Strain, Michael (2007) *Integrated chirped Bragg gratings for dispersion control*. PhD thesis.

UNIVERSITY
of
GLASGOW

Integrated Chirped Bragg Gratings for Dispersion Control

Michael Strain

November 2007

A thesis submitted for the degree of
Doctor of Philosophy (Ph.D.) to the Faculty of Engineering
Department of Electronics and Electrical Engineering
University of Glasgow

I therefore believe myself to have found, on all essential points, the final solution of the problems. And if I am not mistaken in this belief, then the second thing in which the value of this work consists is that it shows how little is achieved when these problems are solved.

Ludwig Wittgenstein

Abstract

In this work, the need for an integrated optical dispersive device is discussed, with particular reference to pulse compression of semiconductor mode-locked laser (MLL) pulses that exhibit temporal chirp and therefore, worse than transform limited behaviour. It is shown that current techniques in fibre and integrated dispersion control do not overlap the dispersion regime presented, making it necessary to design a new integrated device for this purpose.

A monolithic chirped Bragg grating is presented with dispersion and bandwidth characteristics coinciding with the previously mentioned regimes. The device, based on a deeply etched tapered waveguide design, may be fabricated fully post-growth, lending it a significant advantage over current grating designs that require the pattern to be written into the core material and the upper cladding layers subsequently overgrown. The deeply etched sidewall grating structures provide the requisite high coupling coefficients, and the ability to induce arbitrary apodisation profiles, while the tapered waveguide design allows the same freedom with the grating Bragg condition profile.

The coupled-mode analysis for a chirped grating structure is presented and used as a basis for a Transfer Matrix Method (TMM) representation of the device. This simulation tool allows modelling of the arbitrary Bragg condition and apodisation profiles for steady state analysis of passive grating devices, Distributed Feedback (DFB) and Distributed Bragg Reflector (DBR) lasers.

The fabrication of low loss passive grating devices and DFB lasers is described with particular attention paid to lithography and reactive ion etching methods. In addition, work is presented on a wet chemical oxidation technique for reduction of sidewall roughness in AlGaAs based waveguides. Deeply etched waveguides were shown to exhibit losses reduced by up to $4\,dBcm^{-1}$ after application of this procedure. The fabricated passive grating devices exhibit transmission and grating phase profiles closely matching those predicted by the simulations, with control shown over both Bragg condition and coupling coefficient. The DFB lasers, again in agreement with simulation, show unique multi-mode behaviour, closely related to the chirped grating modulation profile.

Also presented is a method by which sub-100 μm tapers for transitions between shallow etched and deep etched waveguides may be fabricated for quasi-adiabatic propagation. These tapers provide a means by which integration may be achieved between optical systems with different mode profiles, these being defined by device properties, for example integration of small radius bends and waveguide gain structures. A simulation tool based on the TMM is derived and a set of optimised tapers are fabricated, their results matched to the simulations. Low loss, low reflectivity tapers are exhibited with properties in close agreement with the TMM and Finite Difference Time Domain (FDTD) simulations.

Publications

Journal Papers

M. J. Strain, M. Sorel, "*Compact Semiconductor Tapers for Deep-to-Shallow Etch Transitions*," IEEE Photonics Technology Letters, vol. 19, no. 19, pp. 1544–1546, 1 Oct. 2007.

M. J. Strain, M. Sorel, "*Post-Growth Fabrication and Characterization of Integrated Chirped Bragg Gratings on GaAs−AlGaAs*," IEEE Photonics Technology Letters, vol. 18, no. 24, pp. 2566–2568, 15 Dec. 2006.

M. J. Strain, M. Sorel, "*Integrated III-V Bragg Gratings for Arbitrary Control over Chirp and Coupling Coefficient*," submitted to IEEE Photonics Technology Letters.

Conferences

M. J. Strain, M. Sorel, "*Integrated Chirped Bragg Gratings on Deeply Etched Tapered III-V Waveguides*," Conference on Lasers and Electro-Optics and the Quantum Electronics and Laser Science Conference (CLEO-QELS), 6–11 May 2007, Baltimore , U.S.A.

M. J. Strain, M. Sorel, "*Fully Post-Growth Fabrication of an Integrated Chirped Bragg Grating for Pulse Shaping (Invited)*," European Semiconductor Laser Workshop (ESWL), 21–22 September 2006, Nice , France.

M. J. Strain, M. Sorel, "*Integrated Chirped Bragg Grating Devices for Pulse Compression (poster)*," ePIXnet Winter School, 13–17 March 2006, Pontresina , Switzerland.

M. J. Strain, M. Sorel, "*Integrated Chirped Bragg Gratings for Dispersion Control*," Postgraduate Research Conference in Electronics, Photonics, Communications and Computing Science (PREP), University of Lancaster, UK, 2005.

Other Publications

D.A. Yanson, S.D. McDougall, I. Baker and J.H. Marsh, A. Sizmann, R. Holzwarth. M. Jost, I. McKenzie, M. J. Strain "*Free-Space Spectrally-Sliced WDM Using Individually Addressable Semiconductor Modulator Arrays*," Submitted to Optical Fiber Communication Conference and Exposition (OFC) ,24–28 February 2008, San Diego, U.S.A.

Acknowledgements

I would like to thank my supervisor, Dr. Marc Sorel, for his guidance and support over the course of this work. His boundless enthusiasm for research has been both infectious and inspiring, and without his efforts this PhD would not have been possible.

I also owe a great amount to Dr. Dan Yanson, my industrial supervisor at Intense. Dan has ever been available and willing to discuss my work and offer useful insight. In addition he has allowed me the opportunity to pursue other avenues of research outwith the confines of the project proper, but greatly useful to my aspirations as a scientist.

The optoelectronics group at Glasgow University is as open and encouraging an environment as one could wish for. Not only have many people taken time to discuss matters both theoretical and practical with me but everyone has been extremely generous with their expertise. In particular I would like to thank Francesca Pozzi who initiated me into the mysteries of semiconductor device fabrication and Marco Gnan who for the last three years has always been eager to talk about the minutae of optical physics. Jenny McGeough has been a good friend, and has made being trapped in the office and the underground labs far easier to bear, especially in light of the often too frequent coffee and cookies. For their help, friendship and the discovery of palinka I would also like to mention Sandor Furst and Gabor Mezosi. And to all of those who have made working in the department a real pleasure, Dave Hutchings, Barry Holmes, Steven McMaster, Harold Chong, Antonio Samerelli, Corrie Farmer and Cross HK Tan.

The results contained in this thesis would not have emerged if not for the smooth and efficient running of the James Watt Nanofabrication centre, and the efforts of the technical staff. Also, Stephen Thoms' knowledge has been invaluable in the issues associated with the E-beam fabrication of grating devices. I would also like to thank Zhong Ren of Bristol University for his work associated with the hydrogen passivation of shallow dopants.

I would like to acknowledge the financial support of EPSRC and Intense who funded the work presented here.

Finally, without the support and constant encouragement of my family and friends I am sure that my course would have been an arduous one. And to Jill I owe deep gratitude for everything.

Contents

List of Figures

List of Tables

Chapter 1

Introduction

1.1 Motivation

Optical pulses are used in applications from telecommunications to biomedical systems, and often the spectral content of the pulse with time is of importance. The advent of Mode-Locked Lasers (MLL) has lead to a reduction of optical pulse widths, allowing increased data rates in optical communication systems, and high peak intensities with broad application areas. However, the optical pulses generated by such lasers are far from perfect. In long haul transmission systems it is desirable to produce pulses with small temporal envelopes - which implies relatively large bandwidths - and transform limited behaviour; that is, the time-bandwidth product of the pulse is at its theoretical minimum. The most prevalent form of deviation from transform limited behaviour is frequency chirp across the pulse width. Chirp - the variation of the pulse's instantaneous frequency in time - tends to spread the pulse temporally and therefore exacerbates the problems of dispersion in long transmission links and depending on the form of the variation, may produce unwanted effects in measurement systems.

The frequency chirping of optical pulses is not limited to linear chirp - a monotonic increase, or decrease, of the spectral content of the pulse over its duration - it is also possible to have higher order pulse chirping where the distribution of spectral components exhibits a variation following the order of the function. In fact, given that integrated optical devices are being produced with ever greater complexity of both type and combinatorial degree the instantaneous frequency of the optical signal may be subject to multifarious influence, resulting in highly complex chirp functions. This work will be concerned with producing a device that may be easily incorporated into current integrated optical morphologies with simple post growth fabrication techniques. Monolithic chirped Bragg gratings will be designed with flexibility not only to compensate for the chirp of mode-locked lasers but that may also induce an arbitrary chirp into the pulse. In addition to modulation of the Bragg condition of the grating it is possible to control the grating coupling coefficient. By variation of the coupling coefficient, or apodisation of the grating, its reflectivity with respect to wavelength may be controlled. Grating apodisation allows the opportunity for reducing ripple in both grating reflectivity and group delay characteristics in addition to creation of devices that may have arbitrary reflectivity profiles. With influence exerted over both grating chirp and apodisation, devices may be designed with great flexibility and for many applications.

1.2 Mode-locked laser diodes

In the pursuit of shorter pulses and faster repetition rates for telecommunications systems mode locked diode lasers are a significant step forward. With repetition rates into the Terahertz regime and pulses under picosecond durations, diode MLLs provide an attractive solution for a wide range of applications. A very thorough review of the topic is presented by Avrutin et al [1].

1.2.1 Operation

The basic operation of mode-locked lasers harnesses the range of longitudinal modes that are present in a laser cavity. In the case of a Fabry-Pérot (FP) laser the longitudinal modes of the cavity are defined by the optical path length between the laser facets, the modal propagation constant and the facet reflectivity, such that a number of discrete modes are allowed within the cavity. Added to this is the material gain bandwidth which defines the gain of the medium with respect to wavelength and together these two parameters give a spectrum for the lasing wavelengths of the cavity.

In a mode locked laser the goal is to arrange the propagation of the allowed modes such that their phases are locked, thus creating a pulse that travels around the

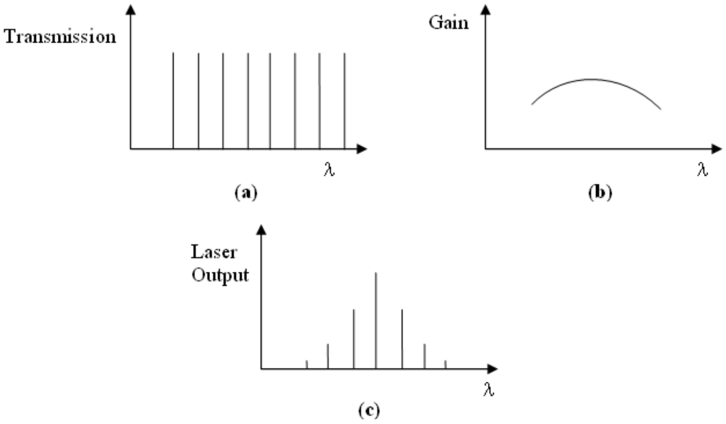

Figure 1.1: Spectra of (a) Transmission of a Fabry-Pérot cavity (b) Material gain (c) Power output of a FP laser.

cavity which is the superposition of the locked modes. Clearly, by increasing the number of modes involved in the creation of this travelling pulse, the shorter its temporal envelope will be - assuming transform limited characteristics - due to its larger bandwidth.

In order to create the locking of the modal phases a number of methods are commonly employed. The first of these is the passive mode locking scheme [1–3]. The device is modified to include a saturable absorber at one facet as shown in Figure 1.2. The lasing modes are attenuated in the absorber section unless, when

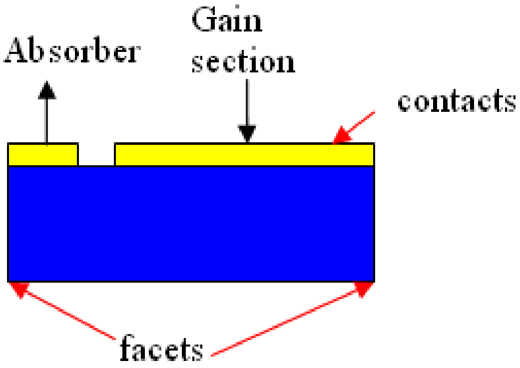

Figure 1.2: Schematic of a passively mode-locked laser diode.

a mode-locked superposition is present, the power is high enough to saturate the absorber and allow the pulse to continue circulating in the cavity. The absorber section may also be located in the centre of the cavity to create a colliding pulse MLL [3, 4] where the repetition rate of the laser is double that of a device where the repetition rate is the cavity round trip time.

MLLs may also be hybridly or actively mode-locked [1, 3]. In active mode-locking the absorber section is driven with a microwave frequency close to the repetition rate, or its harmonics, that assists in the creation of the mode-locked laser pulse.

1.2.2 Chirp in mode-locked laser diodes

A limiting problem with MLL diodes is that they exhibit unwanted frequency chirp in their output pulses [4–10]. Frequency chirp is the phenomenon of the instantaneous pulse frequency varying with time.

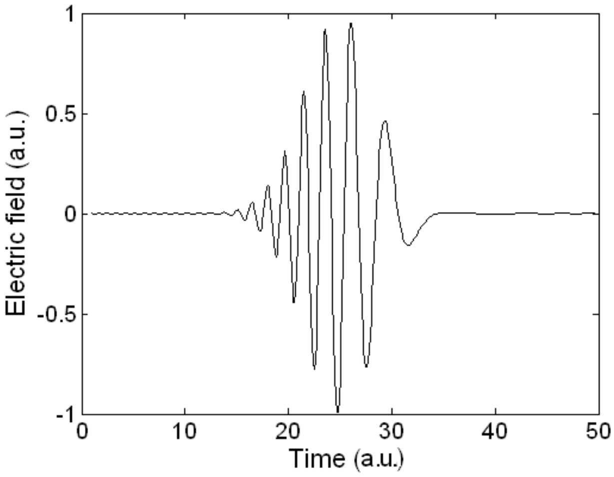

Figure 1.3: Red chirped optical pulse with time.

In the relatively long gain section of MLLs the mode-locked pulse undergoes self-phase modulation (SPM) due to the effect of its high intensity on the refractive index of the medium. This SPM is related to the instantaneous frequency of the pulse through the modified refractive index [3].

$$\omega(t) = \frac{2\pi c}{\lambda_0} \frac{1}{n_0 + \delta n} \tag{1.1}$$

Where $\omega(t)$ is the instantaneous frequency, c is the speed of light in a vacuum, λ_0 is the free space wavelength, n_0 is the material refractive index and δn is the intensity dependent component of the refractive index. The characteristics of a chirp free pulse and a pulse after SPM are illustrated in Figure 1.4. After the SPM the pulse experiences a red chirp towards its peak, then a blue chirp in its tail. However, in the absorber, due to saturation it is the tail of the pulse that is emphasised, effectively shifting the envelope back in time and so creating an overall blue chirp of the pulse. The SPM of the pulse in the absorber is negligible due to its short length, usually in the order of tens of micrometres [7].

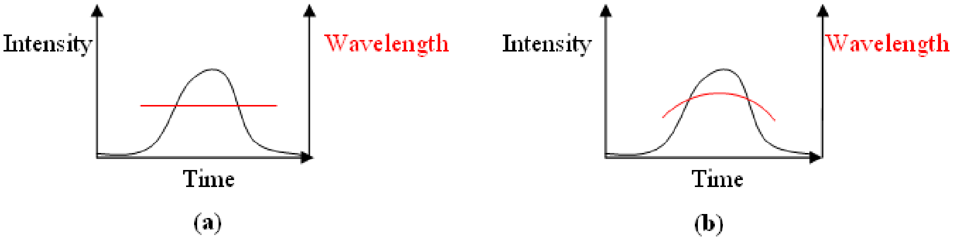

Figure 1.4: Effects of SPM on unchirped pulses (a) unchirped pulse (b) after SPM.

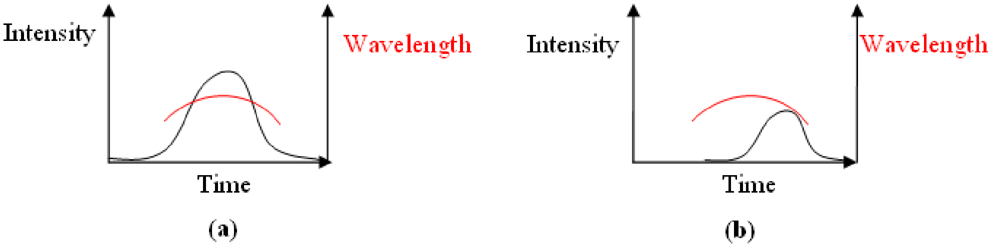

Figure 1.5: Blue chirp of pulses due to saturable absorber (a) before absorber (b) after absorber section.

Hybrid and actively mode-locked lasers behave slightly differently due to the driving signal on the absorber section. The driver shifts the pulse in time, the direction determined by the shift of the signal above or below the passive repetition rate, and so results in an overall red or blue chirp depending on whether the pulse is shifted forward or backward in time [4, 7].

1.3 Pulse dispersion compensation

There are a number of groups who have investigated pulse compression techniques to compensate for the undesirable pulse chirping described in section 1.2 [11–22]. The common component in these pulse compression schemes is the use of grating technology.

In systems where the physical size of the setup is not important free space gratings have been applied [3, 23–25]. In the free space configuration one or two reflective gratings are arranged such that the group delay of the pulse on reflection is frequency dependent. By tailoring the geometry of the gratings the pulse may be compressed or extended in time; the combination of such functions are commonly used for the amplification of high power ultra-short pulses [3] where the pulse is extended to reduce its peak power before amplification and subsequent re-compression. However, these systems are bulky and require careful alignment, making them suitable for high power lab situations rather than in-situ telecommunications or measurement applications. It is therefore desirable to have systems that are easily incorporated into the common fibre and integrated optical technologies. Bragg grating devices based on the periodic modulation of waveguiding materials' effective index are an attractive solution in this area and can be broadly divided into two categories: fibre or integrated devices.

Bragg gratings are periodic perturbations in the refractive index of the guiding medium. When the period of the grating is constant it produces a narrowband reflective component in the waveguide. The peak of the reflection spectrum for a 1^{st} order Bragg grating is defined by the period of the perturbation such that:

$$\lambda_B = 2n_{eff}\Lambda_0 \tag{1.2}$$

Where λ_B is the free space wavelength of the mode satisfying the Bragg condition, n_{eff} is the effective index of the waveguide and Λ_0 is the period of the index perturbation.

If the period of this device is chirped, i.e. its period varies along the propagation direction, the device becomes broadband in response with a varying Bragg reflection wavelength along the device length. In essence this results in a device which reflects the varying frequency components of the pulse at different points along its length creating a graded group delay profile. Therefore the long wavelength components of the pulse will see a different delay to the short wavelength components, and if the profile of the delay is opposite to the group dispersion in the pulse the wavepacket may be compressed, as shown in Figure 1.6. Therefore, chirped Bragg gratings appear to be an elegant pulse compression solution in waveguiding media.

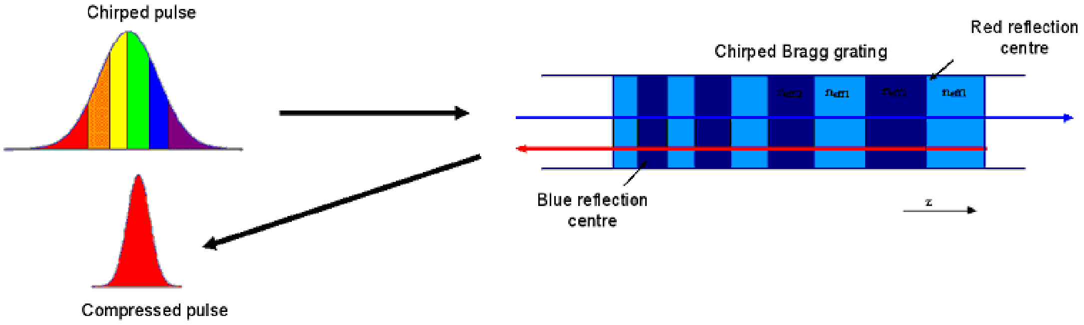

Figure 1.6: Pulse compression using a chirped Bragg grating.

Much work has been done in optical fibres using chirped Bragg gratings [11–16, 18–22, 26] to this end, however, in integrated optics the chirped grating has chiefly been harnessed for applications other than dispersion compensation [27–36] including wavelength tuning of lasers [36] and chirp compensation in spot size converters [33].

1.4 Fibre based devices for pulse dispersion compensation

Most of the work carried out in pulse compression techniques using chirped Bragg gratings has been concentrated on fibre devices. There are a number of reasons for concentrating on fibre schemes. Firstly if pulse compression is required in long haul transmission systems, it seems attractive to implement an all fibre compression system; this circumvents the need for electronics and coupling in and out of the fibre to integrated devices. Secondly, writing Bragg gratings in photosensitive optical fibre is a well established technique, and since the refractive index perturbation occurs over the entire guiding area the coupling factor associated with the grating is high, leading to high reflectivity and good control over the designed grating parameters.

1.4.1 Fabrication methods

There are a number of techniques used to write chirped gratings in photosensitive fibres. One method is based on two beam holographic sidewriting technology already established for writing fixed period Bragg gratings [12, 14]. In the two beam holographic method two UV beams are focused on the core of the fibre such that an interference pattern is created, the high intensity portions of this distribution creating a refractive index change in the core. A fixed period grating is written by directing both beams at an equal angle either side of the normal to the fibre surface. A chirped grating may be introduced by angling the beams such that the period of the interference pattern varies with distance along the propagation direction of the fibre, as shown in Figure 1.7. The chirp may also be introduced by curving the fibre through the interference pattern [21] or using a fibre with a tapered core [12] and so varying the modal index across the constant spatial period grating written with the holographic technique.

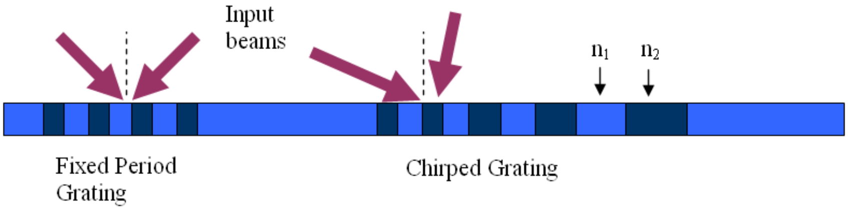

Figure 1.7: Writing fixed and variable period gratings using a two beam holographic method.

Phase mask technology, where a diffractive element is placed between a laser source and the fibre to create an interference pattern from the source on the fibre core, is similar to the holographic method in many ways and chirp may be induced in the interference pattern by the same methods as previously noted [11, 16]. A phase mask method of step chirping may also be utilised, where a phase mask is employed to produce grating sections, of dimensions much less than the total grating length, with varying period [11]. The final grating structure is a discretised approximation to a continuously chirped grating. The holographic writing technique may be further extended for use without a pre-fabricated phase mask, the grating amplitude and phase being controlled directly by computer allowing for flexible grating design [37].

Another method used for writing gratings in optical fibres is the double exposure photo-imprinting technique [15]. In the double exposure method the first exposure is directed through a mask scanned along the fibre length, this creates a linearly varying refractive index along the length of the fibre. The second exposure creates the periodic index change in the normal fashion using a phase mask, the total effect being an effectively chirped Bragg grating with constant spatial period.

1.4.2 System configuration

In general the setup for a fibre pulse compressor is as shown in Figure 1.8 [22]. In the fibre compression system shown in Figure 1.8, the dispersed pulse is coupled into a Chirped Fibre Bragg Grating (CFBG) acting in reflection mode. High reflectivities have been demonstrated in these devices, up to around 95% [11, 16]. The reflected pulse is compressed as described previously and coupled back into the transmission system by means of a 50:50 power splitter. Obviously, one of the major disadvantages of this method is the $3\,dB$ power loss on input and output coupling to the CFBG line, due to the coupler. However, pulse compressions of up to 40 times have been demonstrated [11, 16], therefore as any loss of signal power may be compensated for after the filter section, these devices show good potential for in-fibre links.

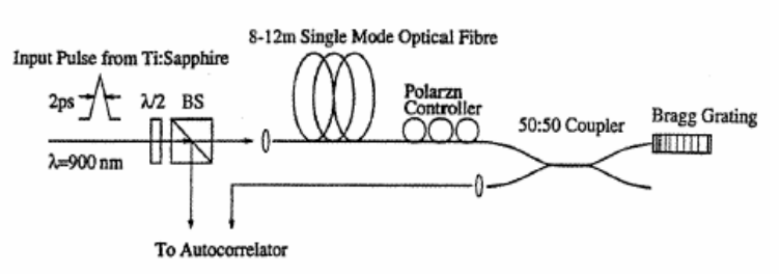

Figure 1.8: Fibre based pulse compression system[22].

1.5 Integrated devices for dispersion compensation

Although in-fibre devices appear to be relevant solutions to long haul degradation of optical signals, they are physically large. It is clearly desirable to compensate for pulse chirp at the source, before the generated chirp is exacerbated in transmission through dispersive media, and it would be preferable to refrain from the use of large fibre based components if possible. A further advantage of an on-chip dispersive element is that known dispersion of a fibre link may be pre-compensated; such that dispersion of equal magnitude and opposite sign is applied to the pulse before it is transmitted, therefore, the pulse at the receiver should be chirp free.

1.5.1 Arrayed waveguide gratings, chirped mirror stacks and quasi-phase matched devices

Chirp compensation has been attempted in integrated devices by means of arrayed waveguide gratings (AWG), chirped thin film mirrors and quasi-phase matching devices [35]. Arrayed waveguide grating devices operate by splitting the input pulse into discrete spectral ranges and propagating each portion through waveguides of varying optical length as shown in Figure 1.9. As each discrete section of bandwidth sees a unique optical path length there is a wavelength dependent delay introduced into the system, so that dispersion of the pulse is apparent on recombination in the output coupler. One advantage of this system is that it operates in transmission, potentially avoiding losses associated with reflective devices. However, the operation of the AWG structure is limited both by the bandwidth of the wavelength dependent input and output couplers and the number of waveguides that may be fabricated to carry the sectioned bandwidth of the pulses. The

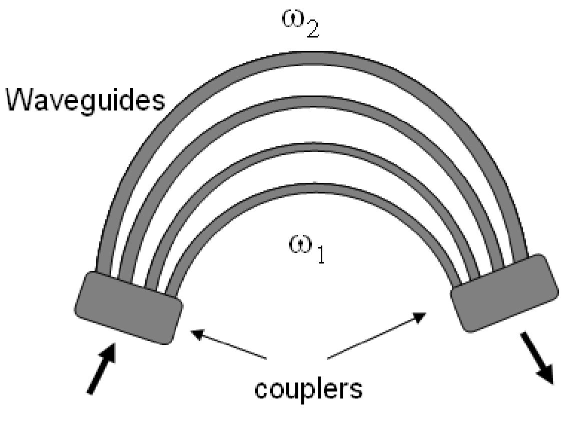

Figure 1.9: Arrayed waveguide grating for pulse compression.

physical size of AWG devices is also prohibitive, being typically in the order of centimetres, in semiconductor integrated optics where losses are higher than in glass and often device footprint is a concern.

Chirped mirror (CMs) stacks, Figure 1.10, operate in a similar manner to Bragg gratings, although the coupling coefficient associated with CMs is far greater than the weakly reflecting Bragg gratings. The main advantage of the high reflectivity of the stack layers is that very few periods are necessary to couple significant power into the backward propagating mode. The CM stack is through virtue of its high reflectivity a physically small device, which in turn limits the amount of dispersion that may be induced in the input signal. A further limitation of this device geometry is that it is necessary to couple into the mirror stack from free space, a requirement that inflates the device footprint when including the area needed for coupling optics and joints.

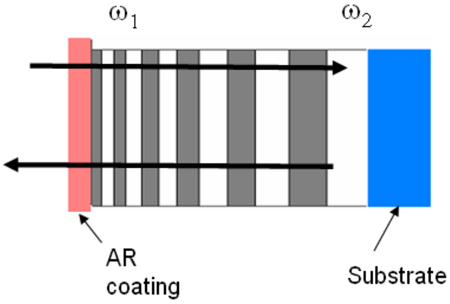

Figure 1.10: Chirped Mirror stack.

Like AWG devices Quasi-phase matched (QPM) gratings operate in transmission. In a single period QPM device the input signal is used to generate a second harmonic output. By varying the pitch of the QPM sections the dispersion of the output second harmonic pulse may be controlled. A schematic of a QPM grating is shown in Figure 1.11.

1.5.2 Chirped Bragg gratings

The fabrication techniques associated with integrated devices allows for great variability in the construction of grating structures, which are easily incorporated into monolithic waveguides and hence readily compatible with other integrated

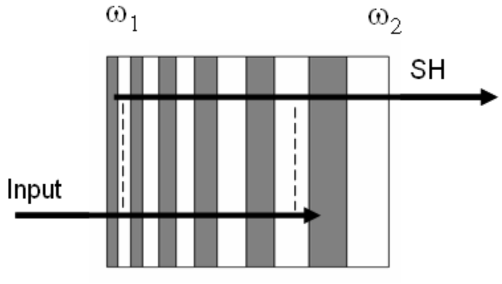

Figure 1.11: Quasi-phase matched device.

optic devices. The fabrication flexibility may be utilised to create gratings of non-linear period variations, allowing for tailorable dispersion characteristics. With these advantages, devices based on integrated optics are an elegant solution for dispersion control of optical signals. However, the task of fabricating chirped gratings in integrated optical components is more challenging than in the case of fibres. There has been some limited work carried out in the fabrication of Chirped Bragg Gratings (CBGs) in integrated devices [23,24,27–36,38–41], but most have concentrated on the tunability this affords to Distributed Feedback (DFB) lasers, rather than the potential for chirp compensation [27,28,32,34,36,41].

The introduction of a chirped Bragg grating in the DFB laser allows the output wavelength to be tuned, by exploiting the varying pitch of the grating to localise the photons in particular regions [28], and hence select the lasing wavelength. Mohrle et al. present a DFB laser based on a tapered waveguide [33]. The taper of the waveguide is introduced to promote more efficient mode matching between the laser and fibre modes in an attempt to reduce coupling losses. However, by tapering the ridge waveguide that the DFB is based around the effective index of the lasing mode will vary along the device length. Referring back to (1.2) it is clear that by modifying the effective index of the mode the Bragg wavelength of the device is also altered. To compensate for the undesirable change in Bragg wavelength the authors implemented a chirped grating that varied in period corresponding to the unwanted shift in Bragg wavelength due to the changing effective index.

Work has also been carried out into the tuning of Distributed Bragg Reflector (DBR) lasers [36]. In the DBR devices one reflector was fabricated as a phased Bragg grating and the second as a sampled grating reflector that exhibited a broadband reflection characteristic. The phased grating is a single period grating with π phase shifts in the grating periodicity along its length. The phase shifts result in a grating response that may be designed to exhibit a top-hat comb of reflection peaks with equal amplitude and spacing. The sampled grating is overlaid with a series of electrical contacts along its length which, when biased in various configurations, can tune the reflection peak of the grating to correspond to one of the phased grating modes. In this way the device produces a discretely tunable laser over a broad spectrum.

An example of pulse compression using a CBG on InP based integrated MLLs is presented by Sato et al. [38–40]. A MLL with one chirped DBR mirror was fabricated, and generation of near transform limited pulses at around $4\,ps$ in length.

Current device geometries

The chirped gratings in the above mentioned devices were fabricated in a number of ways. The first method was based on writing a fixed longitudinal period grating on a bent waveguide using direct Electron Beam (E-beam) lithography [29–31]. The waveguide path induces a changing grating period along its length in exactly the same manner as the curved fibre device outlined previously. The second method was based on a spherical holographic technique [28]. In this case the grating was a series of fixed period grating sections, in entirety approximating a linearly chirped grating. A novel E-beam lithography technique has also been demonstrated which consists of multiple exposures at varying beam incidence angles to create a chirped grating pitch, as shown in Figure 1.12 [33, 34]. The writing time for the multiple exposure method is much higher than that for writing a simple grating, and in addition a significant amount of modification to the

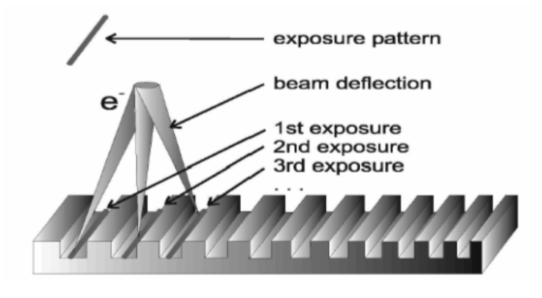

Figure 1.12: Double exposure E-beam method for chirped grating fabrication[34].

standard addressing scheme of the E-beam writer is required to allow application of the novel multiple exposure pattern.

Finally, Sato et al use a multiphase shifted pattern to approximate a linearly chirped grating [40]. A fixed period grating is written using E-beam lithography in the normal manner. To introduce the chirp a phase shift is introduced into the grating structure with the relationship $\sqrt{i}m\Lambda_0$, where i is the index of the phase shift position $(1, 2, 3..)$, m is the number of periods from the start of the grating to the first phase shift, and Λ_0 is the grating period as usual. The equivalent chirp rate of the multiphase shifted grating may be expressed as:

$$r_c = \frac{4n_{eq}\frac{\Delta\Lambda}{\Lambda_0}}{m^2} \tag{1.3}$$

Where r_c is the chirp rate, n_{eq} is the equivalent refractive index of the waveguide and $\Delta\Lambda$ is the constant phase shift being introduced. A representation of the phase shifted grating is shown in Figure 1.13.

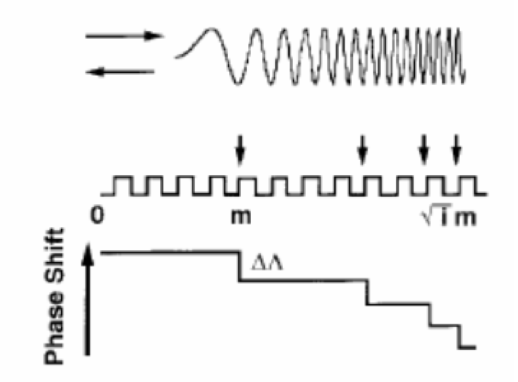

Figure 1.13: Multiple phase shifted grating[40].

Fabrication of integrated gratings

The common root of the chirped grating devices covered in the literature is the pattern and overgrowth procedure used to fabricate them. The main issue necessitating this fabrication technique is the requirement of a high coupling coefficient in the grating structure. For single period gratings of a few hundred microns in length a coupling coefficient under $5\,cm^{-1}$ is sufficient to provide a high narrowband reflectivity of over $60\,\%$. However, since in the chirped grating the Bragg wavelength is shifted along its length, the peak reflectivity will be reduced with the increasing bandwidth. As a result a much higher coupling coefficient is required to produce a significant reflectivity. For a passive grating the coupling coefficient, (1.4), is related to the proportion of the mode that experiences the refractive index perturbation and the magnitude of that disturbance. This relationship is discussed in more detail in section 2.2.

$$\kappa = \frac{k_0^2}{2\beta} \frac{\iint \Delta\epsilon(x,y) U(x,y)^2 \, dxdy}{\iint U^2(x,y) \, dxdy} \tag{1.4}$$

In (1.4), κ is the coupling coefficient, k_0 is the free space propagation constant, β is the modal propagation constant, $\Delta\epsilon(x,y)$ is the deviation of the material permittivity along the z axis due to the perturbation and $U(x,y)$ is the spatial envelope of the mode. In shallow etched gratings fabricated using post growth processes κ is limited by the small proportion of the mode that experiences the index modulation. By employing a fabrication technique where the grating is directly written into the waveguide core and the upper-cladding grown over the structure, the coupling coefficient may be greatly enhanced by the much larger proportion of the mode travelling within the area of the index modulation. The lithographic techniques used to pattern the core gratings are outlined in section 3.2. The processes used for etching the waveguide ridges after upper-cladding growth are common to both the overgrowth method and the post-growth technique that will be presented in this work.

1.6 Comparison of integrated device geometries

As outlined in section 1.5 there are a number of technologies available to deal with dispersion in optical signals. However it was also noted that each of these techniques operate over finite bandwidth and dispersion regions. In addition to the limits of operation there are also physical limits that define the size of the device. For the technologies discussed previously the optical and physical ranges of operation are given in Table 1.1, where GDD is the group delay dispersion. The information presented in Table 1.1 can be further illustrated in a plot showing the operation regimes of each device structure as in Figure 1.14. These results may be considered with relation to both the absolute values of bandwidth and dispersion relating to each device and the range of each over which they operate. Chirped

Table 1.1: Characteristics of dispersive device structures.

Device	Optical length (m)	Bandwidth (nm)	GDD (ps^2)
Chirped Mirror	10^{-5}	$200 - 350$	5×10^{-5}
FCBG	$10^{-2} - 1$	$0.1 - 10$	$5 \times 10^{2} - 10^{4}$
AWG	10^{-2}	0.5	$100 - 300$
QPM	$0.05 - 5 \times 10^{-4}$	$10 - 500$	$5 \times 10^{-4} - 0.3$

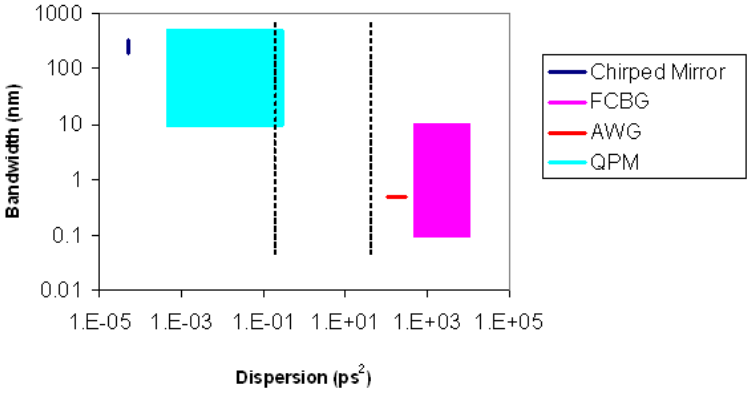

Figure 1.14: Dispersion and bandwidth characteristics of available dispersive devices.

mirrors present very limited dispersion due to the small physical length of the device, however they have large possible bandwidths in the range of hundreds of nanometres. AWGs alternatively, have very small bandwidths, limited mainly by the operation of the wavelength dependent couplers at the input and output of the arrayed waveguides. AWGs do produce significant dispersion profiles in the order of hundreds of ps^2, as they are physically large devices, though it is useful to recall that their operation is essentially discrete with respect to spectral and temporal response. Quasi-phase matched devices exhibit small absolute dispersion, but with a range of operation that promises some ability to design the device for specific applications. They also operate over a reasonably large range of bandwidths, again promising some flexibility in design of devices. It is worth recalling from section 1.5 that the QPM devices are operating on dispersion control of the second harmonic generated in the structure rather than the input signal. Chirped fibre Bragg gratings are similar, with respect to range of operation, to the QPM devices. CFBGs can be designed over a large range of large absolute dispersion - due to the potentially long device length of the CFBGs - and a reasonable range of bandwidth. Like the QPM devices this allows design of dispersive devices with flexible range of operation and induced dispersion.

Previously a review of the above listed techniques was carried out and on the basis of physical application at least, it was suggested that integrated CBGs were an attractive alternative device geometry. There is now another clear argument for the pursuit of integrated CBGs based on the device dispersion and bandwidth parameters. From Figure 1.14 a gap in the dispersion coverage of the available technologies is apparent between 10^{-1} and $2 \times 10^{1} ps^2$. Recalling that one of the main application areas for dispersion control - and one in which the physical characteristics of integrated CBGs make them particularly suitable - is that of dispersion control in MLLs. It is useful to consider the range of dispersion characterised in these devices. Typically MLLs exhibit dispersion in their output pulses in the range of $1.2 \times 10^{-1} - 12 \times 10^{1} ps^2$ [7], coinciding with the range of dispersion so far not covered by other technologies.

As in the case of other dispersive devices the dispersion achievable using integrated CBG structures is related to the bandwidth of operation and the physical dimensions of the devices. As mentioned earlier the length of the grating is closely related to the required reflectivity of the response, the bandwidth over which the device reflects and the coupling coefficient. Therefore the size, dispersion and bandwidth of the CBG are interrelated parameters that given a set of design constraints - to be discussed further shortly - are defined by the device structure itself. However from these considerations the dispersion characteristics of integrated CBGs may be shown not only to fill in the dispersion gap left by other technologies, but also to overlap conveniently with the chirp characteristics of the integrated MLLs discussed previously. Figure 1.14 may be modified to show the inclusion of the integrated CBGs, as in Figure 1.15. It was noted that to achieve a favourable balance of these parameters the majority of current work in the field has been concentrated on writing longitudinally chirped, or discrete approximations to linearly chirped gratings, directly into the core region of waveguiding devices and subsequently overgrowing the upper cladding layers. While producing desirable dispersion characteristics these methods are unwieldy and require sensitive fabrication steps. Therefore it is desirable to pursue the design of an integrated CBG structure that while retaining the attractive dispersion characteristics of the available techniques is easily fabricated. In particular it would be beneficial not only to manufacture the device fully post-growth of the wafer but also to create continuous chirp in the structure without resorting to complicated direct schemes as mentioned in section 1.5.

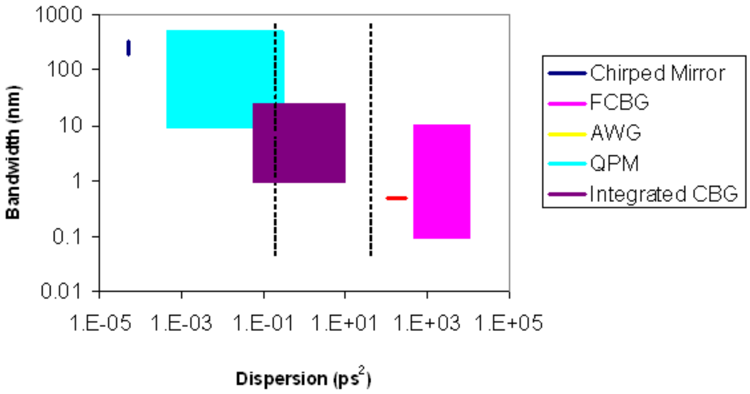

Figure 1.15: Dispersion and bandwidth characteristics of available dispersive devices including integrated CBGs.

Chapter 2

Chirped Bragg Gratings, Theory and Design

Integrated chirped Bragg gratings may be used to compensate for frequency chirp in optical signals, or more generally to modulate the dispersion of the signal in some arbitrary manner. In order to design a CBG for use in such applications a thorough understanding of the underlying theory must first be obtained. Therefore, the operation of Bragg gratings is discussed here, and how this may be extended to include the effects of introducing chirp and apodisation to the grating. Once this has been established it is possible to consider simulation methods relevant for the design of the devices described in this work.

2.1 Simple Bragg grating theory

As described in Agrawal's book [42] it is possible to induce coupling between orthogonal modes of a waveguide by introducing a refractive index perturbation. By making this perturbation periodic in the propagating direction it is possible to couple between forward and backward propagating modes of the waveguide. In simplified terms, a periodic perturbation of half the propagating modal wavelength will induce 1^{st} order coupling between forward and backward modes with equal magnitudes of propagation constant, and opposite sign. This is given by the Bragg condition:

$$m\lambda_B = 2n_{eff}\Lambda_0. \tag{2.1}$$

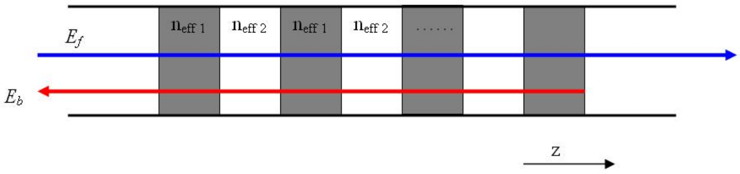

Figure 2.1: Schematic of a Bragg grating showing ray paths of forward and backward propagating modes

Where m is the order of the grating response $(m \in \mathbb{Z}, m > 0)$, λ_B is the free space wavelength of the mode satisfying the Bragg condition, n_{eff} is the effective index of relevant waveguide modes and Λ_0 is the period of the index perturbation. The frequency response of a single period grating may be considered as a narrowband filter around the Bragg wavelength, and is widely used in many applications. Figure 2.1 shows a representation of the basic operation of this device. In Figure 2.1, E_f is the forward propagating mode in the Bragg grating where as it travels through the grating region the wavelength component that satisfies the Bragg condition is coupled into the backward propagating mode, E_b. The device response is fairly easily modelled using the Bragg condition for a simple periodic grating. However, it is not so straightforward to design a grating with a chirped period. To allow the design of the latter device, it is desirable to consider a more general solution to the simple periodic grating case which may then be expanded to allow for the introduction of a chirp to the period. The method by which this may be accomplished is the consideration of coupled-mode theory to describe the interaction of the propagating modes and the index perturbation of the waveguide.

2.2 Coupled-mode analysis of a fixed period Bragg grating

The full derivation of the coupled-mode solutions for a waveguide with periodic index perturbation is presented in Appendix A. The most significant outcome of this analysis is that the system may be described using expressions for the forward and backward propagating modes, interelated by the coupling coefficient, κ, index petrurbation period, Λ_0, and the boundary conditions of the grating structure. So in summary, the 1^{st} order solution for a single period Bragg grating may be obtained with the following system of equations.

$$E(z) = A(z)\exp[-j\beta_0] + B(z)\exp[j\beta_0] \tag{2.2}$$

$$A(z) = A_1 e^{-jqz} + r(q) B_2 e^{jqz} \tag{2.3}$$

$$B(z) = B_2 e^{jqz} + r(q) A_1 e^{-jqz} \tag{2.4}$$

$$r(q) = \frac{(jg + \Delta\beta) - q}{\kappa} \tag{2.5}$$

$$q^2 = (jg + \Delta\beta)^2 - \kappa^2 \tag{2.6}$$

$$\kappa = \frac{(n_2^2 - n_1^2)\Gamma_{x,y}}{2n_{eff}^2 \Lambda_0} \tag{2.7}$$

Where $E(z)$ is the total z-dependent electric field in the structure, β_0 is the propagation constant of radiation meeting the Bragg condition of the grating, $\Delta\beta$ is the detuned propagation constant from the Bragg condition, A_1 and B_2 are constants related to the grating length, boundary and Bragg conditions, n_{eff}, n_2 and n_1 are the refractive indices of the propagating mode, the waveguide and the lower index portion of the grating respectively, $\Gamma_{x,y}$ is the confinement factor of the mode to the grating area, and g is the modal gain. The grating chirp, as described previously is achieved by modulating β_0 with z, and the apodisation is controlled by means of a z-dependent coupling coefficient, κ. The transmission and reflection spectra of a single period grating, with zero gain, are shown as a function of wavelength in Figure 2.2, with the associated phase responses shown in Figure 2.3, where the grating length was set at $450\,\mu m$ and $\kappa = 50\,cm^{-1}$.

2.3 Modelling of chirped Bragg gratings

The analysis of a CBG follows directly from that described for constant period gratings. As outlined previously, a chirped grating has a Bragg condition that varies along the propagation direction, producing a wavelength dependent phase profile that may be controlled by means of the physical grating parameters. Chirped Bragg gratings may be described by the coupled-mode equations where the system is expanded to include the effects of the $z-$dependent Bragg condition. However, this analysis is rather involved and description of the devices may be more readily achieved through simulation methods. Due to the physical dimensions of the devices, and the fact that the gratings are chirped and apodised, modelling

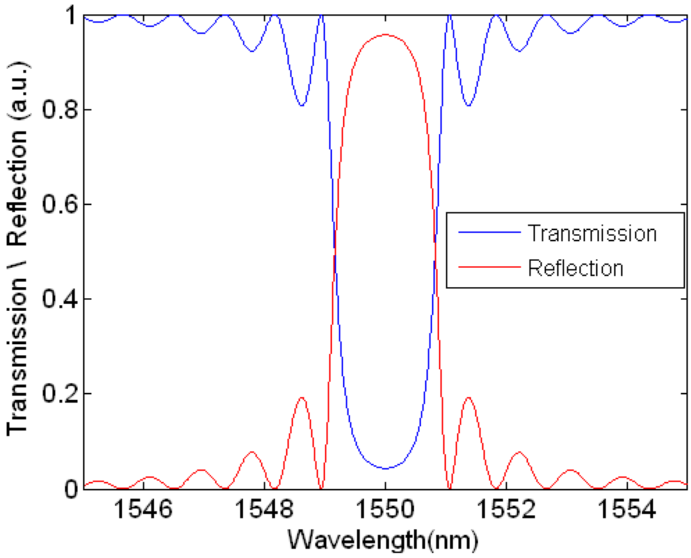

Figure 2.2: Simulated transmission and reflection spectra of a single period grating. $L_g = 450\,\mu m, \kappa = 50\,cm^{-1}$.

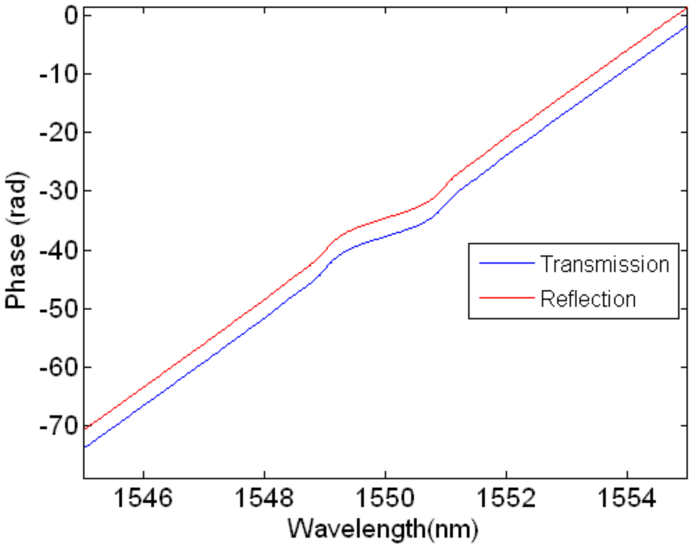

Figure 2.3: Simulated transmission and reflection phase of a single period grating. $L_g = 450\,\mu m, \kappa = 50\,cm^{-1}$.

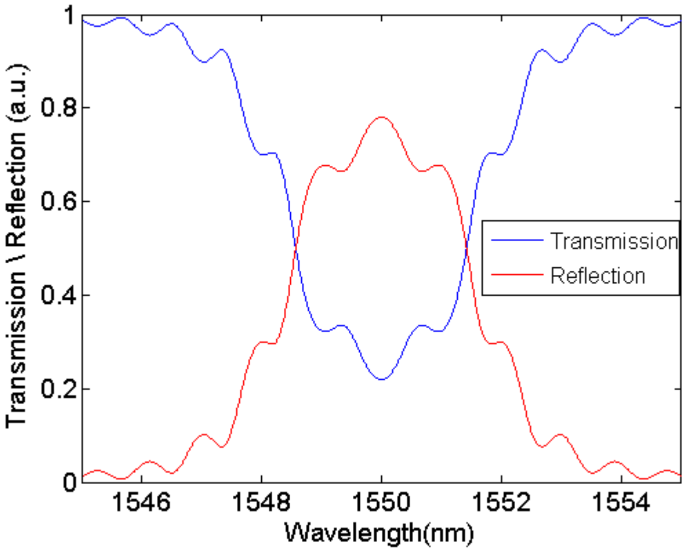

Figure 2.4: Simulated transmitted and reflected field intensities of a linearly chirped Bragg grating. $L_g = 450\,\mu m$, Bandwidth=$4\,nm$, $\kappa = 50\,cm^{-1}$.

using Finite Difference methods is computationally prohibitive. One method that may be harnessed for the purposes of this work is that of Transfer Matrix Method models, to be discussed more fully in section 2.5. Using this technique the grating may be characterised in both transmission and reflection for amplitude and phase.

For example, the response of a linearly chirped grating with $L_g = 450\,\mu m$, $\kappa = 50\,cm^{-1}$ and $\Delta\beta_{max} = 1.622 \times 10^4\,m^{-1}$ corresponding to a bandwidth of $4\,nm$, is plotted in Figure 2.4 and Figure 2.5. As is expected, the width of this function is much larger than that of the fixed period grating, showing a peak reflectivity spanning a larger range of wavelengths due to the grating chirp. However, this increased bandwidth over the same length of grating results in the reduction of peak reflectivity. It is also clear that the phase of the transmitted and reflected waves have diverged from the simple single period grating case. In the simple grating the phase of both forward and backward modes was modulated over the relatively narrow stopband region, and in a similar fashion. However, in the case of the linearly chirped grating it is evident that the z-dependent Bragg condition allows the transmitted wave, whose phase accumulation is associated with the integration of the now z-dependent group velocity of the field to pass with only small phase modulation. However, in reflection this z-dependence strongly affects the phase profile of the field. A more useful method of handling this relationship,

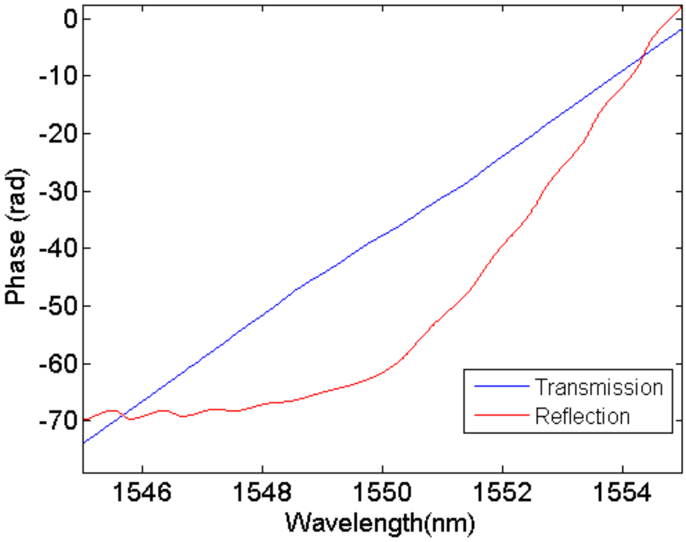

Figure 2.5: Simulated phase response of transmitted and reflected fields of a linearly chirped Bragg grating. $L_g = 450\mu m$, bandwidth=4 nm, $\kappa = 50\, cm^{-1}$.

especially considering the dispersion based applications of these techniques, is to consider the group delay, τ_g, of the reflected field. The group delay is the derivative with respect to rotational frequency of the field, $\left(\frac{\partial \phi}{\partial \omega}\right)$, and illustrates quite effectively the function of the chirped grating. For example, a linearly chirped grating, which produces a quadratic phase profile in reflection, exhibits a linear delay function, as shown in Figure 2.6. For the linearly chirped grating discussed previously the grating may be described in terms of its transmission spectrum and group delay profile. The transmission spectrum is selected as this is more easily measured than the reflection characteristic, and with measurement of the grating loss the reflection spectrum may be inferred. In addition the group delay in reflection may be measured using interferometric techniques, that through careful design of the integrated device geometry may be tested in the same rig as the transmission measurements. Verification of these methods are given in Chapter 4.

2.4 Dispersion control

As discussed in section 2.3 a Bragg grating may be chirped to create a wider reflection bandwidth response. The chirp of the grating also introduces dispersion

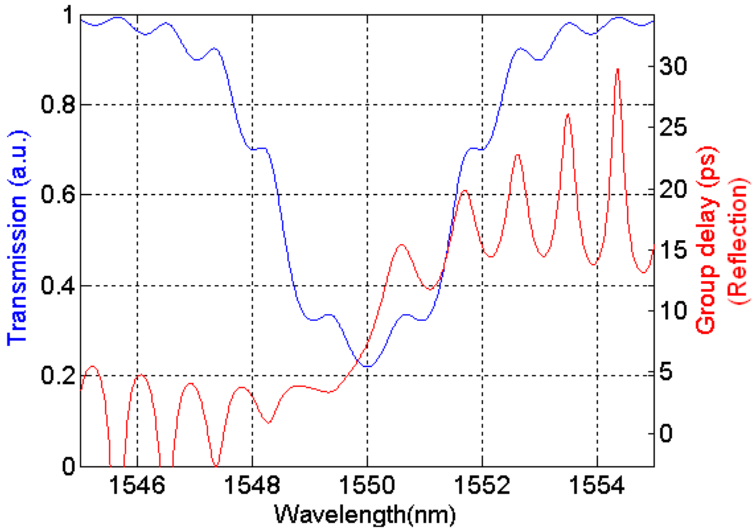

Figure 2.6: Simulated transmission spectrum, and group delay in reflection of a linearly chirped Bragg grating. $L_g = 450\,\mu m$,Bandwidth=$4\,nm$, $\kappa = 50\,cm^{-1}$.

to the pulse as each wavelength component reflected by the device sees a reflection delay relative to its frequency. As outlined in the introduction, devices exhibiting dispersion have wide ranging applications and the design of this dispersion is desirable. In order to engineer the dispersion characteristics of integrated CBGs a relationship must be drawn between the z-dependent Bragg condition and the optical path length seen by the pulse frequency components corresponding to the reflection bandwidth distribution.

As was stated earlier the characteristics of a chirped Bragg grating are most easily illustrated using its transmission spectrum and group delay profile. However, a common measure of chirped grating performance, particularly for linearly chirped gratings, is the grating dispersion. The dispersion of a given device is obtained by further differentiating the group delay with respect to the field rotational frequency, $\frac{\partial \tau_g}{\partial \omega}$. So that a grating with a linearly varying group delay profile gives a constant dispersion. This dispersion may be related to the grating length, L_g, effective bandwidth and group velocity as shown in (2.8).

$$D = \frac{2L_g}{Bv_g} \tag{2.8}$$

Where D is the dispersion, B is the bandwidth of the grating and v_g is the group velocity of the pulse through the grating. For simplicity the group velocity is assumed to be constant across the pulse bandwidth and equal to the group velocity of the mode in the unperturbed waveguide. The bandwidth of the filter may be chosen so that it matches the bandwidth of the input pulses. Therefore for any pulse with known bandwidth and dispersion, the filter length necessary to counteract this dispersion may be found. However, for more complex grating designs the grating dispersion, along with the group delay and transmission spectrum, will be a wavelength dependent function and therefore the group delay will remain the method by which the grating is assesed, being the most intuitively understandable of the phase based relations. As an example of these measures the characteristics of a single period grating, a constant κ linearly chirped grating and an apodised chirped grating may be considered. Figure 2.7 shows the transmission amplitude and reflection delay response of a single period Bragg grating device. The structure, as shown previously, exhibits a narrowband, high reflectivity stopband. The delay profile shows a small delay at the minima of the transmission spectra that increases away from the Bragg condition. This result is easily anticipated as it is clear that the radiation meeting the Bragg condition will be reflected strongly whereas away from this point the radiation will penetrate more deeply into the structure and consequently show a greater reflection delay time. If a linearly chirped Bragg grating is considered it has been shown that a broadened stopband is created, and it is expected that the group delay should follow a monotonic increase with wavelength. Figure 2.8 shows the characteristics of an unapodised

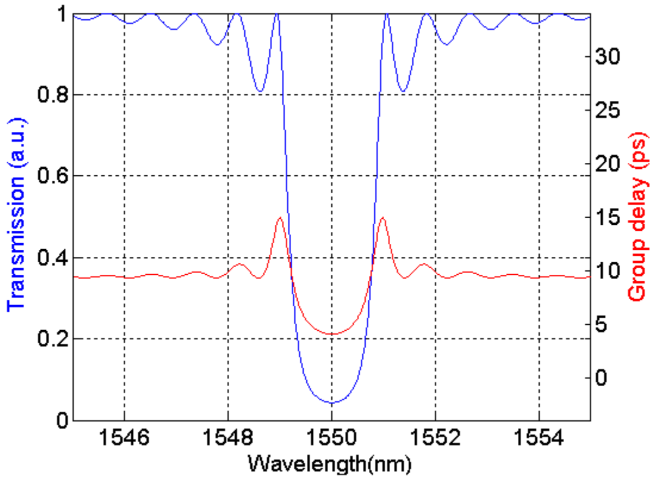

Figure 2.7: Transmission amplitude and reflection group delay profile for a single period Bragg grating.

linearly chirped Bragg grating. As before the widened stopband with significant ripple is evident. The group delay profile does indeed show an approximation to a linear variation across the stopband, though there is a significant ripple here too. The wide swing of group delay on either side of the stopband may be ignored as there is little power in the reflected mode at these wavelengths. So far it is only the Bragg condition that has been considered as a function of propagation length, although it was mentioned that the coupling coefficient, κ, may also be evaluated in this manner. By varying κ the coupling strength of the grating may be modulated as a function of z. However, there is a close link between κ, λ_B and τ_g through the solutions to the coupled-mode equations as shown in (2.2)-(2.6). Clearly the grating transmission and group delay cannot be modulated completely independently, though arbitrary T, τ_g profiles may be achieved through careful design. In many cases a smoothly varying κ function has been implemented in attempts to supress the sidelobes in constant κ grating responses [43]. This technique, of slowly varying the coupling coefficient from zero to a maximum and back again along the grating length, is equally applicable in chirped grating devices. The simulated response of an apodised CBG is shown in Figure 2.9. In Figure 2.9 it is clear that the apodisation has reduced the ripple of both the transmission spectrum and group delay profile. However, to design the more general gratings with arbitrary transmission and group delay characteristics more careful design must be carried out which is discussed more fully in Chapter 4.

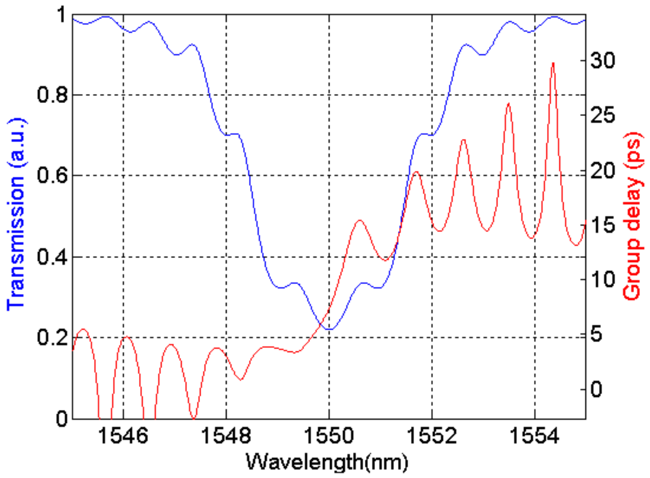

Figure 2.8: Transmission amplitude and reflection group delay profile for an unapodised linearly chirped Bragg grating.

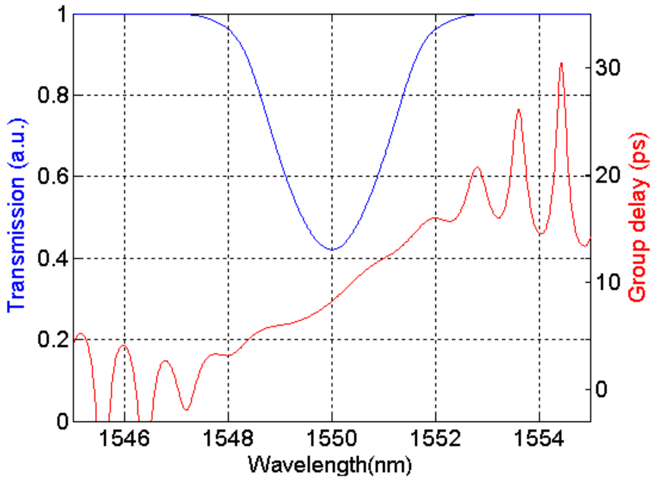

Figure 2.9: Transmission amplitude and reflection group delay profile for an apodised CBG.

2.5 Transfer matrix method for simulating coupled-mode solutions of a CBG structure

2.5.1 Matrix formalisation

As described in section 2.3 the complex propagation coefficient, q, and reflectivity coefficient, $r(q)$, of a CBG are functions not only of transmission frequency but also of z along the axis of propagation. This being the case, the fields in the grating cannot be solved for by simply considering the boundary conditions at the extents of the grating as was the case for single period gratings. As the values of q and $r(q)$ are functions of z so then are the interdependent constants A_1 and B_2. Figure 2.10 shows a schematic of how the grating device may be divided into slices, each much smaller in length than the total grating dimension, and so the grating may be considered as a piecewise representation of the continuous whole. Therefore, rather than a solution derived from constant grating response along its length and fixed interdependent constants a discretised solution may be sought to solve each δz slice of the structure in a piecewise fashion, the product of these solutions approximating to the real solution of the grating structure. One method by which to approach this problem is to use a matrix formalisation, providing a transfer matrix method (TMM) model that covers the changing properties of the grating along its length and hence the solution only relies on the transfer matrix

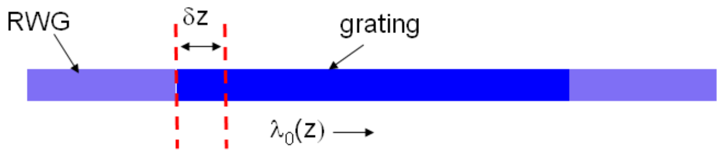

Figure 2.10: Matrix approximation to a continuously chirped grating.

and the conditions at each extremity of the grating, which are known. From (2.3) and (2.4), the conditions at $z = 0$ may be calculated as before. In order to solve for the forward and backward waves using a matrix formulation the grating must be represented as a series of small grating sections, δz, of finite length and constant pitch, with the chirp introduced as changing pitch between sections. The solutions at the end of the first grating increment may be written as:

$$A(\delta z) = A_1 e^{-jq\delta z} + r(q) B_2 e^{jq\delta z} \tag{2.9}$$

$$B(\delta z) = B_2 e^{jq\delta z} + r(q) A_1 e^{-jq\delta z}. \tag{2.10}$$

By substitution of the boundary conditions at $z = 0$ into (2.9) and (2.10) A_1 and B_2 may be solved for in terms of $A(0)$ and $B(0)$.

$$A_1 = \frac{A(0) - r(q)B(0)}{1 - r(q)^2} \quad , \quad B_2 = \frac{B(0) - r(q)A(0)}{1 - r(q)^2}$$

$$A(\delta z) = A(0)\left[\frac{e^{-jq\delta z} - r(q)^2 e^{jq\delta z}}{1 - r(q)^2}\right] + B(0)\left[\frac{r(q)e^{jq\delta z} - r(q)e^{-jq\delta z}}{1 - r(q)^2}\right] \tag{2.11}$$

$$B(\delta z) = B(0)\left[\frac{e^{jq\delta z} - r(q)^2 e^{-jq\delta z}}{1 - r(q)^2}\right] + A(0)\left[\frac{r(q)e^{-jq\delta z} - r(q)e^{jq\delta z}}{1 - r(q)^2}\right] \tag{2.12}$$

Naturally the solutions given above are valid only for the first grating increment as q and $r(q)$ vary with grating pitch. However, the constants for the proceeding section may be calculated with reference to the forward and backward waves at the end of the previous section. The result is a matrix formulation where each discrete section provides the input to the next. The equations for $A(\delta z)$ and $B(\delta z)$ may be recast in matrix form.

$$\begin{bmatrix} A(z_1) \\ B(z_1) \end{bmatrix} = \begin{bmatrix} \left(\frac{e^{-jq\delta z} - r(q)^2 e^{jq\delta z}}{1 - r(q)^2}\right) & \left(\frac{r(q)e^{jq\delta z} - r(q)e^{-jq\delta z}}{1 - r(q)^2}\right) \\ \left(\frac{r(q)e^{-jq\delta z} - r(q)e^{jq\delta z}}{1 - r(q)^2}\right) & \left(\frac{e^{jq\delta z} - r(q)^2 e^{-jq\delta z}}{1 - r(q)^2}\right) \end{bmatrix} \begin{bmatrix} A(0) \\ B(0) \end{bmatrix} \tag{2.13}$$

If the transfer matrix in (2.13) is H_1, then H_n for the n^{th} section is calculated using the relevant functions for q and $r(q)$. Finally the forward and backward wave components at any point of the grating may be written as:

$$\begin{bmatrix} A(z_n) \\ B(z_n) \end{bmatrix} = \prod_{p=1}^{n} H_p \begin{bmatrix} A(0) \\ B(0) \end{bmatrix} \tag{2.14}$$

The utility of the matrix formalisation is further compounded by the ease with which variations in the coupling coefficient and gain parameter in the z direction may be implemented into the solution.

2.5.2 Convergence of transfer matrix method solutions over free parameter space

As with any computational simulation tool, care must be taken in the application of the TMM as it is a discretisation of the continuous physical world that is being sought to simulate. With the TMM model described in this work there is an obvious discretisation immediatly apparent as the grating structure, consistent of periodic variations in physical dimension, already performs a discretisation of the waveguide width function that is applied to modulate the effective index and hence Bragg wavelength of the device. Nevertheless this is not the only issue that needs attention with regards to this model. In simulation there are a number of particulars, that in their conflict, determine the characteristics of the final solution. These include the computational memory available both for calculation of the model and storage of the results, simulation time and of course accuracy of the model. In most cases there are a number of free parameters that may be set to give a reasonable trade off between accuracy and computational speed and cost. In the TMM model described here the free parameters, of the system are: $\Lambda_0, g, A(0), n_{eff}, \kappa, \Delta\beta$ and δz. However, since Λ_0, g and $A(0)$ are taken as constant in this work - although if varying, the first two would be discrete functions of z and the latter, $\Delta\beta$ - and n_{eff} and κ are functions varying with z, then the two discretisation dimensions are left as z and $\Delta\beta$. Therefore the model's utility may be assesed as a function of these two parameters.

Firstly, the fixed parameters of the model are given in Table 2.1. The fixed parameters were chosen to represent a grating with stopband centred at $1550\,nm$, and reasonably high reflectivity, matching the parameters of the material described in Chapter 4. For the discretisation of $\Delta\beta$ and z it was determined to set brackets on the desiged values and sample the response of the model at 25 intermediate values to assess the possible divergence of the model solutions with increasing discretisation step. The points to be used were generated using the pseudo-random number generator function in Matlab to span the bracketed interval, in the hope that this would isolate any periodic effects of the discretisation step that may become apparent in event of a harmonic relation between the sampled points. The upper and lower bounds of the discretisation dimensions for $\Delta\beta$ and z are given in Table 2.2. A further point to note is that the discretisation steps for z are given in terms of Λ_0, the grating period. It would be meaningless to sample the structure at less than the grating pitch, however, it is not necessary that the discretisation in the z dimension be multiples of this pitch, and in this study that is not the case. The TMM model functions, as previously described, by calculating the grating response for each discrete δz increment of the device, over the bandwidth under test. Therefore the discretisation of the two parameters, z and $\Delta\beta$, can be thought of in different physical terms. By discretising z the model is approximated to a

Table 2.1: Fixed parameters of TMM for convergence testing.

Parameter	Value
Λ_0	$250\,nm$
n_{eff}	3.1
κ	$50\,cm^{-1}$
L_g	$450\,\mu m$
g	0
$A(0)$	1

Table 2.2: Discretisation bounds for convergence tests.

Discretisation step	Lower Bound	Upper Bound
δz	Λ_0	$100 \times \Lambda_0$
$\Delta\beta$	$5\,m^{-1}$	$500\,m^{-1}$

sampled grating - one where the grating pitch is constant over small lengths, with grating pitch being variable between the sections - and therefore the simulated response will be affected consequently. However, the discretisation in $\Delta\beta$ is not a physical alteration to the simulation, rather a sampling of the grating response, and as such the main objective is to ensure that the discretisation allows accurate description of the smallest features of the final device characteristics. For the case of a single period grating the TMM model was compared with the direct solution of the coupled-mode equations over the full grating length, L_g, first holding $\Delta\beta$ constant at $10\,m^{-1}$ and varying δz, then holding δz constant at $2 \times \Lambda_0$ whilst varying $\Delta\beta$. It was not possible to set the constant parameter at the lower end of their brackets as intended as this exceeded the memory capacity of the personal computer being used for the simulations. As expected the discretisation of z did not vary the final fields calculated from the full grating length solution. This is obviously the case as although the grating is solved for in a piecewise manner the solution does not vary along the propagation length and so any discretisation in z is merely equivalent finally to the full grating length solution. In the case of $\Delta\beta$ discretisation, within the bracketed limits, the amplitude error was less than $0.5\,\%$ and the phase error less than $0.2\,rad$.

Unlike the single period grating case, in a chirped grating simulation the discretisation in z is expected to yield varying results for the calculated fields, as the grating parameters are modulated over the propagation length and therefore sampling these points at various rates produces differing approximations to the device. One additional point to note is that in these sampling schemes the final grating length is not constant over all of the simulated cases. This is the case as each δz is not necessarily a multiple of the intended grating length and therefore the final length may be in error by as much as a sampling length. Figure 2.11 shows the calculated transmitted and reflected fields from a linearly chirped grating with varying δz in the solver. Comparing the results with the smallest discretisation length, it is clear that there is some variation in the field amplitude but it is the phase that shows significant variation especially at longer wavelengths, away from the central Bragg condition. The maximum error with discretisation length is shown in Figure 2.12, where the errors in transmitted and reflected field powers exactly overlap in the plot. The error in field amplitude increases to $1.5\,\%$, where the error in transmitted and reflected fields is equal. However, the maximum error in the phase extends up to $15\,rad$, although the mean error (while following the

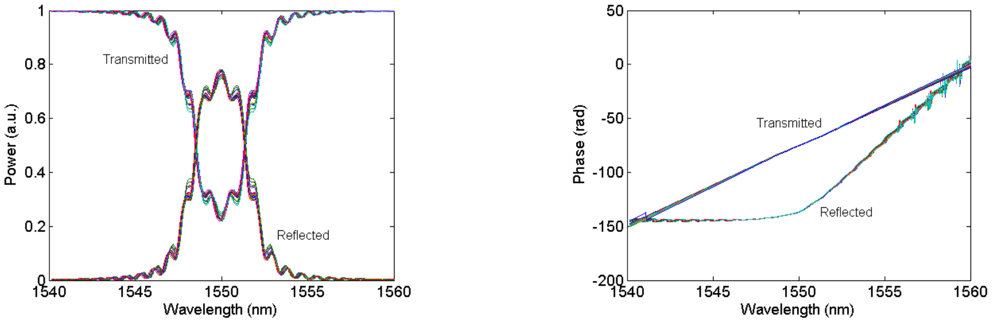

(a) (b)

Figure 2.11: Simulation of transmitted and reflected fields from a linearly chirped grating (a) power , (b) phase, with varying δz $(\Lambda_0 \rightarrow 100 \times \Lambda_0)$.

same trend with δz) remains less than $2\,rad$. The mean error is calculated for each value of δz as the arithmetic mean of the function error with wavelength. It may be noted that the error does not uniformly increase with increasing δz. This is an artifact of the point noted about variable grating length explained previously. Although the grating length is variable about the designed length, and so results in errors commensurate with consequently different device lengths that are not uniformly removed from the true length, the trend in error clearly shows the tendency to increase with increasing δz independent of these local variations.

Figure 2.13 shows the calculated transmitted and reflected fields from a linearly chirped grating with varying $\Delta\beta$ in the solver. Clearly the matching here is very

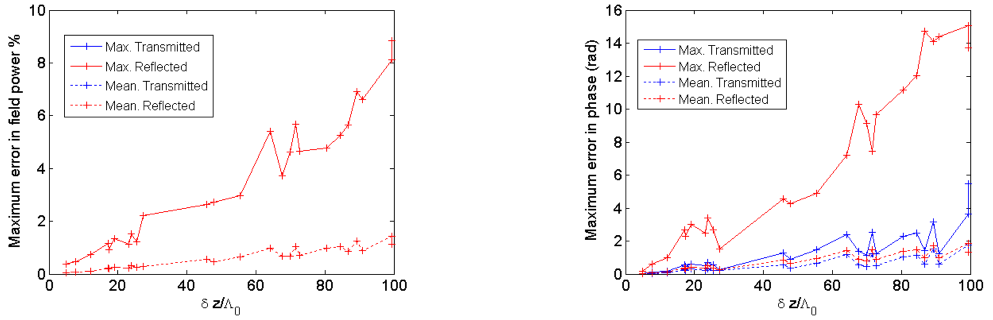

(a) (b)

Figure 2.12: Error relative to simulation of a linearly chirped grating with finest discretisation grid for (a) power (where the transmitted and reflected plots overlap), (b) phase as a function of discretisation step δz.

good, as was anticipated since the response is simply being sampled in the frequency domain. The maximum amplitude error was found to be less than $2\,\%$, while the phase error did not exceed $0.2\,rad$. The fact that there is any error at all stems from the matching of the lower sampled frequencies to the reference system that is not necessarily a harmonic of the sampling frequency.

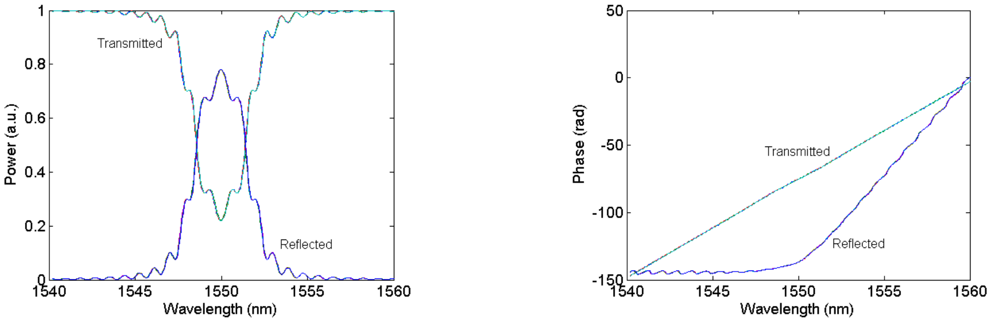

(a) (b)

Figure 2.13: Simulation of transmitted and reflected fields from a linearly chirped grating (a) power, (b) phase with varying $\Delta\beta$ $(5m^{-1} \rightarrow 500m^{-1})$.

In addition to the linearly chiped grating, a non-linearly chirped grating with z-dependent coupling factor was also simulated to assess the performance of the model with varying discretisation in z and $\Delta\beta$. Figure 2.14 shows the calculated transmitted and reflected fields from the non-linearly chirped grating, with varying δz in the solver. Again it is clear that there is some variation with increasing δz, though the same caveats apply here as in the linearly chirped grating case. As

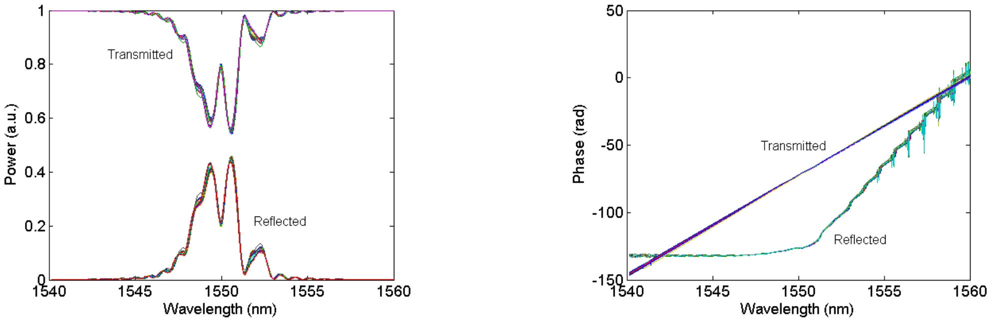

(a) (b)

Figure 2.14: Simulation of transmitted and reflected fields from a non-linearly chirped grating (a) power, (b) phase, with varying δz $(\Lambda_0 \rightarrow 100 \times \Lambda_0)$.

before, the maximum errors in both amplitude and phase of the transmitted and reflected fields are presented in Figure 2.15, with the non-increasing variation again rooted in the juxtapostion of designed and simulated grating lengths. The maximum field amplitude error does not exceed 6 %, and the maximum phase error is below 22 rad, with respective mean errors of below 0.8 % and 2 rad. Similarly

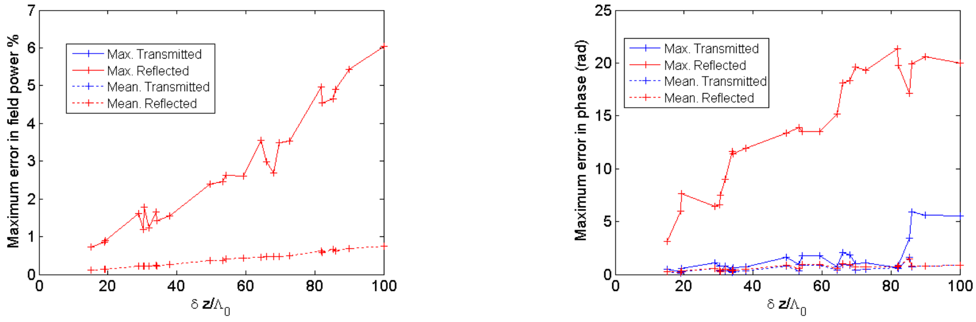

(a) (b)

Figure 2.15: Error relative to simulation of a non-linearly chirped grating with finest discretisation grid for (a) power (where the transmitted and reflected plots overlap), (b) phase as a function of discretisation step δz.

in the case of the variation in sampling of $\Delta\beta$, Figure 2.16 and Figure 2.17 show the close agreement for all sampling values of $\Delta\beta$ within the predefined brackets.

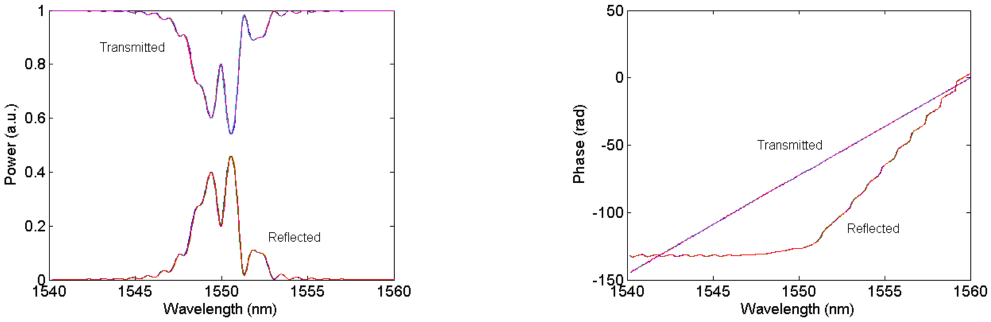

(a) (b)

Figure 2.16: Simulation of transmitted and reflected fields from a non-linearly chirped grating (a) power, (b) phase, as a function of discretisation step $\Delta\beta$ ($5m^{-1} \rightarrow 500m^{-1}$).

So, from the above results it is clear that the TMM model is consistent over a range of values with deviation from the most closely sampled solution emerging

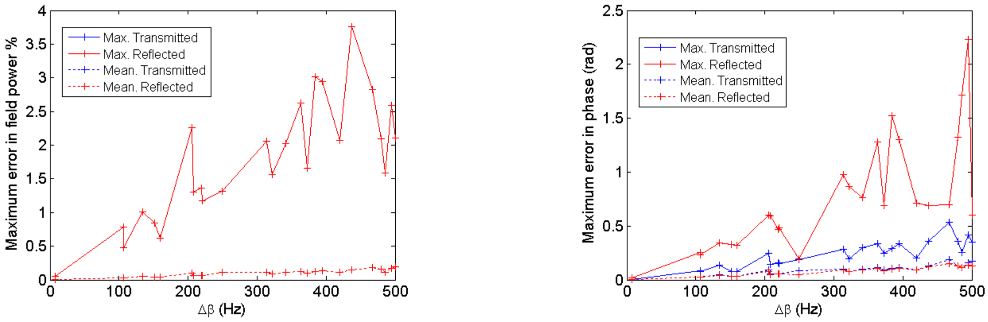

(a) (b)

Figure 2.17: Error relative to simulation of a non-linearly chirped grating with finest discretisation grid for (a) power (where the transmitted and reflected plots overlap), (b) phase as a function of discretisation step $\Delta\beta$.

with increasing δz. With simulation times not exceeding a few minutes, and with the previous limits discussed for δz, and $\Delta\beta$ due to memory constraints, the final discretisation lengths that were used in the simulation work for this thesis were set at $\delta z = 1 \times \Lambda_0$ and $\Delta\beta = 10\, m^{-1}$.

2.6 Conclusions

In this chapter solutions to the coupled-mode wave equation were extended to include the effects of chirp in the Bragg condition of the integrated Bragg gratings under discussion. It was shown that not only could a z-dependent effective grating pitch be incorporated into the solutions but also varying functions of κ, illustrating the potential for control over both grating chirp and apodisation. In addition a Transfer Matrix Method model of arbitrarily chirped and apodised gratings was derived and presented, along with analysis of its relative accuracy.

Chapter 3

Tapered Waveguide, Sidewall Gratings

In the preceding chapter it was shown that integrated Bragg grating devices may be designed to incorporate z-dependent functions of Bragg wavelength and coupling coefficient in order to produce devices with arbitrarily defined amplitude and phase characteristics. Although it was illustrated numerically that these structures may behave as designed, little attention was paid to the physical design of the device. The introductory chapter of this work presented a number of current techniques by which linearly chirped gratings are fabricated, though these devices were limited to linearly chirped gratings often requiring the application of re-growth techniques. In this work then it is the intention to design a grating structure that may be fabricated fully post-growth, whilst retaining flexibility enough to produce the arbitrary functions of λ_B and κ.

3.1 Physical structure

In order to address the problems associated with current integrated CBG designs - as described in the introduction - whilst still maintaining their advantageous characteristics, a fully post-growth fabricated CBG device is presented here. The integrated CBG device is based on a tapered waveguide sidewall grating structure that is both fabricated entirely post-growth and produces a continuous chirp in the grating period; excluding of course the inherent discretisation associated with the grating pitch periodicity. A schematic of the proposed device structure is shown in

Figure 3.1. In addition to the continuous chirp and apodisation profiles that may be induced with the sidewall grating geometry there is the further advantage that the proposed device structure allows for current injection along its length. With the grating modulation restricted to the waveguide sidewalls the top surface of the waveguide is left free for electrical contact.

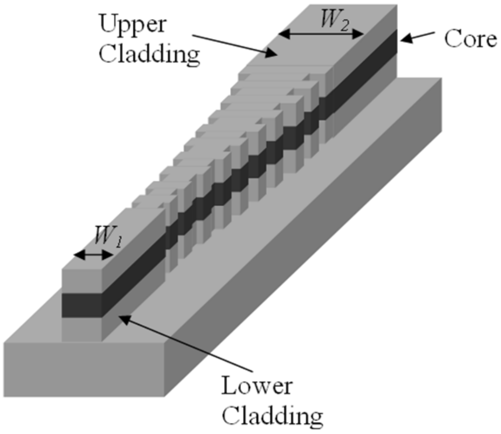

Figure 3.1: Schematic of the integrated CBG device.

3.1.1 Tapered waveguide design

In order to produce chirp in integrated CBGs it has been shown that current techniques rely either on complicated direct write schemes to vary the longitudinal grating period, or resort to discrete approximations to continuously chirped gratings such as step chirped or multiphase shifted geometries. In order to create continuous chirp, whilst still adhering to standard, current lithography and fabrication technologies, the Bragg condition may be revisited. Recalling that:

$$\lambda_B = 2n_{eff}\Lambda_0$$

for a 1^{st} order Bragg grating, it is clear that to vary the Bragg wavelength the obvious method is to vary the longitudinal pitch of the grating. However, if the longitudinal pitch is held constant then from the Bragg condition it is clear that to vary the Bragg wavelength in this case it is necessary to modulate the effective index of the mode. By attacking the problem in this way the necessity to construct delicate methods by which to modulate the longitudinal grating pitch - in the order of $< 1\,pm/period$ - may be circumvented. As a result only a single grating period is required, something that is well established in E-beam lithography.

The next issue is the matter of how to modulate the effective index of the waveguide mode. There are a number of methods by which this may be achieved. A Sub-Wavelength (SW) grating may be written into the waveguide where the effect of the grating is to modify the effective index experienced by the mode due to the sub-wavelength features of the waveguide [44]. To achieve this effect it is necessary that $\lambda_B < \lambda_0$. In the case where the Bragg wavelength is less than the wavelength of the incident light the mode effectively sees a homogeneous medium the index of which is the integral effect of the media comprising the grating. A schematic of a SW grating device is shown in Figure 3.2. With constant grating duty-cycle the SW grating introduces a waveguide region where the effective index of the mode is less than that of the unprocessed slab region. In order to create a variation in the modal index that is dependent on the spatial position along the propagation direction in the waveguide, the duty cycle of the grating must be modulated, as shown in Figure 3.3. There are some complications with the SW grating method of modulating the effective modal index. First, the SW grating itself is written directly into the waveguide core and then the upper cladding layers overgrown. As outlined previously, overgrowth fabrication procedures are sensitive processes and it desired to avoid them in this work if possible. There is obviously the prospect of deeply etching a post-growth patterned SW grating into the waveguide where the air trenches would serve as the modulating media. Deep etching the trenches may be difficult given that the modulation of the modal index

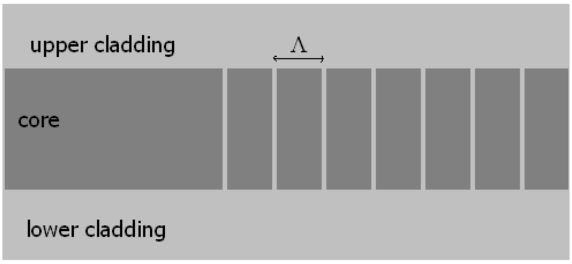

Figure 3.2: Sub-wavelength grating.

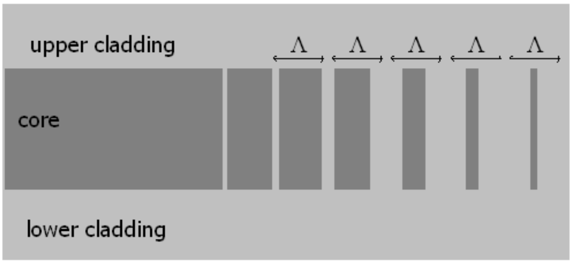

Figure 3.3: Varying duty-cycle sub-wavelength grating.

is related to the duty-cycle of the SW grating, and the precise control over trench widths required may be confounded by effects of Reactive Ion Etching (RIE) lag present in dry etching such structures [45]. Also, a second difficulty of using this technique in the current work is apparent. The modulated index is to be used in conjunction with a single period Bragg grating. So in effect the waveguide would be subject to the fabrication of two grating structures that must be somehow fabricated in the same region. The compound grating fabrication is clearly not a straight forward task.

Another possible method for varying the waveguide index is to vary the etch depth, D, of the ridge along its length, as illustrated in Figure 3.4. As the depth of the ridge increases the modal confinement in the lateral direction is enhanced and the mode sees a lower effective index. This modulation is not easily fabricated and with the non-linear variation of n_{eff} with D, the effective index variation to be modelled given the Bragg condition chirp is not easily created. There is also

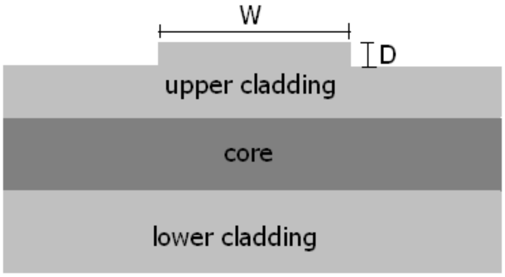

Figure 3.4: Varying modal index with etch depth D.

the problem that the varying etch depth will modulate the coupling coefficient of the Bragg grating to be written, this effect is discussed more fully later. Also as the grating design that will be implemented in this work is based on a deeply etched sidewall geometry the varying etch depth index modulation is completely unsuitable.

Finally and undoubtedly most simply, the modal effective index may be varied by modulating the waveguide width. The effective index of the 0^{th} order waveguide mode is related to the waveguide width, W. Therefore by modulating the width of the waveguide along the propagation direction the local modal index may be controlled. A major benefit of this technique is that it is easily applicable with conventional lithography methods and requires no extra processing steps in addition to the waveguide definition procedure. There are a couple of factors however that require attention in association with this method. The first is that the local taper profile of the waveguide should not perturb the lateral confinement of the mode in such a way as to significantly couple into other waveguide, cladding or radiation modes. Also, the rate of change of modal index is not a constant with regards to waveguide width, unless only a small range of values is considered. Therefore, the modulation of the index with width must be taken into account when designing dispersive devices so that the correct profile is calculated for a given dispersion characteristic.

As will be discussed in the next section the devices considered here are based on deeply etched waveguide structures. The effective index of the fundamental mode with respect to the waveguide width may be calculated using a mode solver program to simulate the given waveguide geometry. Figure 3.5 shows a schematic of the proposed tapered grating design, with a linear taper from width W_1 to W_2. The sidewall gratings have a 50 % duty-cycle and a recess depth of d. In the case of the device in Figure 3.5 the bandwidth over which it operates may be calculated given the widths W_1 and W_2 which translate to effective modal indices and hence Bragg wavelengths. Figure 3.6 shows the refractive index of the fundamental TE mode of a deeply etched waveguide on the material structure defined in Chapter 4. So, by varying W_2 - with respect to a constant W_1 - a non-linearly increasing bandwidth is achieved proportional to the increasing effective index of the waveguide at W_2. Clearly for a small difference between W_1 and W_2 the relationship is approximately linear, meaning that a linear chirp in the grating may be induced by a linear variation in waveguide width. However, as W_2 increases

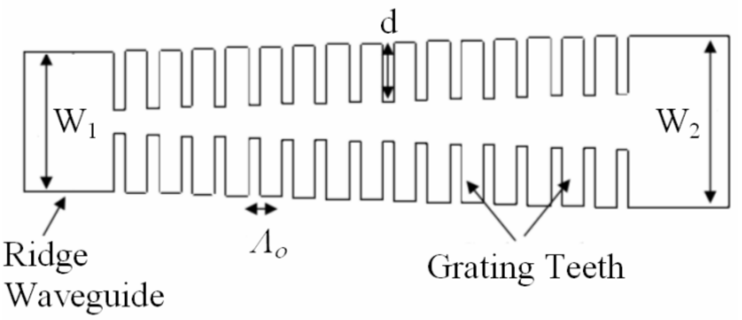

Figure 3.5: Schematic of a tapered Bragg grating device.

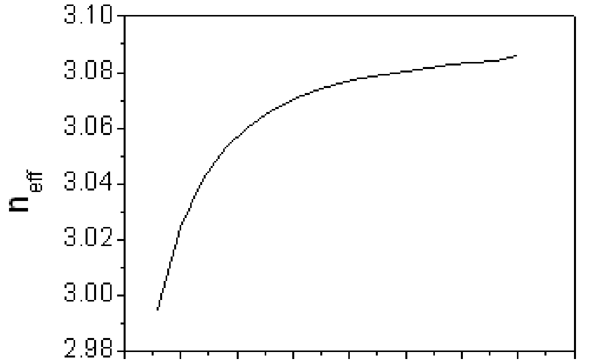

Figure 3.6: Effective index of fundamental TE mode with waveguide width.

the associated effective index tends towards a limit - that of the slab waveguide - that ultimately limits the useful bandwidth of the device. When considering grating designs for large bandwidth linear chirp, or non-linear chirped functions it is necessary to include the effects of both recess depth and waveguide width on the effective index of the waveguide mode. As shown in Chapter 2 the grating chirp may be expressed as a function of effective index, that in turn is dependent both on waveguide width and recess depth. This method of modeling chirp invokes an additional response in the coupling coefficient so that the waveguide width and recess depth may be offset to produce the required effective index and coupling coefficient pair. This is discussed in more detail in Chapter 4.

3.1.2 Deeply etched sidewall gratings

Now that a method for varying the Bragg condition of the single period grating has been defined it is necessary to design the form of the grating itself. The major design considerations are the resultant coupling coefficient obtained from the grating geometry and the ability to fabricate the design post-growth and with well established lithographic techniques.

Sidewall gratings were selected as they are easily fabricated using E-beam technology and RIE tools in a fully post-growth system. The concern then is the magnitude of the coupling coefficient available from such a geometry. As outlined in section 2.3, by introducing a chirp into the grating the reflectivity becomes a funtion of $\Delta\beta, \kappa$ and L_g. In the case of single period gratings the reflectivity may simply be calculated as a function of the κ value and the length of the grating.

$$R = tanh^2(\kappa L_g) \tag{3.1}$$

From (3.1) it was found that for a reflectivity of $> 30\,\%$ a κ value of approximately $10\,cm^{-1}$ for grating lengths of a few hundred microns is derived. However, as the grating structure under scrutiny here is chirped, and so its reflectivity is now a function of its bandwidth and length, the required coupling coefficient to maintain the necessary reflectivity over the grating's entire bandwidth is also increased. The method by which this coupling coefficient may be estimated is through iterative simulation of the grating device varying the coupling coefficient. For III-V based grating structures it was calculated that the coupling coefficient necessary for

$> 30\,\%$ reflectivity over a device bandwidth of a few nanometres is in the order of a few tens cm^{-1} for gratings of hundreds of microns in length. It was shown in Chapter 1 that other groups have achieved high coupling coefficients by writing the grating variation directly into the core material and thereby confining a large proportion of the modal power to the grating. However, since it is required to produce structures in a post-growth environment another method was sought. The alternative is to write deeply etched sidewall gratings. An examination of the relationship between the grating geometry and the coupling coefficient will illuminate the reasoning behind this strategy.

In section 2.2 it is shown that the grating coupling coefficient κ can be expressed as the following:

$$\kappa = \frac{(n_2^2 - n_1^2)\Gamma_{x,y}}{2n_{eff}^2\Lambda_0}. \tag{3.2}$$

(3.2) shows that the coupling coefficient is dependent on both the variation of index between the waveguide structure and the recessed area and the confinement factor of the mode to the grating. Taking the variation of index first, in the case where the grating is written into the core material, the index difference is between the material index of the core and upper cladding. In the case of sidewall etched gratings the index variation can be considered as between the effective index of the unperturbed waveguide and that of air. The second, and much larger variation is then desirable for strongly coupled gratings. However, in shallow etched gratings the proportion of the mode confined to the grating cross-section is relatively low, negating the effect of the strong index perturbation. Figure 3.7 shows the effects on sidewall grating characteristics produced by variation of the ridge etch depth, D. The device simulated was of $1.5\,\mu m$ width and $100\,nm$ recess depth. From Figure 3.7 the grating Bragg condition is shown to vary with D, as the modal effective index changes given the waveguide geometry. The change in λ_0 is relatively rapid as the device is etched through the upper cladding and core, with a stable value being observed for geometries etched down into the lower cladding. The etch depth of the ridge is determined by the reactive ion etching processes involved in fabrication that are subject to errors in the range of $\pm 50\,nm$. Given that control over the Bragg condition is crucial to the device operation, designing the grating to be etched into the lower cladding should provide good robustness with respect to the achieved etch depth. Figure 3.7 also shows the relation of κ to the ridge etch depth. Again, the variation of coupling coefficient shows the

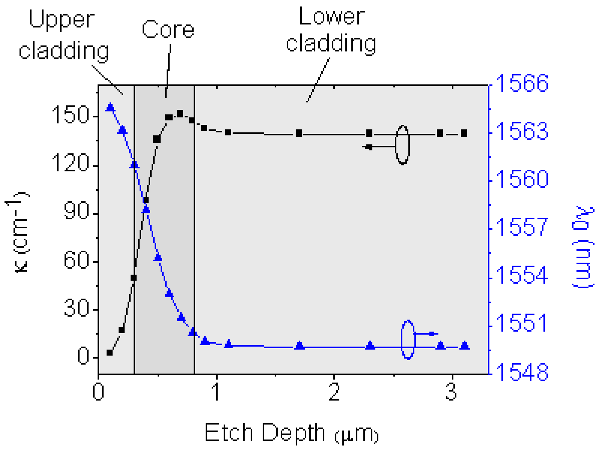

Figure 3.7: Grating coupling coefficient and Bragg wavelength as a function of ridge etch depth, D.

greatest gradient through the upper cladding and core layers. This suggests for robust design transcription, etching into the lower cladding - which also produces high values of κ - should be used. There is another interesting point to note from these results. It seems that κ peaks at some point where the ridge is etched to the lower edge of the core, before settling at a slightly lower value through the lower cladding. This may be explained by recalling that the coupling coefficient is determined both through the grating index modulation and the confinement factor of the mode to the grating area. By etching into, but not through the core, a large portion of the propagating mode sees the grating, as is the case for devices etched into the lower cladding. However, the mode is less confined in the lateral direction for shallower etches, allowing a greater proportion of the modal power to interact with the grating. Given these observations, it is desirable then to investigate devices etched into the lower cladding, denoted from here on as deeply etched structures.

A schematic of the overlap of the mode with deeply etched sidewall gratings is shown in Figure 3.8. Further simulations of the grating coupling coefficient were carried out to verify the thesis of enhanced κ due to the deeply etched sidewall grating geometry. The simulations were carried out by first calculating the modal profile of the unperturbed waveguide, using the FIMMWAVE mode solver package, and then using an overlap integral to calculate the confinement factor of the mode to the grating cross-section. An example of the κ values calculated for a

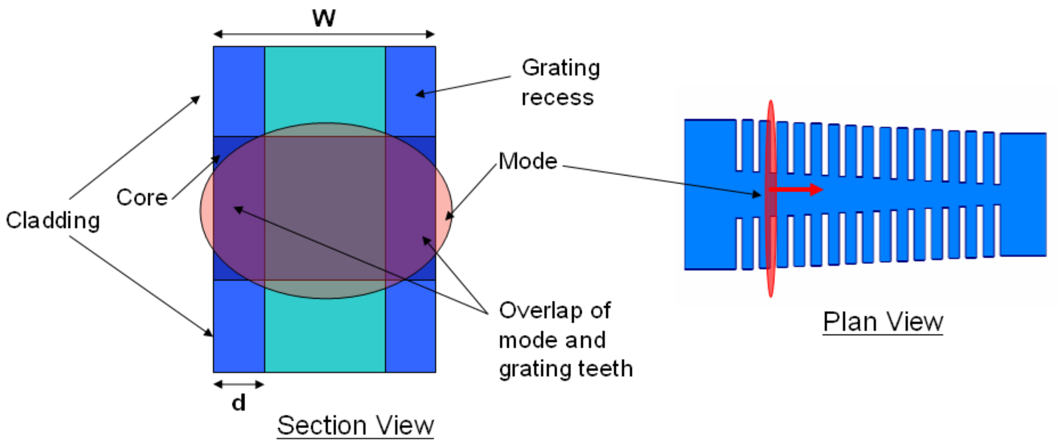

Figure 3.8: Modal confinement to grating cross-section in a deeply etched sidewall grating structure.

III-V material waveguide system is shown in Figure 3.9 for a number of waveguide widths. As would be expected due to the greater confinement of the mode with increasing waveguide width the coupling coefficient diminishes accordingly. However, the high κ values necessary for application in integrated CBGs are obviously attainable with this device geometry.

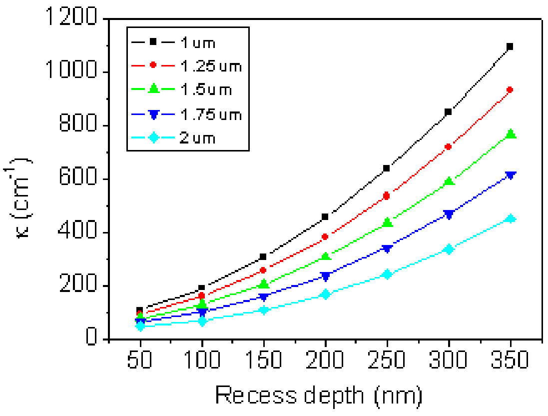

Figure 3.9: Coupling coefficient as a function of grating recess depth and waveguide width.

So in summary, an integrated chirped Bragg grating is presented based on a tapered deeply etched sidewall grating geometry. The major benefits of this device structure is that it may be fabricated using currently available lithographic and RIE techniques and is based on fully post-growth fabrication procedures. In addition the tapered waveguide design means that the grating chirp is induced in the effective modal index rather than the spatial grating period. The effective index modulation, being created by a varying waveguide width, may be tailored easily not only to linear dispersion designs but also higher order dispersion profiles that are unattainable with other methods. The deeply etched sidewall gratings produce the high coupling coefficients required for CBG applications without recourse to overgrowth methods, and also allow for modulation of the κ value via the grating recess depth.

3.2 Fabrication of integrated chirped Bragg gratings

The grating structures detailed in section 3.1 were produced in this work in a variety of contexts, from simple passive grating structures to inclusion in Distributed Feedback (DFB) lasers. Nevertheless, the fabrication method over all the devices was constant. First the grating pattern was exposed using E-beam lithography and subsequently transferred into the semiconductor material via RIE processes.

3.2.1 Lithography

In the manufacture of integrated optoelectronic devices there are two main lithography techniques that are widely employed; namely photolithography and Electron Beam lithography. The decision on which method to use is based on a number of considerations such as the feature size to be defined, the number of samples to be produced, the required flexibility in the design stage, the size of the area to be written, the exposure time and the cost of production. Both methods, if the process requires pattern transfer into a hard mask, will use similar Reactive Ion Etching steps after the transfer of the mask pattern into the resist or soft mask. The main distinction then is the method of transferring the mask into the resist.

Photolithography

Photolithography uses a pre-patterned mask plate that carries the desired features to be transferred onto the semiconductor. The sample is spun with photosensitive resist and baked to evaporate the solvents. There are a number of different methods of transferring the mask details into the resist depending on the specific application; however, the main mechanism is the same. A light source is shone through the mask, and any other processing optics required, and exposes areas of resist. The resist exposed to the light is molecularly altered so that on development the developer solution will only react with either the exposed or unexposed areas. The developer solution clears the unwanted resist leaving only the information from the mask plate transferred into the photoresist. Subsequently the sample can be processed using reactive ion etching depending on the application.

Photolithography is the technology of choice for large scale production as many features or devices may be written simultaneously using a single mask. An entire wafer can be manufactured in a single run with the exposure time limited only by the reaction of the photoresist. However, the resolution of the photolithography is limited by the diffraction limit of the illumination. Currently UV and deep UV sources are common in photolithography processes and can achieve feature sizes of under a micron [46, 47]. There are a number of limiting factors to the photolithographic techniques however. The speed of the system is partially due to the single mask that is used in the processing cycle. The drawback of using a mask is that if any modification is required in the pattern an entirely new mask must be fabricated, meaning that while ideally suited to large scale, consistent fabrication, photolithography is less appropriate for research work involving many different mask designs. Also, as stated, the feature size of the pattern is limited to close to a micron whereas many optical structures require features with dimensions significantly smaller than this limit.

Electron-beam lithography

An alternative to photolithography is Electron Beam lithography. Rather than using a mask to define the exposed areas of resist the E-beam writes onto the surface directly exposing the required areas. Clearly this is a much slower process than the photolithography since the pattern is serially written. There are some significant benefits to be garnered from this technique however. Firstly, the pattern is easily created and modified using CAD packages which quickly produce new designs that can be implemented in short time scales allowing feedback of results into fabrication processes. Current E-beam technology provides the opportunity to create feature sizes into the nanometre range [48]. With this ease of modification and flexible nanometre scale device definition E-beam lithography is an attractive option for the production of sub-micron scale optical structures in both commercial and research environments and as such is the technique of choice in the current work.

3.2.2 E-beam resists and reactive ion etching

The final objective of creating three dimensional structures in semiconductor materials can be viewed from two different perspectives. Firstly, the two dimensional pattern to be created must be applied to the surface of the material; this is dealt with by the lithographic techniques discussed previously. Secondly, a method must be sought by which selective removal of the semiconductor material will create a depth profile in the material. Clearly it is necessary to use the lithography to create a two dimensional pattern that is then etched into the semiconductor material. From the different perspectives described it is clear that the constraints on the method require a layer that is receptive to lithography and a subsequent process that will selectively etch the material under the pattern.

There are a number of common resists used in conjunction with E-beam lithography, but it is poly(methyl methacrylate), PMMA, that will be considered as an example here. The PMMA resist is spun onto the sample, exposed with the E-beam system and subsequently developed with MIBK:IPA solution to produce the pattern. The issue now is to transfer this pattern into the semiconductor. The selective etching of GaAs and AlGaAs is well covered in the literature [49–54], with a consensus that dry etching with $SiCl_4$ produces good sidewall verticality with a fast etch rate (typically a few hundred nanometres per minute). However, there is a conflict arising through the use of dry etching in conjunction with PMMA resist patterns in that the PMMA is quickly eroded by the $SiCl_4$. Therefore it is necessary to have an intermediate step so that the pattern is faithfully reproduced in the semiconductor material. One method of pattern transfer is to use a layer of PECVD silica as an intermediary hard mask for the etching of the semiconductor. A thin layer of silica (around $200\,nm$) is deposited onto the semiconductor and the

PMMA spun on top. The pattern is written into the PMMA as normal and then transferred into the silica by dry etching with CHF_3. The silica is used as a hard mask to etch the semiconductor as it is not greatly affected by the $SiCl_4$ etching process. The final process is shown in Figure 3.10. The double etching process required when using a silica hard-mask does produce sidewall roughness transferred from both the PMMA and silica masks into the semiconductor material. Another option for fabrication which may reduce the associated sidewall roughness and hence scattering losses is the use of a spin on glass, Hydrogen Silsesquioxane (HSQ), resist in place of the PMMA. The benefit of using this system is that upon development it produces a hard-mask for the etching of the semiconductor without the necessity for an intermediary silica layer, and so reduces the roughness associated both with the PMMA and the CHF_3 etching of the silica.

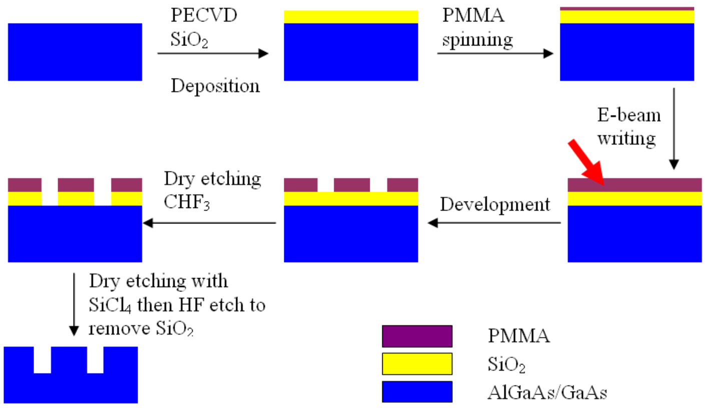

Figure 3.10: Fabrication procedure for pattern writing in AlGaAs/GaAs using PMMA based E-beam lithography.

PMMA is a positive photoresist - meaning that exposed areas will be removed from the mask on development. This being the case it is useful for opening contact windows, contact pad areas or marker patterns, as in these cases it is only small portions of the sample that need to be opened to the RIE or metal deposition processes. However, if it is used to define waveguides a narrow unexposed area must be left between adjacent exposed areas so that trenches are opened on either side of the waveguide on etching. This process is shown in Figure 3.11a. However, since PMMA is a positive resist, writing these two large exposed areas so close to one another causes problems with exposure of the waveguide pattern itself. When exposing resist with E-beam lithography the substrate backscatters electrons into

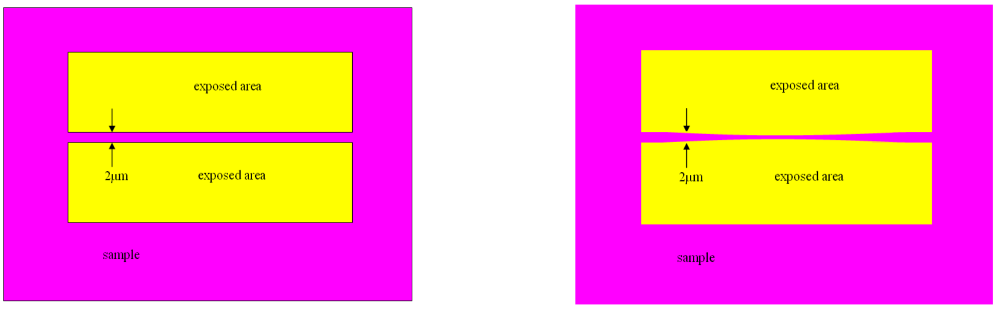

(a) (b)

Figure 3.11: Exposure of pattern to write $2\,\mu m$ waveguide in PMMA (a) ideal case (b) with proximity effect.

the resist, the radius of which exposure is related to the exciting beam voltage and substrate material. One effect of this process is the exposure of areas surrounding the focused spot due to the backscattering. If a large area is exposed then this background dose can cause warping of the pattern. In the case of a narrow strip surrounded by two large areas of exposure the causeway of resist may be bowed or even breached by the proximity effect, as shown in Figure 3.11b. The proximity effect problem may be remedied somewhat by applying a correction factor to the E-beam dose distribution in the pattern, with areas exposed to a high fraction of proximity dose given a reduced relative exposure. The proximity correction may be carried out using software associated with the E-beam lithography tool, but sensitive structures such as fine gratings are more difficult to produce in the light of this effect.

HSQ is a negative tone resist - the exposed areas are left after development - therefore writing small features such as waveguides and gratings is far more attractive in this system as compared to PMMA. A further benefit of using HSQ over PMMA for waveguide and grating fabrication is that it cuts out the requirement for an intermediate hardmask for etching the semiconductor material. The fabrication of waveguide devices using HSQ as the ebeam resist is shown in Figure 3.12. Aside from the simplified fabrication procedure of using HSQ there is also the issue of sidewall roughness losses associated with the deeply etched waveguides pursued in this work. The origin and quantification of these losses is detailed in section 3.3.1, where it is also illustrated that PECVD silica hardmasks introduce significant roughness into the etched semiconductor sidewalls. Some experiments

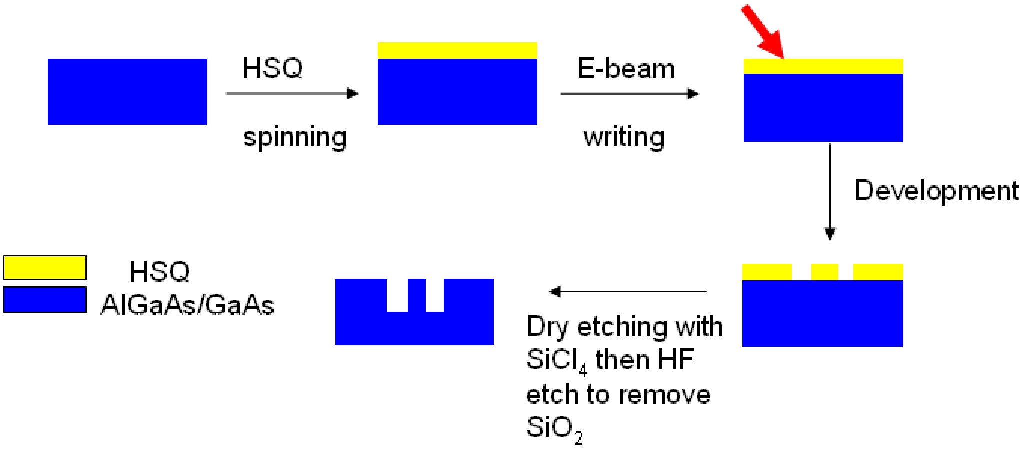

Figure 3.12: Fabrication of waveguide devices using an HSQ E-beam resist.

were carried out, using the Fabry-Pérot loss measurement system detailed in section 3.3.2, to find the waveguide losses of 2 μm waveguides fabricated with either the PMMA or HSQ methods. The losses using HSQ were 11.6 $dBcm^{-1}$ compared to the best case of 16 $dBcm^{-1}$ for the as-fabricated PMMA based guides. Clearly the HSQ resist offers a substantial benefit in terms of sidewall roughness loss reduction over the PMMA. So in conclusion, for waveguide and grating fabrication, HSQ resist is the obvious choice of fabrication route, where for fabrication of contact pad, current injection windows and marker lithography PMMA continues to be the more appealing option. An additional note may be made with regards to marker lithography in the light of fabrication using the Vistec VB6 electron beam tool. In this case markers may be patterned using HSQ as a mask for etched markers, by creating mesas with open square areas of approximately 50 μm in width. After etching these pits - generally $> 1.5\,\mu m$ is sufficient in III-V materials - the tool can find these edges fairly easily. One great advantage in using etched markers is that again the number of processing steps may be reduced as now the marker and first device lithography layers may be fabricated concurrently. Table 3.1 shows a comparison of the fabrication steps necessary for fabricating active devices using the soley PMMA based lithography and a mixture of PMMA and HSQ lithographic processes.

Table 3.1: Active device fabrication steps using either soley PMMA, or PMMA & HSQ lithography techniques.

Process	PMMA only	PMMA & HSQ
Marker & device lithography		✓
Marker lithography	✓	
Evaporation of markers & lift-off	✓	
Deposition of PECVD SiO_2	✓	
Device lithography	✓	
CHF_3 etching of silica hardmask	✓	
$SiCl_4$ etching of semiconductor	✓	✓
HF wet etch of mask	✓	✓
Deposition of PECVD SiO_2	✓	✓
Contact window lithography	✓	✓
CHF_3 etching of silica hardmask	✓	✓
Contact pad lithography	✓	✓
Metalisation of p contacts	✓	✓
Thinning	✓	✓
Metalisation of n contacts	✓	✓
Device cleaving	✓	✓

3.3 Loss Reduction Techniques for Deeply Etched Sidewall Grating Structures.

A major factor when considering aspects of fabrication techniques for optical structures is that of waveguide loss. There are a number of mechanisms through which energy can be lost on transmission through semiconductor integrated waveguides. Contributions to transmission loss are made by scattering loss, material absorption, free carrier absorption and losses due to surface state recombinations in active devices. A useful review of waveguide losses in III-V semiconductors is presented by Deri et al [55].

3.3.1 Sidewall roughness reduction via aqueous oxidation and selective oxide removal

Material loss, and free carrier absorption are clearly independent of the physical device fabrication - but may be addressed by other means as will be discussed shortly - scattering losses however are closely related to the physical device fabrication and are strongly related to issues such as the sidewall roughness and waveguide dimensions that are directly impacted by fabrication techniques. Sidewall roughness is a particular problem when considering waveguide propagation losses, especially where the structures are deeply etched. Payne and Lacey [56] give a relationship for scattering losses associated with ridge waveguides that shows high dependence on the r.m.s. roughness of the sidewalls and the waveguide width.

$$\alpha = \frac{\sigma^2}{\sqrt{2}k_0 d^4 n_{core}} g.f_e \tag{3.3}$$

Where α is the waveguide loss, σ is the r.m.s. roughness, d is the half-width of the waveguide ridge, k_0 is the free space wavevector, n_{core} is the refractive index of the waveguide core region and g and f_e are complex functions dependent on the waveguide material properties and the correlation length of the roughness. So, given that losses are proportional to the square of the sidewall r.m.s. roughness, it is apparent that fabrication techniques are required which produce smooth transcriptions of the pattern. The method of RIE steps outlined previously produces significant roughness of a few nanometres in scale, transferred from the PMMA and silica masks into the semiconductor.

One method of roughness reduction based on chemical oxidation and oxide removal has been proposed by Sparacin et al. [57] for application in Silicon on Insulator (SOI) systems. The oxidation front was found to be dependent on the material profile for the first few nanometres of formation before becoming a diffusion limited process, allowing preferential removal of areas of high positive cuvature. There is possibility of application in the AlGaAs/GaAs material system with papers by Houng's group [58–62] showing chemical oxidation processes for AlGaAs that may be applied.

Oxidation smoothing on Silicon-On-Insulator

Oxide smoothing of rough semiconductor surfaces has been previously pursued using gas-phase oxidation techniques with oxygen or steam at elevated temperatures [63]. Gas-phase oxidation process, although showing some promise with regards to reducing sidewall roughness also has a significant impact on the global waveguide dimensions. The gas-phase oxidation consumes a large portion of the waveguide and therefore is not particularly suited for applications where the structural dimensions are critical.

In work by Sparacin et al. [57] a novel sidewall roughness loss reduction technique is presented based on wet chemical oxidation of silicon (in Silicon-On-Insulator systems). The liquid-phase oxidation process promises a less consumptive method of oxidation, thereby retaining close agreement with as-fabricated dimensions. The basic theory is that in chemical oxidation reactions there are two main regimes. In the first the chemical oxidation process is highly dependent on the surface profile of the material. The profile limited oxidation is dominant in the first few nanometres of oxide generation, however after this the process becomes diffusion limited. In the diffusion limited regime the oxidation front proceeds uniformly across the sample irrespective of surface geometry, limited only by the diffusion of the reactant species through the existing oxide layer. Therefore, the authors interrupt the oxidation reaction whilst it is still a fast chemical reaction limited process and remove the oxide using an HF acid dip. The process is then repeated a number of times to reduce the waveguide sidewall roughness. The fast reaction limited process may be described by the Gibbs-Thomson relation.

$$\mu(\kappa) = \mu(\infty) + \gamma\Omega\kappa \tag{3.4}$$

Where $\mu(\kappa)$ is the potential at the material surface, κ is the surface curvature, $\mu(\infty)$ is the potential at a flat surface, γ is the surface energy, and Ω is the atomic volume. Essentially, the chemical potential of the surface is related to its curvature so that the areas of positive curvature, the roughness peaks, have greater chemical potential than those of negative curvature, the troughs. In this way the peaks of the roughness profile are more rapidly oxidised in this fast chemical limited process, and on removal of the generated oxide leave a smoother surface. The major advantages of this method of oxidation smoothing are that it may be carried out at room temperatures and that it only produces small amounts - in the order of nanometres - of oxide and thereby retains the global waveguide dimensions.

Results have been presented for waveguides of $0.63\,\mu m$ and $1.3\,\mu m$ widths [57], with losses being reduced by up to $7.3\,dBcm^{-1}$ and $0.6\,dBcm^{-1}$ respectively. The disparity in loss reduction, with similar smoothing of sidewall r.m.s. roughness may easily be explained with the Payne-Lacey function, given that the waveguide width has a dramatic effect on losses - with losses inversely proportional to the quartic of the waveguide width - so that the same amount of roughness reduction has a more beneficial effect on narrower waveguides. The second aspect of this work to highlight is the effect of the wet chemical oxide formation and removal on the roughness of the top surface of the waveguide. The top surface, as it has not been etched by RIE processes that lead to the roughening of the sidewalls, should be a relatively smooth surface. In both sets of waveguides the as-fabricated top surface roughness losses are of the order of $0.1\,dBcm^{-1}$ and increase to $0.6-0.7\,dBcm^{-1}$ after processing. The losses were calculated using measurements of the top surface roughness by Atomic Force Microscopy (AFM). The increase in top surface roughness may be explained by considering the effects of the topographically sensitive chemical oxidation process in its pre-diffusion limited regime. As stated earlier, in the fast chemical limited oxidation process the oxidation front is highly dependent on the profile of the surface, with sections of positive curvature being oxidised more rapidly than those of negative curvature. However, in the case of a relatively smooth surface this chemical potential gradient may act to roughen the surface by amplifying the potential profile through the selective oxidation and oxide removal. The significance of this result is to suggest that there is a limit to the smoothness achievable by wet chemical oxidation and oxide removal, that is reached from below in the case of the smooth top surface of the waveguides. Obviously this top surface roughening may be prevented by retaining the etch mask on the top surface, however it may lead to a minimum value of acheivable roughness on the waveguide sidewalls.

Wet oxidation smoothing of GaAs/AlGaAs

Oxidation in III-V materials is usually a wet thermal process that is diffusion limited, used to provide insulating areas in structures for current confinement or manufacture of waveguides and high index contrast structures. However, it is desirable for oxide smoothing loss reduction to harness a chemical oxidation technique in III-V materials equivalent to that presented by Sparacin et al. for SOI.

Houng's group has presented a wet chemical oxidation process for GaAs/AlGaAs that allows fast oxidation without recourse to wet thermal processes [58–60]. The main advantages of this are that no external energy source is required and that it may be carried out at low temperatures. The chemical solution used in their work was a dissolution of Ga into concentrated nitric acid that was then reduced to a pH of 4.5 by addition of ammonium solution and water. At a reaction temperature of 70^oC oxidation rates of up to $100\,nmhr^{-1}$ were achieved.

It was decided to use a variation of this oxidation process, yielding a much slower oxidation rate, as a parallel to the work done in SOI. The addition of Ga and the high reaction temperature were neglected in favour of a (nitric acid/ammonium solution/water), solution at room temperature that promised to yield an oxidation rate of approximately $14\,nm/hr^{-1}$. Using this figure, and assuming that a waveguide shrinkage of around $1\,nm$ per oxidation iteration was required to maintain a fast chemical reaction limited process, the iterations were set first at $3\,min$.

3.3.2 Loss and sidewall roughness measurement techniques

A batch of $2\,\mu m$ waveguides were produced on the passive $Al_xGa_{1-x}As$ (70:20:70)% wafer described in Chapter 4 using E-beam lithography into a PECVD SiO_2 hardmask and subsequent deep etching with $SiCl_4$. The waveguide losses were measured using the Fabry-Pérot measurement system. The surface r.m.s roughness was measured using the S4700 Scanning Electron Microscope (SEM) tool.

Fabry-Pérot loss measurement technique

To measure waveguide transmission losses a method based on the apparent Fabry-Pérot (FP) fringes in the transmission spectrum may be used. The transmission spectrum of a straight ridge waveguide is related to the reflectivity of its facets, the waveguide losses, refractive index and propagation length [55,64]. The transmission may be given as in (3.5).

$$T(\lambda) = \frac{(1-R^2)e^{-\alpha L}}{(1-Re^{-\alpha L})^2 + 4Re^{-\alpha L}\sin^2\left(\frac{2\pi n_{eff}L}{\lambda}\right)} \tag{3.5}$$

Where λ is the propagation wavelength, n_{eff} is the effective index of the propagting mode, R is the facet reflectivity, α is the waveguide loss, and L is the propagation length. For a straight waveguide this relationship, taken over wavelength, gives a fringe pattern in the transmission spectrum. The fringe contrast is taken as:

$$K = \frac{T_{max} - T_{min}}{T_{max} + T_{min}} \tag{3.6}$$

By some substitution an expression for the waveguide losses may be arranged in terms of the facet reflectivity and fringe contrast.

$$lnR - ln\alpha = ln\left[\frac{1-\sqrt{1-K^2}}{K}\right] \tag{3.7}$$

Sidewall roughness measurement technique

For each set of waveguides a set of plan view images of the waveguide edge were taken at a magnification of $180k\times$. In order to achieve a reasonable averaging of results a number of images were taken for each experimental set in a pseudo-random spatial distribution across the processed sample. An example of one such image is shown in Figure 3.13. There is a clear edge in Figure 3.13 that represents the boundary of the waveguide, however below this termination there is an apparent area of turbulence in the image. This area was found to be due to the image of the SiO_2 hardmask which does indeed show significant roughness, which is transferred to a smaller extent into the semiconductor material. After an HF dip this area shows significant improvement confirming that it is indeed the effects of the hard mask as the HF selectively etches the oxide.

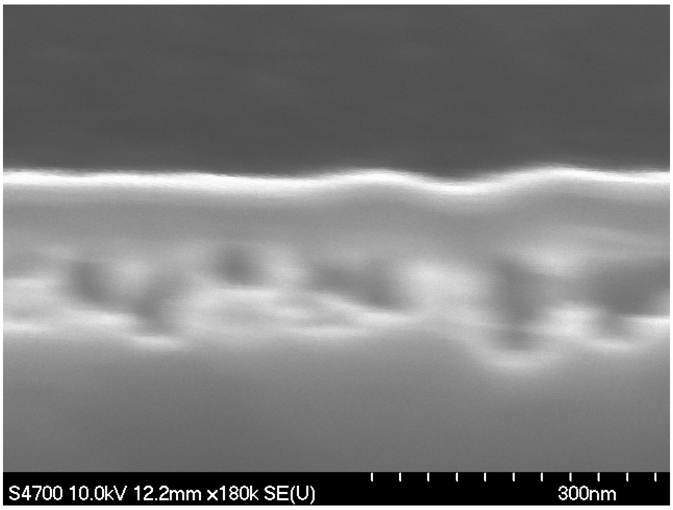

Figure 3.13: Edge of as-fabricated AlGaAs waveguide.

Once the images have been obtained they are processed to provide an average r.m.s. roughness for the sample. This is done using a MATLAB program that first of all creates a threshold for the image based on the contrast and polarises the output of each pixel to high or low with respect to this threshold as shown in

Figure 3.14. After polarising the image the routine searches for the edge between the high and low areas of the image. This should correspond to the waveguide edge in well captured images. The edge detection is illustrated by the green lines in Figure 3.14 and 3.15. Figure 3.15 is a greatly enlarged rendering of a section of Figure 3.14 showing the individual allocation of each pixel with respect to the threshold. Clearly the edge detection is not perfect and subject to spurious highs created by the image processing of the SEM image. This is only apparent on a very small scale however it is corrected for nonetheless by applying a smoothing routine to the detected edge to cut out any loops or spikes that are artefacts of the previous processes. Finally the edge is filtered to remove high frequency noise due to the pixelation of the image, the result of which is shown in Figure 3.16.

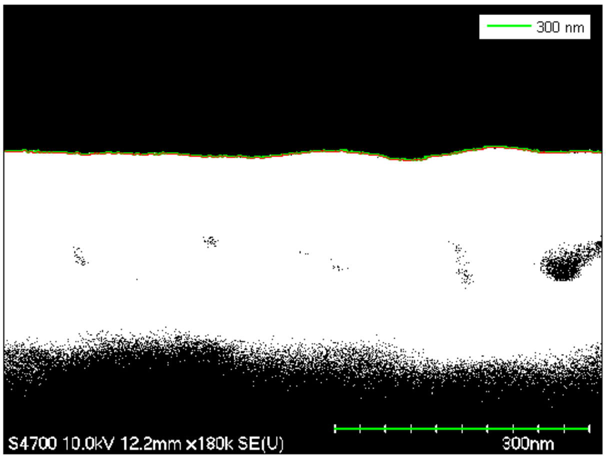

Figure 3.14: Roughness image after polarisation around a threshold value.

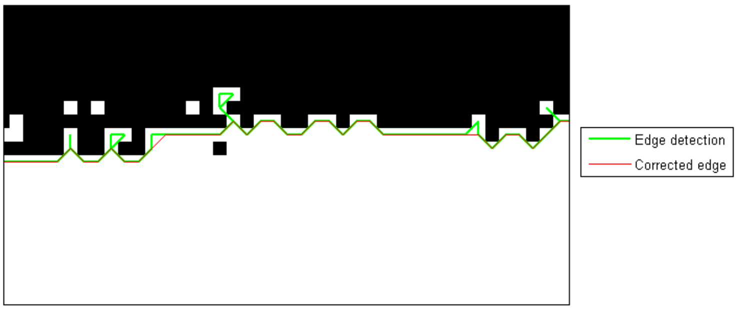

Figure 3.15: Enlargement of waveguide edge after edge detection and correction.

The r.m.s. roughness thus calculated is averaged over the range of images taken for each processing run.

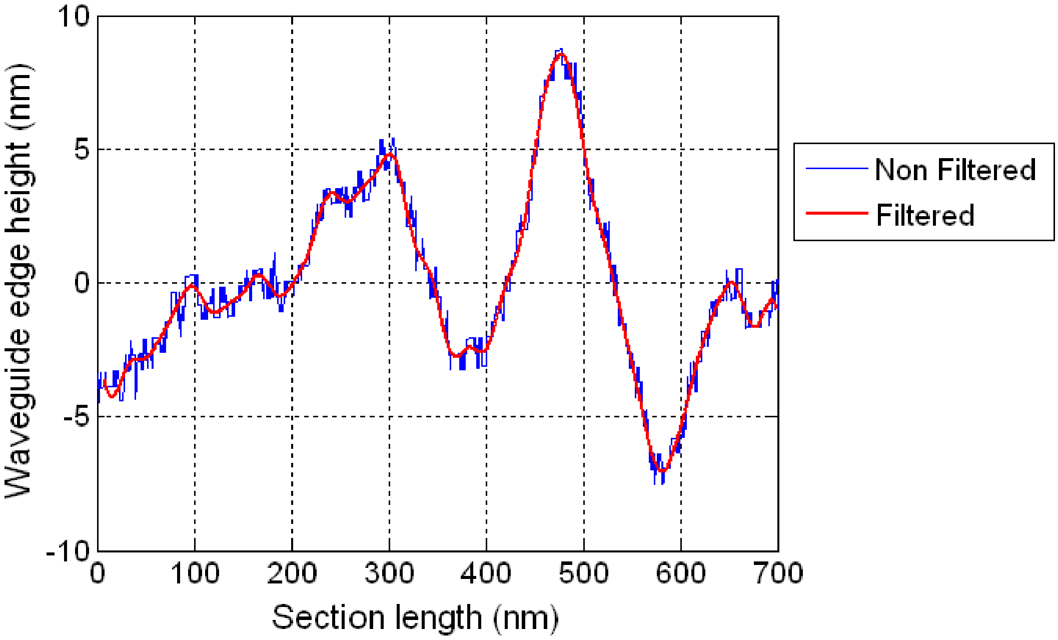

Figure 3.16: Edge profile before and after filtering.

3.3.3 Results

For the first run of tests the iteration time for the chemical iteration was set at $3\,min$ in an attempt to attain minimum roughness. The results for the first run of tests are shown in Figure 3.17. The sidewall roughness is reduced for the first few iterations with a minimum after three oxidation iterations, followed by an increase after four. On this occasion the increase in roughness after four iterations extends to higher than the as-fabricated case. The loss results appear to match well with the roughness measurements with a minimum after three iterations and a subsequent increase to significantly above the as-fabricated case.

The theory proposed initially for the increase in loss after a minimum is that the roughness was limited to some minimum after which the surface condition is actually deteriorated by a further treatment. With this in mind another experiment was conceived with shorter iteration time and more iterations in order to better illustrate the oxidation process. In this experiment the iteration time was reduced

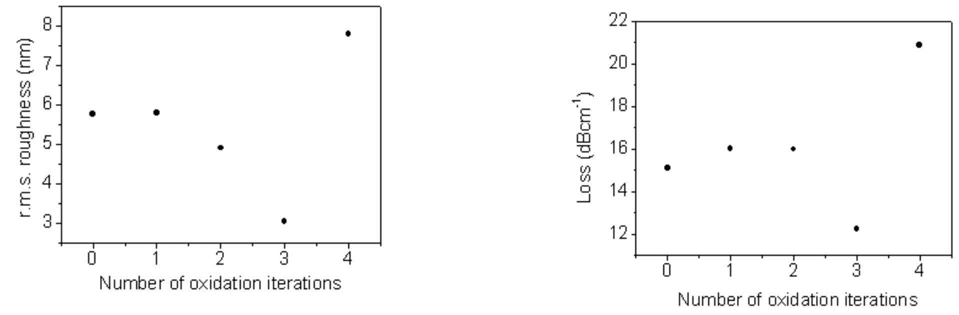

(a) (b)

Figure 3.17: Results of $n \times 3\,min$ oxidation smoothing iterations for 70:20:70 material (a) r.m.s. sidewall roughness (b) waveguide propagation losses.

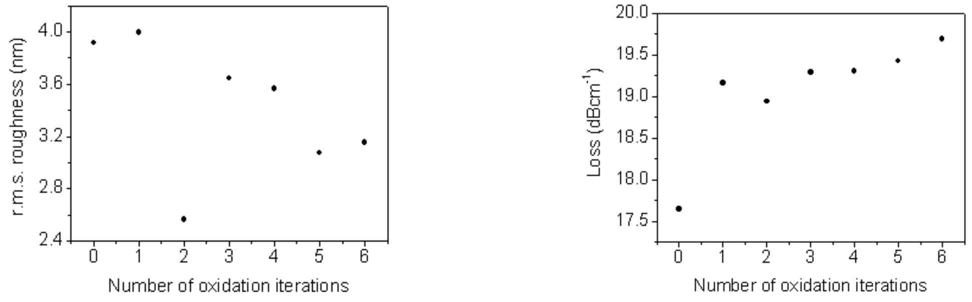

(a) (b)

Figure 3.18: Results of $n \times 1.5\,min$ oxidation smoothing iterations for 70:20:70 material (a) r.m.s. sidewall roughness (b) waveguide propagation losses.

to 1.5min and up to six iterations were processed. Also it was realised that after fabrication the waveguides may have a native oxide covering the sidewalls and if the first oxidation iteration were to have any effect this must be removed prior to that process. To ensure that the sidewall surfaces were free of native oxide before the oxidation process the sample was subjected to an initial HF acid dip. The results of the second round of oxidation experiments are shown in Figure 3.18. In this set of processes the roughness again reaches a minimum after only a couple of iterations and then increases again. However, in this instance further iterations after the increase show that the roughness is once again reduced, supporting the theory that the minimum roughness is attacked by a subsequent process but may possibly be regained as the chemical potential of the surface fluctuates around an optimal value.

The loss measurements, aside from the large jump from the as-fabricated sample, match the roughness calculations fairly well. However, they do ascend at higher iterations where the roughness results are improving. One possible reason for this is that crystal growth from the waveguide sidewalls was observed for increasing iteration number, so that although the actual sidewall roughness was decreased it was still intermittently prone to the growth of crystal structures that could affect the propagation losses. It is still unclear why the losses in this case are worse than the as-fabricated case or what is the process behind the crystal formation. An SEM image showing the crystal structures formed out of the side of the waveguides is presented in Figure 3.19. One other notable result is that for each set of oxidation experiments a sample was processed with only one oxidation step, which lasted for the total time of the maximum number of iterations of the process. So for a run of experiments with a maximum of 5 iterations of $3\,mins$ a sample was subjected to 1 iteration of 15 minutes in duration. These single long oxidations showed sidewall roughness, and propagation losses comparable to those of the associated as-fabricated samples. This agrees well with the supposition that after a short span of fast chemical limited oxidation the process becomes diffusion limited. Taking both sets of results together, the effects of cummulative oxidation time - obtained as a summation of the number of iterations multiplied by the iteration time - as well as iteration number may be compared between the two. The

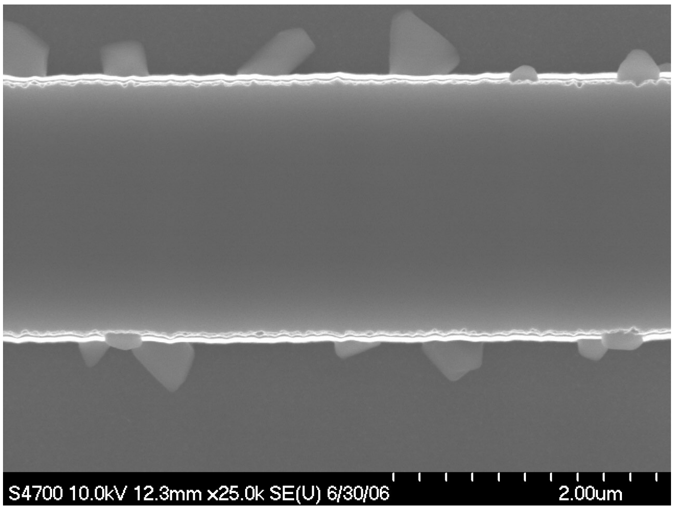

Figure 3.19: Crystal growth from waveguide sidewalls after oxidation smoothing processes.

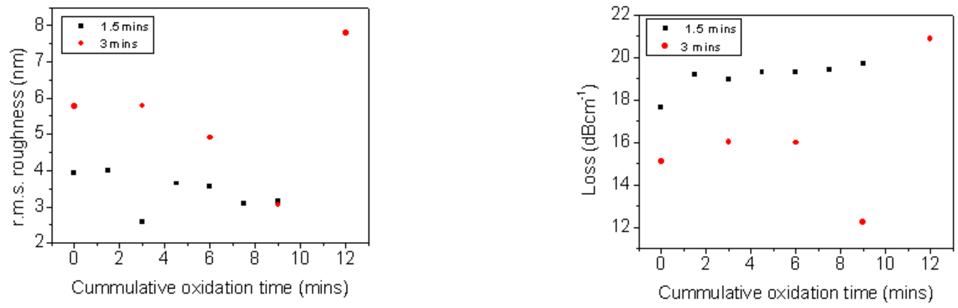

(a) (b)

Figure 3.20: Results of $n\times 3\,min$ and $n\times 1.5\,min$ oxidation smoothing iterations for 70:20:70 material (a) r.m.s. sidewall roughness (b) waveguide propagation losses.

results are shown in Figure 3.20. It seems from the results presented in Figure 3.20 that there is a greater correlation between sidewall roughness (or waveguide loss) and iteration number than between sidewall roughness (or waveguide loss) and reaction time. This suggests that in both cases - for iteration times of $1.5\,min$ and $3\,min$ - the chemical process has reached the diffusion limited case by the end of the reaction time. Therefore the roughness is reduced in the same manner in both sets of results by iteration rather than time.

Also worth noting is that although roughness is lower in the $1.5\,min$ set of results the losses are higher than for the $3\,min$ iterations. This is not entirely disingenuous as both sets of waveguides were fabricated separately and therefore may include effects such as slightly different etch profiles and waveguide angle to the cleaved facet that may affect the loss calculations.

As noted in section 3.2.2 the average losses of as-fabricated waveguides using PMMA/PECVD $Si0_2$ and HSQ based lithography techniques were $16\,dBcm^{-1}$ and $11.6\,dBcm^{-1}$ respectively. For the same set of fabricated guides the average loss of the PMMA/PECVD SiO_2 waveguides was reduced to $12.2\,dBcm^{-1}$ using chemical oxidation techniques, which still does not rival the as-fabricated HSQ guides, which were found to have increased losses after oxidation processing. Therefore, it seems reasonable to favour lithography with HSQ resist with respect to losses, as well as those benefits previously enumerated, where possible. However if the alternative PMMA based techniques are unavoidable then loss reduction via chemical oxidation and subsequent oxide removal may prove useful.

3.3.4 Material absoprtion, free carrier and surface re-combination losses

Many integrated optical devices make use of electrically active and passive structures on the same chip. Clearly there is an issue with material absorption raised in this scenario as the active sections require a bandgap to produce emission or absorption at a specific frequency and the passive regions - necessarily exhibiting the same band-structure when developed on the same material - will show absorption at that same frequency. The main factor in designing integrated systems is to ensure that the active sections have a smaller band-gap than the inactive ones. This ensures that light generated in the device will not have sufficient energy to be absorbed by the material comprising the inactive sections. There are two main methods for fabricating such systems. The first is a process of selective etch and re-growth. A device is created in a single material, the sections required to be non-absorbing are then selectively etched, and another material grown in their place, a technique that may prove to be cumbersome for many applications. The method that will be considered here is that of quantum well intermixing (QWI) [65]. In situations where a device is based on a quantum well (QW) structure, inactive sections may be created by altering the material structure, and hence the band-gap. The process of QWI is one whereby the layer structure of the quantum wells may be disordered such that the band edge of that portion of material undergoes a blue shift. Therefore the light emitted in the active regions does not have enough energy to be absorbed in the intermixed regions. A significant benefit of the intermixing process is that it is a completely post-growth technique making it compatible with current fabrication technology without the problems associated with the alternative etch and regrowth processes.

When considering devices fabricted using QWI methods, further absorption of the light transmitted in the waveguides may be accounted for by free carrier absorption and re-combination due to surface states of the etched material. In semiconductor devices there are a significant number of free carriers created by doping of the lattice: of the order of $10^{17}\,cm^{-3}$. Clearly the operation of active regions relies on the presence of these free carriers. However, in the inactive regions they are purely a source of loss. It is therefore desirable to passivate these carriers in the inactive sections of the device. A number of groups have pursued a method of hydrogen, deuterium or lithium passivation of the free carriers in which the positive ions form neutral complexes at the dopant sites, so tethering the free carriers that would otherwise contribute to the waveguide losses [66–81]. Work was carried out in pursuit of this loss redcution technique but provided mixed results, the bulk of which are presented in Appendix B.

Losses are also suffered in active device regions where the carriers diffuse away from the modal area, reducing the efficiency of the structure. There are a few fabrication techniques used to combat this problem by ensuring the carriers are guided into the area of interest. One option is selective oxidation of a lateral portion of the waveguide ridge so that the carriers are focused through the central portion where the peak intensity of the mode is present, this also has the added benefit of providing an amount of gain guiding of the mode in addition to the refractive index guiding of the structure [82, 83]. The same effect can also be produced by using the mass transport phenomenon. For mass transport a ridge waveguide is fabricated and the core material selectively wet etched so that the ridge is undercut. The sample is then annealed so that the upper cladding is transported down around the exposed core and forms a buried hetero-structure waveguide [84–87].

Surface state recombinations may be addressed by a passivation of the etched waveguide surface. The surface states are a symptom of the dangling bonds which exist at the termination of the lattice and by concluding these surfaces in a dielectric complex the losses may be reduced. Work has been mainly carried out into sulphur passivation of boundaries with interest in hetero-junction bi-polar transistors, with some applications to Vertical Cavity Surface Emitting lasers (VCSELs) [88–96]. The surface passivation may also have applications in devices, particularly deeply etched structures, where the surface roughness increases the density of surface states created. Other methods of passivation including treatment with CF_4 [97], and buried intrinsic layers [98,99] have also been investigated.

3.4 Conclusions

In this chapter the physical structure of the proposed chirped, integrated Bragg grating was presented. It was illustrated that the deeply etched sidewall gratings may provide the high κ values required for chirped grating devices and furthermore by modulating the recess depth of the gratings the coupling coefficient may be controlled. The variation in Bragg wavelength may be provided by modulating the waveguide width, thus varying the propagating modal effective index and so the Bragg condition associated with the fixed period grating. In addition it was noted that by careful design of both waveguide width and recess depth arbitrary functions of Bragg wavelength and coupling coefficient may be defined. Attention was paid to the fabrication of these devices, with emphasis on producing a technique that allowed fully post-growth fabrication using currently available lithography techniques. It was shown that fabrication with electron-beam lithography and reactive ion etching, using HSQ both as an e-beam resist and etch mask could produce well defined structures with better sidewall roughness profile characteristics than the PMMA/PECVD silica alternative. Finally the losses associated with the devices were assessed. It was exhibited that the losses due to sidewall roughness may be reduced using a process of chemical oxidation and oxide removal, although the HSQ fabricated devices showed better as-fabricated results than the oxidation treated PMMA/PECVD silica guides. The losses associated with active waveguide devices were also enummerated and possible loss reduction methods presented.

Chapter 4

Passive, Chirped, Apodised Bragg Grating Devices

4.1 Measurement and analysis techniques

It was mentioned previously that by using an endfire type apparatus for testing passive waveguide structures the transmission spectra of the devices under test (DUT) are the most easily accessed. Therefore the main bulk of measurements carried out on the passive grating devices were done in this manner, the results of which are easily compared to the theoretical analysis already undertaken. The main test rig set-up is shown in Figure 4.1. In this experimental rig a tunable laser is coupled through a polariser, mechanical chopper and microscope objective lens into the test bar. All of the devices considered in this section were fabricated as sections in long, straight waveguides as shown in Figure 4.1. This has the benefit of allowing easy coupling in and out of the devices, and by fabricating simple waveguides on the same samples the properties of these access guides may be obtained, and used in the analysis of the DUT. The polariser was used to select TE injection for the devices, since it is normally TE modes that are more easily generated in semiconductor laser diodes, and therefore the devices under test were designed for operation in this regime. The light from the device bar is then coupled through a microscope objective and iris arrangement to a germanium photodiode that is connected to the lock-in amplifier that controls the mechanical chopper. Finally a personal computer running LabView software is used to control the system and collect the data. One particularly important result of this arrangement is the effect

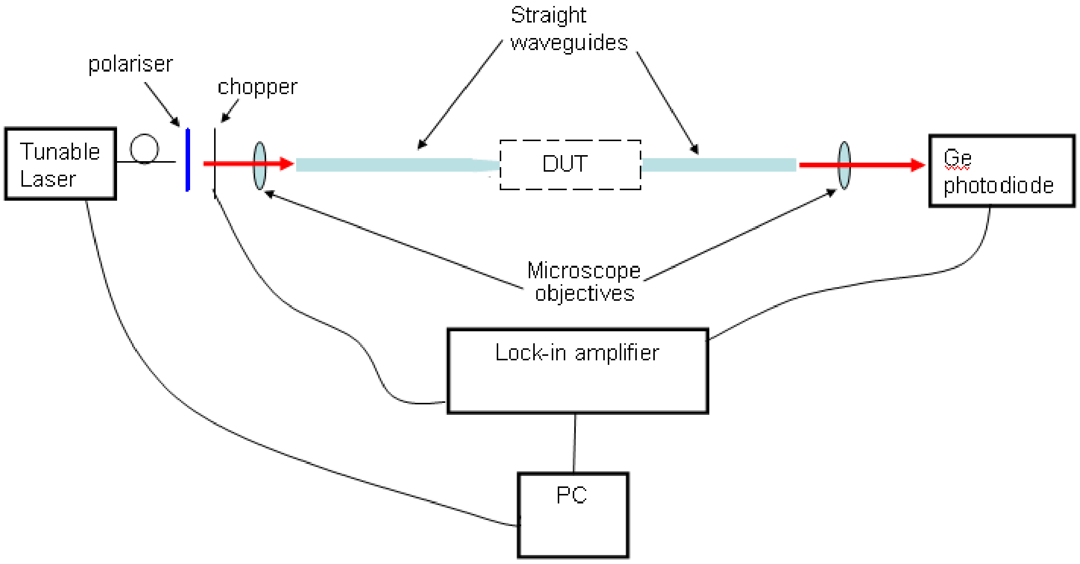

Figure 4.1: Waveguide transmission measurement rig.

on the transmission spectrum due to the facet reflectivity of the device bar. In essence the device is placed in the centre of a Fabry-Pérot cavity that in itself has a characteristic transmission spectrum, which for a simple waveguide, is relient on the facet reflectivity, waveguide loss and total propagation length. Therefore, coupling this response with that of the DUT leads to a measured spectrum which is a complex product of the two. There are of course ways in which these two responses may be decoupled, or at least the effects of the FP cavity minimised. The simplest course is to apply anti-reflection (AR) coatings to the facets in order to minimise the effects of the FP cavity on the transmission spectrum. Failing this, or in cases where even a small facet reflectivity makes the extraction of device parameters difficult, it is possible to numerically extract the device characteristics from the total response, given that a good deal is already known about the system. Much work was done in this direction by Marco Gnan [100], who showed that it was possible to consider the full system as a matrix representation with the DUT characterised by a black-box element with unknown, complex, reflectivities and transmission. A block diagram of this model is shown in Figure 4.2. Where r_{f1}, r_{f2}, t_{f1} and t_{f2} are the facet reflectivites and transmittivities, L_1, L_2 and α_1, α_2 are the access waveguide lengths and losses respectively, t_{bb} is the black-box transmittivity and r_{bb-p} and r_{bb-n} are the directionally dependent black-box reflectivities. The first set of

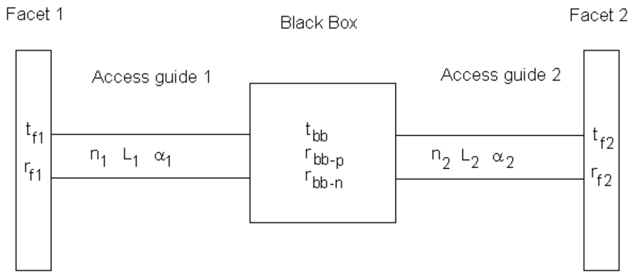

Figure 4.2: Black-box representation of device within a Fabry-Pérot cavity.

parameters that may be obtained are those pertaining to the facets. It is assumed that the facets are identical - if the access waveguides terminating at these surfaces are geometrically similar - and so the reflectivity and transmittivity are easily obtained by recourse to mode solver packages. In turn the waveguide losses may be extracted from the transmission spectra of simple waveguides fabricated on the sample alongside the devices using the Fabry-Pérot fringe measurement method outlined in section 3.3.2, and given the facet reflectivities. By careful fabrication the access waveguide lengths may be directly measured by inspection of the final test bar leaving only the black-box parameters unknown. As stated previously the system may be described as a TMM model, with the section comprising of the DUT being characterised by the unknown reflectivities and trasmittivity, and since the other system parameters may be extracted as described the system is now only a function of these unknowns. Therefore, given the usual matrix elements for simple transmission waveguides and reflectors the complex transmission coefficient of the entire system may be written as (4.1).

$$t_{sys} = \frac{-e^{-jk(n_1L_1+n_2L_2)}e^{-(\alpha_1L_1+\alpha_2L_2)}t_1t_2t_{bb}}{\begin{aligned}1+e^{-2d_1(jkn_1+\alpha_1)}r_1r_{bb-n}+e^{-2L_2(jkn_2+\alpha_2)}r_2r_{bb-p}\\ +\,e^{-j2k(n_1d_1+n_2d_2)}e^{-2(\alpha_1d_1+\alpha_2d_2)}r_1r_2\left(r_{bb-p}r_{bb-n}-t_{bb}^2\right)\end{aligned}} \tag{4.1}$$

Where for $x = 1,2$; n_x is the modal effective refractive index of the access waveguide, L_x is the waveguide length, α_x is the waveguide losses, t_{fx}, r_{fx} are the facet transmission and reflection coefficients respectively and t_{bb}, r_{bb-p}, r_{bb-n} are the transmission and positive and negative direction reflection coefficients respectively. The transmission of the system as measured in the manner described above is related to the transmission coefficient as $T = |t_{sys}|^2$. So, once the transmission spectrum of the device is obtained and the accessible parameters of the total system extracted, the transmission and reflection coefficients of the DUT may be extracted using a curve-fitting method of the transmission spectrum to the TMM representation outlined above, with the parameters of interest remaining free. In this work the curve-fitting was carried out using the least squares curve-fitting method in Matlab. In this routine the least squares distance between the measured transmission and TMM model is minimised in an iterative manner from some initial guess taken as an input. Thus, finally, the DUT transmission and reflection coefficients may be defined free of the effects of the enclosing system.

4.2 Coupling coefficient measurements

It has already been shown that the gratings designed in this work are required to exhibit relatively high coupling coefficients in the the order of tens cm^{-1}. By deeply etching the sidewall gratings it was predicted that large values of κ may be approached, and that the grating recess depth may be used as a manner to control the magnitude of κ. In order to show this a number of single period, unchirped gratings were fabricated with varying grating recess depth over the device set. The devices were fabricated on an $\mathrm{Al}_x\mathrm{Ga}_{1-x}\mathrm{As}$ wafer, the upper and lower cladding layers with a 75% aluminium content and the core 25%. The material structure is given in Figure 4.3. The first gratings to be fabricated were based on a rectangular recess profile. However, these were found to be extremely lossy, with over $10\,\mu m$

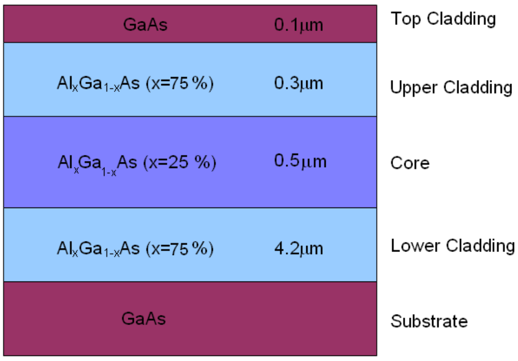

Figure 4.3: Material structure of the $\mathrm{Al}_x\mathrm{Ga}_{1-x}\mathrm{As}$ 75:25:75 wafer.

of grating length proving enough to lose the propagating mode, even outside of the grating stopband region. The gratings fabricated with this geometry exhibited significant sidewall roughness and a swelling of the grating teeth towards their tips due to imperfect etching of the pattern, as shown in Figure 4.4. One possible method of combating the scattering losses and the possible leaky coupling at rectangular grating interfaces is to design a less severe grating profile tapered towards its tip. A triangular grating profile was adopted to reduce the violent modulation of the refractive index observed by the mode, but still retain the overall index perturbation designed for the rectangular grating case. As outlined earlier it was found that fabrication of the grating structures gave better results using the HSQ resist, instead of the PMMA/PECVD silica mask technique. A schematic of the grating profile is shown in Figure 4.5. Additionally as the mode profile is assumed to be slowly varying the modulation of effective index over the grating period should still produce the high coupling coefficient, but the smooth transition between high and low index that the mode travelling through the grating teeth sees should reduce the effective loss. The gratings were fabricated in the same way as illucidated in section 3.2. The results of the fabrication are shown in Figure 4.6,

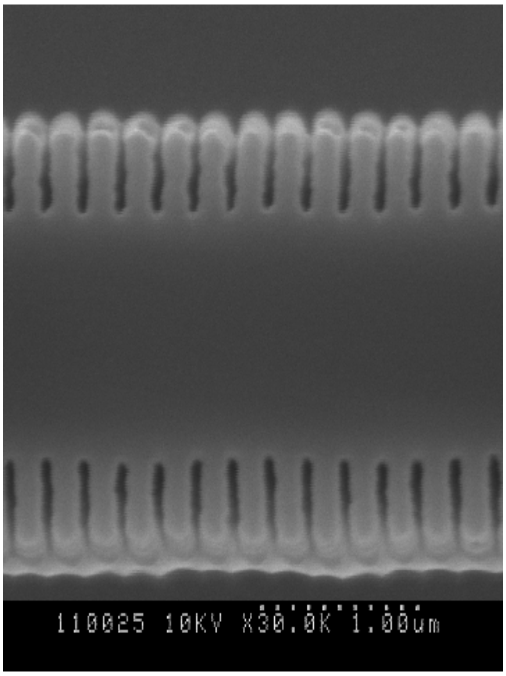

Figure 4.4: Gratings with rectangular recess profile, fabricated using PMMA based lithography.

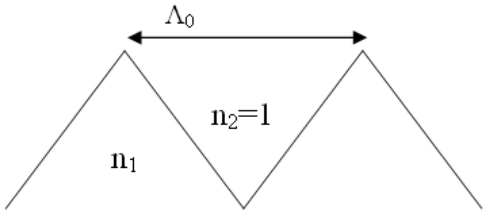

Figure 4.5: Triangular grating profile.

with examples of tapered, rectangular and varying recess depth gratings. Again it is clear that the sidewall verticality is very good, with much of the roughness evident in the fabrication with PMMA/PECVD silica now reduced.

In addition to extracting the relationship between grating recess depth and coupling coefficient for the fabricated devices an assesment of the anti-reflection coatings, a quarter-wavelength layer of Zirconium oxide deposited using an electron-beam evaporation tool, and curve-matching technique were undertaken. Firstly, using the same method by which roughness was calculated on waveguide edges - namely by analysis of SEM images - the grating recess depth was measured. From the images in Figure 4.6 it is clear that while the sidewall verticality looks very good and the grating teeth are very well defined there is a RIE lag effect between the grating teeth, in other words the grating shows less faithful representation of the mask the further from the top of the waveguide it is observed. Subsequently, the transmission spectra of the grating devices were measured for device bars with no coatings, one and two facet coatings. From each of these sets of results, using the known parameters of the test device bars, the transmission coefficient of the grating was recovered by means of the curve-fitting method described. Figure 4.7 shows samples of measured spectra for devices with no facet coatings, one and both facets coated, together with the recovered transmission spectra for these devices, with a comparison of the three recovered spectra in Figure 4.8. The recovered spectra show good isolation from the FP and multiple cavity effects with the bulk of the visible fringes isolated from the transmission spectrum of the DUT. From Figure 4.8 it is clear that there is good matching between the stopbands of all of the recovered spectra, considering both the main feature dimensions and the first

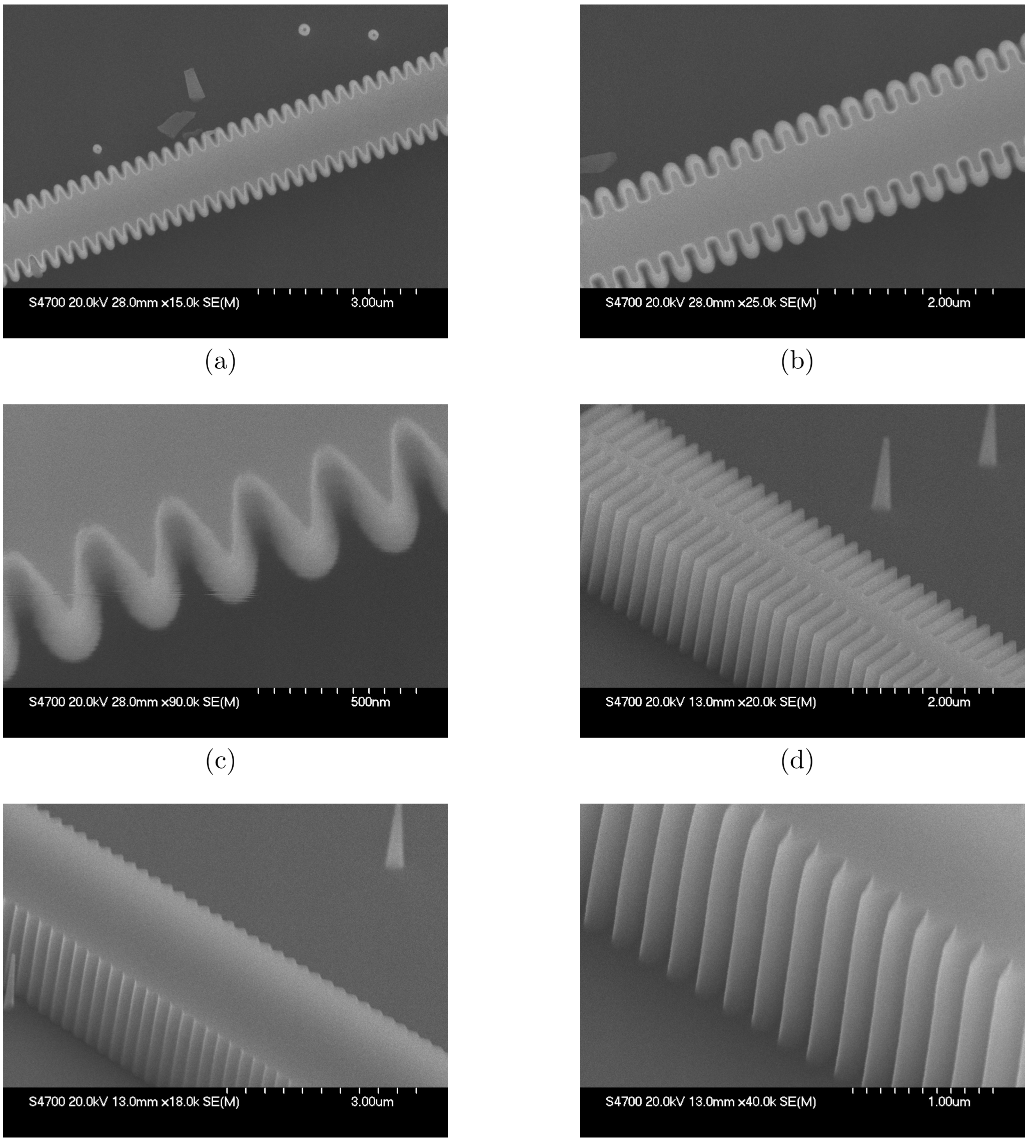

(a) (b)

(c) (d)

(e) (f)

Figure 4.6: SEM images of fabricated deeply etched gratings.

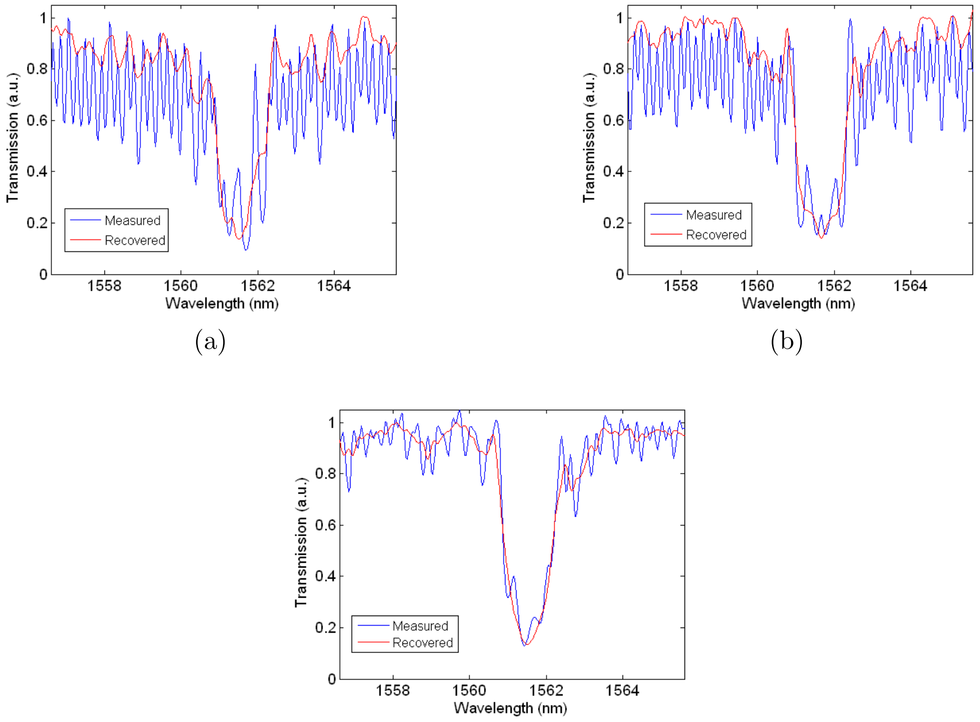

(a)

(b)

(c)

Figure 4.7: Measured and recovered transmission spectra for devices with (a) no facet coatings, (b) 1 facet coated, (c) 2 facets coated.

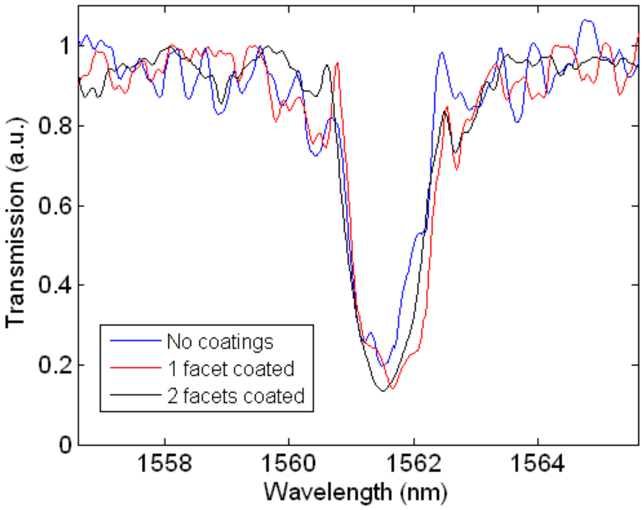

Figure 4.8: Recovered spectra for grating devices with various facet conditions.

sidelobes. It may also be noted that the stopbands very closely match although the devices are on different test bars, giving good confidence in the consistency of the fabrication process.

Further to the transmission spectrum recovery, the assumption may be made that the DUT is a Bragg grating device, of which the analytical transmission coefficient may be written easily in terms of the coupling coefficient by way of the solution to the coupled-mode equations. Then by curve-fitting the recovered transmission spectrum - in the same way as the DUT characteristics were gained - to the Bragg function, the value for κ may be recovered. Figure 4.9 shows the fitted Bragg grating solution to the recovered transmission spectrum of a device with facet coatings. Clearly, the recovered spectrum matches very well with that predicted by solution of the coupled-mode equations and hence confidence may be expressed in the recovered value of κ, which in the case illustrated is $35.7\,cm^{-1}$.

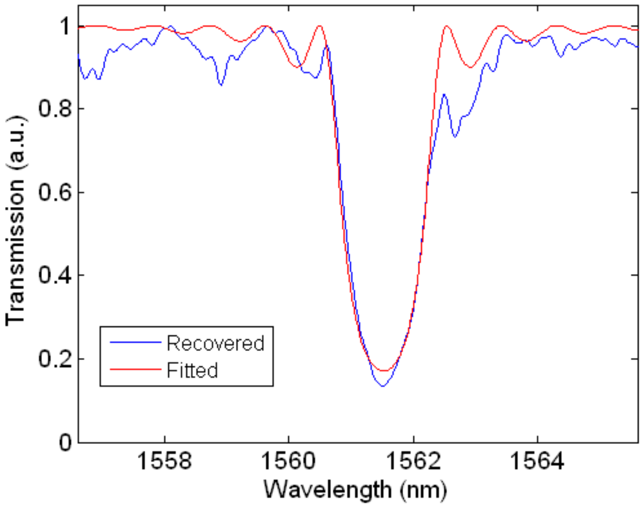

Figure 4.9: Fit of Bragg grating device to recovered transmission spectrum.

The devices with varying recess depth and with a variety of facet conditions were measured and the transmission spectra recovered and fitted to Bragg grating conditions producing both the effective index, from the central wavelength of the stopband, and coupling coefficient of the grating. The full set of results are given in Figure 4.10. Encouragingly, the results from all three facet conditions, for both κ and n_{eff}, match very well giving confidence in the transmission spectrum recovery

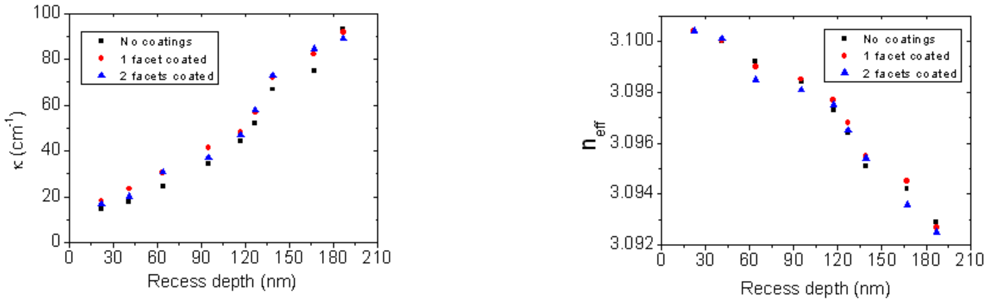

(a)

(b)

Figure 4.10: Recovered values for (a) coupling coefficient and (b) effective index of the single period grating structures.

method. As expected, the deeply etched sidewall gratings produce high coupling coefficient values, increasing with recess depth. These values are somewhat smaller than may have been predicted though the disparity may be easily explained as a manefestation of the RIE lag effect and fabrication imperfections. Figure 4.10a implies a non-zero intercept of coupling coefficient with grating recess depth. Ideally, for no grating modulation there should be no energy coupled into the backward propagating mode. However, it is possible for energy to be backscattered by the sidewall roughness of the waveguide, giving rise to the predicted coupling. Another important point to highlight is that with increasing recess depth the effective index of the mode travelling in the grating is reduced, an intuitive result considering the reduced average cross-section of waveguide carrying the mode due to the grating recesses. However, this result is important when considering grating design, especially as in this work the grating effective index profile, by way of the waveguide width, is used to control the grating phase characteristics. Therefore, when it comes to designing chirped gratings with variable coupling coefficient profiles, the recess depth will play a part in both the coupling coefficient and the chirp, and so both the waveguide width and recess depth must be designed carefully to give the required response.

4.3 Characterisation of gratings with arbitrary chirp and κ profiles

It has been shown that the deeply etched gratings provide the high coupling coefficients required for chirped grating applications, as well as a flexibility in κ design that will allow variation of the coupling coefficient along the grating length simultaneously with the variation of the Bragg condition. With these two parameters controllable using a combination of the grating waveguide width and recess depth it is possible to design gratings with arbitrary chirp and κ characteristics. Figure 4.11 shows a schematic of the grating design, with variable recess depth, d, and waveguide width, W, that in conjunction allow design of arbitrarily varying functions of grating amplitude and phase response. However, although W and d may be independently modulated their effects are necessarily linked through the modal effective index. So that to create a grating with a constant Bragg condition along its length with apodisation of the coupling coefficient for example, requires modulation of both d and W, since variation of the former alone although giving an apodisation profile also results in unwanted chirping of the grating response by way of the modal effective index. Therefore, in order to design gratings with accurate transcriptions of the desired functions of λ_B and κ the effects of varying W and d must be well known. By recourse to a mode solver package, FIMMWAVE was used for this work, the variation of modal effective index with waveguide width may be modelled. As shown in the previous section the effect of varying recess depth on gratings with constant width may be determined experimentally, yielding both the

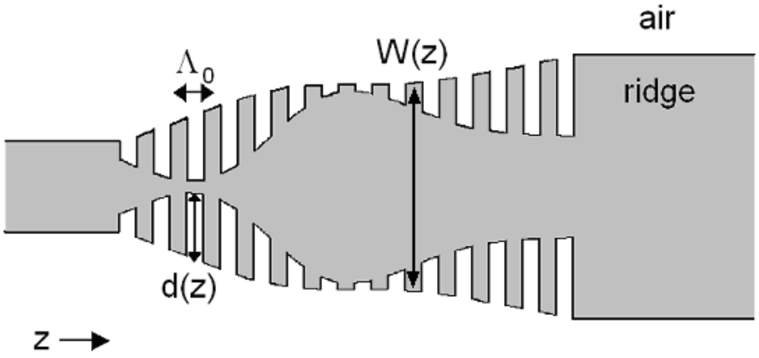

Figure 4.11: Schematic of deeply etched tapered Bragg grating with independently variable recess depth and waveguide width.

functions of n_{eff} and κ with respect to recess depth and waveguide width. With these functions known then, mappings may be formulated of both effective index and coupling coefficient as functions of waveguide width and grating recess depth. Finally, given a desired combination of n_{eff} and κ, a solution may be found for W and d that produces these values. In order to demonstrate the control that may be excercised over the grating parameters a set of devices were fabricated to include the variations in response given in Table 4.1. The chirp profiles were designed for single Bragg wavelength, linear chirp and non-linear chirp profiles, where the non-linear chirp function used in this work was a summation of linear and Gaussian functions of the propagation length as shown in Figure 4.12. The κ profiles were designed to produce, constant κ with propagation length, an apodised coupling coefficient profile obtained by applying a Gaussian envelope to the κ function, and the non-linear variation as given in Figure 4.12. The varying functions of n_{eff} and κ were translated into functions of waveguide width and grating recess to produce the required grating characteristics, and these functions directly transcribed into the E-beam lithography mask design. Finally, the geometries designated with coded κ profiles in Table 4.1 were devices with constant Bragg conditions along their lengths, but where variation of the coupling coefficient allowed modulation of the stopband characteristics. These devices are useful for pulse shaping applications where, for example, a single input pulse may be modulated in reflection into a pulse code train. Four variations of these coded κ profiles are shown in Figure 4.13.

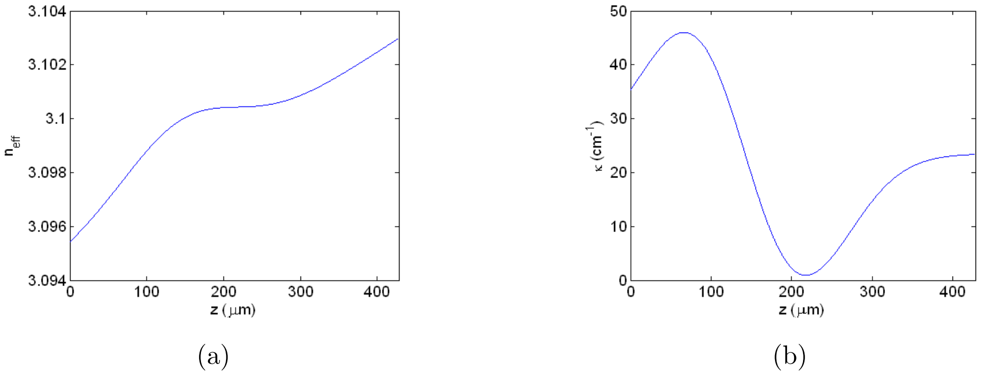

(a) (b)

Figure 4.12: Designed non-linear chirped Bragg grating (a) effective index profile and (b) κ profile.

Although it has been shown that even without anti-reflection coatings the trans-

Table 4.1: Chirped, varying κ grating designs.

Chirp profile	κ profile
None	Constant
None	Gaussian
Linear	Constant
Linear	Gaussian
Non-linear	$f\left(\frac{dn_{eff}}{dz}\right)$
None	Coded

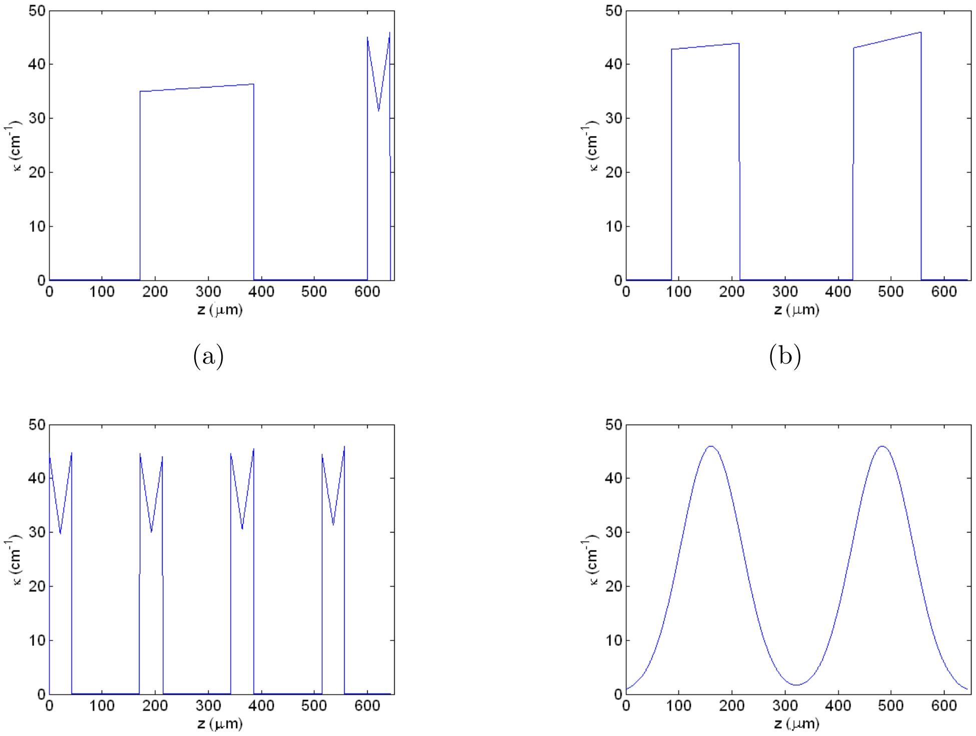

(a)

(b)

(c)

(d)

Figure 4.13: Designed coded κ profiles (a) C1, (b) C2, (c) C3, (d) C4.

mission spectra of grating devices may be accurately recovered from the measured characteristics by way of the TMM based retrieval algorithm, it is obviously desirable to minimise the effects of the facet reflectivities if possible, therefore all of the measured devices were fabricated with anti-reflection coatings on both facets of the test bars. Figure 4.14 shows the simulated transmission spectra of the single wavelength and chirped devices as designed along with the recovered spectra. The simulated spectra were obtained using the TMM model described in section 2.5, where for all of the grating variations L_g was $450\,\mu m$ - except for the coded devices where $L_g = 625\,\mu m$ - and the peak value of κ was set at $70\,cm^{-1}$. These parameters were set to match the values aimed at in the fabrication of the devices.

There is evidently good agreement between the simulated and recovered transmission spectra, with a few interesting points to note. Firstly, the effect of apodisation of κ on both the constant n_{eff} grating and the linearly tapered grating is to reduce the apparent sidelobes in the grating response, this has clearly taken effect in the measured results (Figure 4.14b and Figure 4.14d.) Next, gratings with both linear and non-linear chirp follow the simulated results closely, exhibiting not only the utility of the waveguide taper method but also the κ dependence on recess depth and waveguide width has been effectively modelled and designed into the structures. This result is important as it exhibits that with control of these two parameters, arbitrary grating Bragg wavelength and coupling coefficient profiles may be created as hoped, and also the two effects may be induced independently from one another. Finally, as it is only the transmission spectrum that is measured here there is the possiblity of a number of solutions to the $\lambda_B(z)$, $\kappa(z)$ coupling that may produce the detected spectrum. In this case a secondary method to measure the phase profile of the grating - and hence decouple the two parameters - is needed, which will be discussed presently. However, for the single wavelength gratings this problem does not arise and the value for κ may be extracted directly from the transmission response.

The transmission and simulated spectra of the coded gratings are shown in Figure 4.15. Again it is clear that there is excellent agreement between the simulation results and the recovered transmission spectra for the coded grating devices. Although these devices are designed around a single Bragg condition, the variation of coupling coefficient along their length allows for pulse shaping in the tempo-

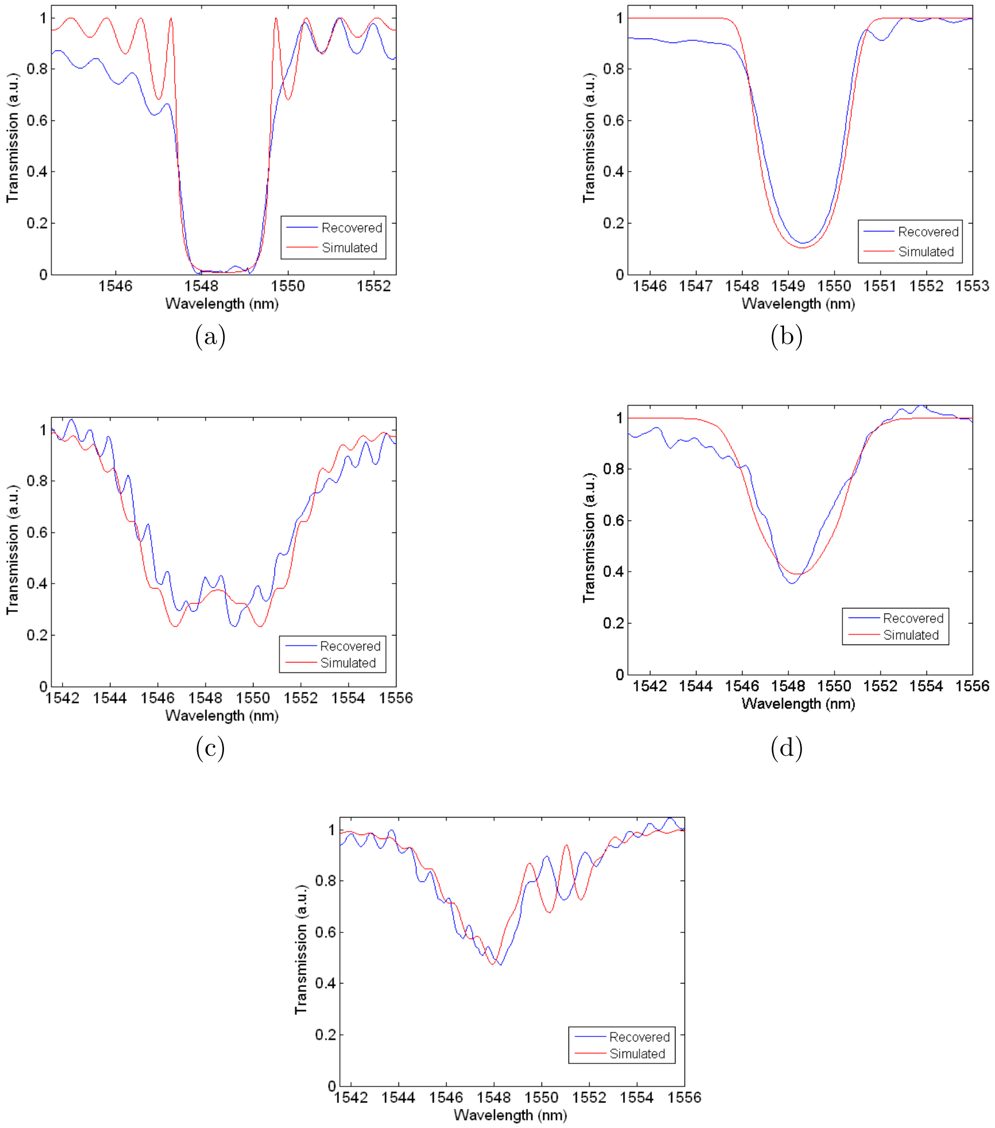

(a) (b) (c) (d) (e)

Figure 4.14: Simulated and recovered transmission spectra for gratings with (a) constant n_{eff} and κ, (b) constant n_{eff} and apodised κ, (c) linearly chirped n_{eff} and constant κ, (d) linearly chirped n_{eff} and apodised κ, (e) non-linearly chirped n_{eff} and κ

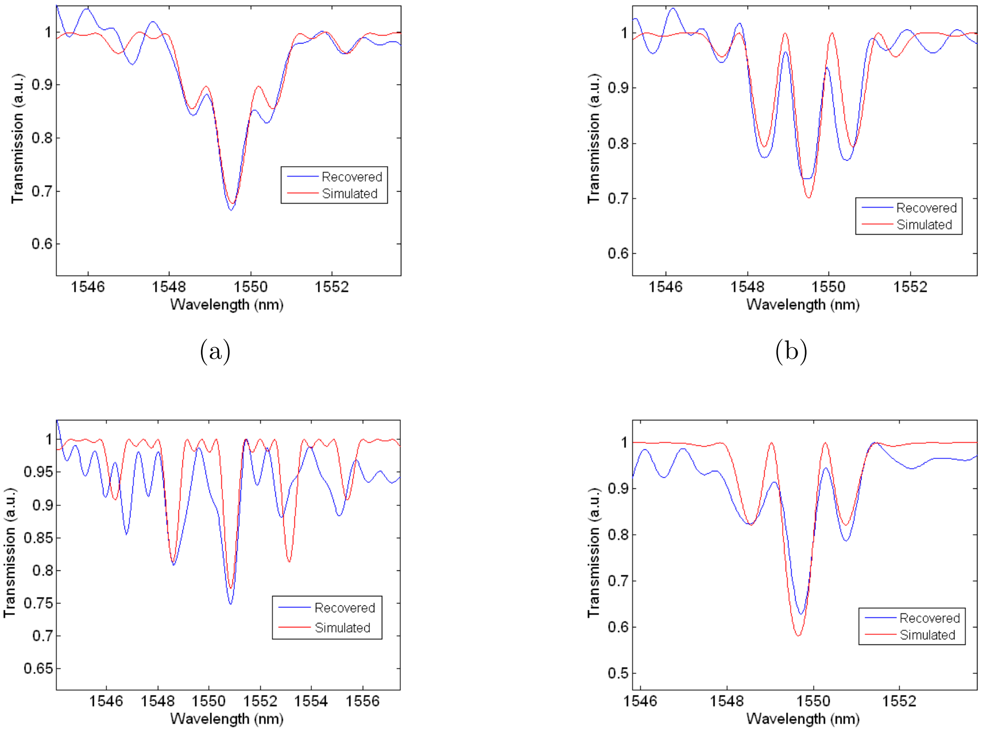

(a)

(b)

(c)

(d)

Figure 4.15: Simulated and recovered transmission spectra for gratings with (a) constant n_{eff} and C1 κ, (b) constant n_{eff} and C2 κ, (c) constant n_{eff} and C3 κ, (d) constant n_{eff} and C4 κ.

ral domain, and stopband modulation in the spectral domain. In the examples given here stopbands with multiple narrow band reflection peaks and broadened bandwidths are exhibited showing again the control possible over the grating characteristics by modulation of κ.

4.4 Grating phase measurements

It was stated that where transmission measurements of grating devices are taken there is always a possibility - although probably small - that the characteristic may be liable to a number of solutions in terms of κ and λ_B functions of the grating. This being the case it is desirable to perform a measurement that is strongly dependent on its phase characteristics. Then together with the transmission measurements, confidence in the actual grating phase profile may be gained. To this end a measurement based on a Michelson interferometer setup was devised. To include the devices in an external Michelson interferometer would be difficult, as not only is it necessary to couple light into the bar but also exact balancing of the interferometer arms' optical path lengths is required to extract the interference fringes accurately. Therefore rather than constructing an experimental rig around the devices, an integrated Michelson interferometric device was designed. A schematic of the integrated Michelson interferometer is shown in Figure 4.16. There are a number of important features of the integrated Michelson interferometer device to note. The input and output waveguides are the usual deeply etched straight wavegudies - in fact the entire device is deeply etched requiring therefore only one lithographic step - that have been used to couple into the device bars previously explained, and as before the facets are treated with AR coatings to avoid the effects of unwanted reflections. In order to couple light into the two interferometer arms, and the resulting interference field out, a $3\,dB$ multimode

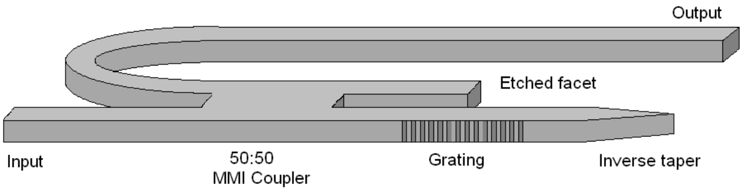

Figure 4.16: Schematic of integrated Michelson interferometer.

interference coupler is employed [101]. To gain the 50:50 power splitting ratio the MMI length is taken as $\frac{3}{2}\times$ the beat length of the device; the beat length may be written as (4.2).

$$L_\pi = \frac{4n_{ridge}}{3\lambda_0}.\left(W_{MMI} + \frac{\lambda_0}{\pi}\left(\frac{n_{clad}}{n_{ridge}}\right)^{2\sigma}\sqrt{n_{ridge}^2 - n_{clad}^2}\right) \tag{4.2}$$

Where L_π is the MMI beat length, n_{ridge} is the effective index of the ridge structure, n_{clad} is the effective index of the cladding, λ_0 is the propagating wavelength, W_{MMI} is the physical width of the MMI coupler and σ is 0 or 1 for TE or TM modes respectively. For the material structure under consideration, a MMI width of $6\,\mu m$ and a TE mode, the length of MMI defined for a double image at the output is $152\,\mu m$. To verify the operation of the device before fabrication the structure was simulated using RSoft's BEAMPROP beam-propagation software. The resulting contour-map of intensity on the $2D$ plan of the MMI device is shown in Figure 4.17. Clearly the MMI is predicted to give the required 50:50 power splitting.

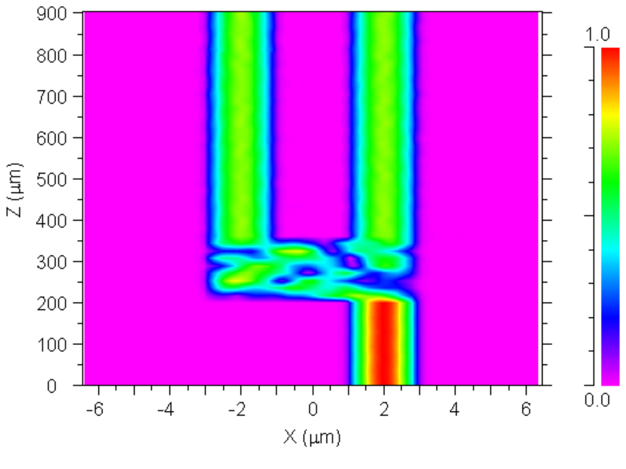

Figure 4.17: BPM simulation of MMI device.

In the first arm of the interferometer the waveguide is terminated in an etched facet to give broadband reflectivity of a well defined path length. The position of the reflector is set to correspond to a distance halfway along the grating device in the second arm. In this manner the phase accumulation in both grating arms is easily simulated, the etched facet simply as the optical path length of the propagating mode and the grating as the reflected wave calculated using the TMM model previously described. In addition, at the termination of the grating an inverse taper [102] was fabricated so that the transmitted mode would be dissipated into radiation without back-reflection into the Michelson device. Also of interest is the application of the AR coatings. For if care is not taken in the deposition of the coatings then the etched facet may also be affected and so reduce its effectiveness as a broadband reflector. In order to address this issue the device bars were slightly tilted on the rig in such a way that the evaporation process would not affect the etched facet. This arrangement is shown in Figure 4.18, where for an etched facet of $2\,\mu m$ in height, $50\,\mu m$ from the cleaved facet, $\theta > 2.3^o$.

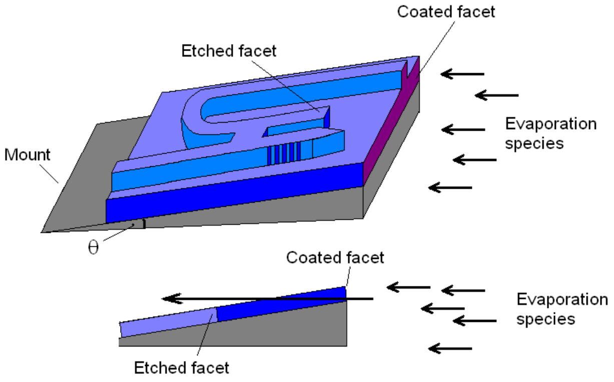

Figure 4.18: E-beam evaporation rig to avoid coating of etched facet in integrated Michelson device.

The devices were measured using the same endfire rig setup as employed for the transmission spectra measurements, with the results in this case being the interference fringes from the integrated Michelson device. The measured results were compared with the simulated spectra, obtained from the TMM model of the chirped Bragg gratings. The devices measured in the Michelson setup were the three chirped grating geometries previously studied, namely the linearly chirped gratings with constant and Gaussian apodisation profiles of κ respectively and the non-linearly chirped grating with non-linearly varying κ. Again the grating lengths were set at $450\,\mu m$ with a peak coupling coefficient of $70\,cm^{-1}$. The results of the Michelson interferometer measurements are shown in Figure 4.19. From all

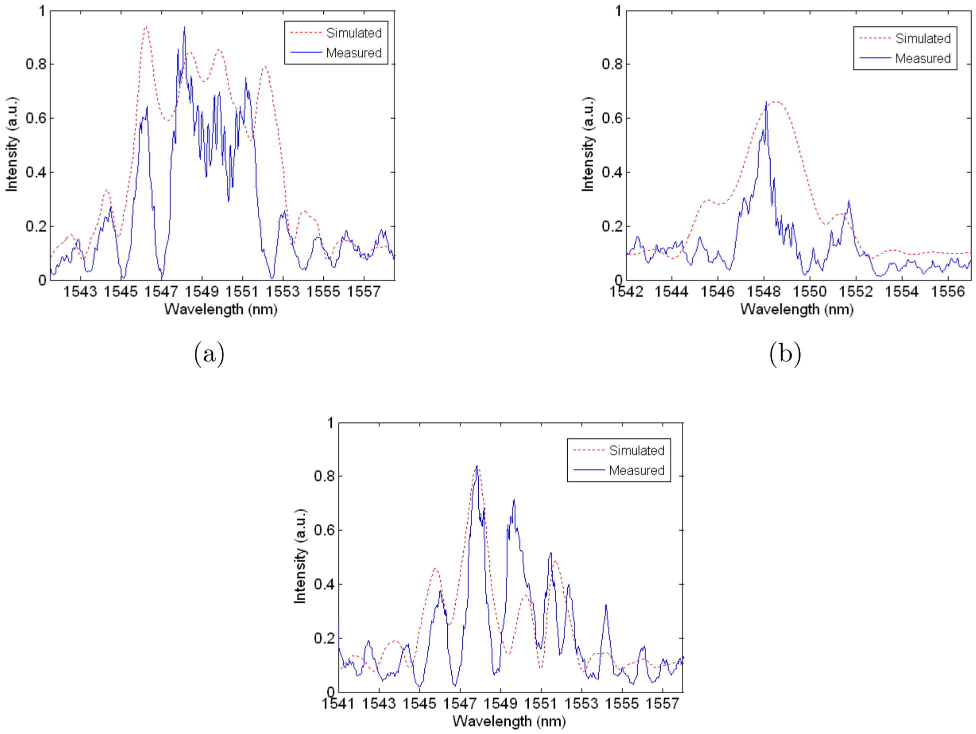

(a)

(b)

(c)

Figure 4.19: Simulated and measured Michelson interferometer transmission spectra for gratings with (a) linearly chirped n_{eff} and constant κ, (b) linearly chirped n_{eff} and Gaussian apodisation of κ, (c) non-linearly chirped n_{eff} and non-linearly varying κ.

three grating variations illustrated in Figure 4.19 it is clear that there is reasonable matching between the simulated prediction of the integrated Michelson interferometer transmission spectra and those measured. The interference may then be used to derive the phase of the reflected field from the grating. The intensity of the interference spectrum from the Michelson interferometer may be given as (4.3).

$$I = |E_1|^2 + |E_2|^2 + |E_1|\,|E_2|\,cos\left(\Delta\phi\right) \tag{4.3}$$

Where I is the intensity of the interference signal, E_1 is the reflected field from the etched facet, E_2 is the reflected field from the grating, and $\Delta\phi$ is the phase difference between them. To find the phase of the field reflected by the grating a number of assumptions must be made. First it is taken that E_1 has a constant amplitude with wavelength related to the facet reflectivity. Secondly the amplitude of E_2 is taken to be that measured in transmission. With these assumptions both the theoretical and reflected phase may be extracted, with the simulated and measured interference signals being taken as inputs respectively. The extracted phase of the chirped gratings is shown in Figure 4.20 where the measured phase matches closely with that simulated. This further confirms the measurements of the device transmission spectra, and once again since these devices were fabricated separately, illustrates the consistency of the fabrication procedure. In addition to confirming the designed grating characteristics the results achieved here also serve to demonstrate the facility of the integrated Michelson interferometer for carrying out these kinds of measurements.

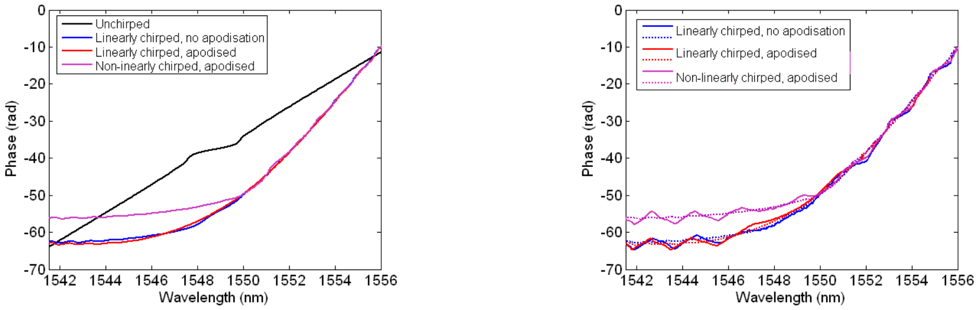

(a) (b)

Figure 4.20: (a) Simulated, reflected phase for various grating designs, (b) simulated (dotted lines) and measured (solid lines) reflected phase for variations of chirped, apodised gratings.

4.5 Conclusions

In this chapter the measurement setup used for both transmission and integrated Michelson interferometric method measurements on passive grating devices was presented. Two methods by which the unwanted Fabry-Pérot fringes associated with the cavity formed by the cleaved facets may be suppressed were outlined. It was suggested that the devices may be treated with facet coatings or that the measured transmission spectrum could be post-processed using a curve-matching technique based on a black-box representation of the DUT within an external cavity. Both methods were carried out and it was shown that the black-box approach successfully minimised the effects of the external cavity on the recovered transmission spectra, that finally matched very well with devices with facet coatings that physically reduced the effects of these fringes. A range of devices were fabricated varying the grating recess depth and waveguide width, effectively mapping the effect of these parameters on the grating coupling coefficient and Bragg condition. It was shown that not only did the deeply etched sidewall gratings provide the predicted means to attain high values of κ but also by careful design of the recess depth and waveguide width arbitrary grating functions of λ_B and κ may be designed. Gratings with a wide range of characteristics were fabricated and their transmission spectra measured. The measurements were shown to follow the TMM model simulations very closely over the array of devices, illustrating that the proposed grating structure can deliver both varying chirp and coupling coefficients together and in isolation. Non-linearly varying grating functions were also exhibited along with coded functions of apodisation, further attesting to the ability of the gratings to provide arbitrary grating profiles. Finally, confirmation of the grating phase characteristics were made using an integrated Michelson interferometer device. The results again closely agreed with simulation further confirming the quality of the grating devices, the consistency of the fabrication processes and also the application of the integrated Michelson device itself. So, the properties hoped for from the proposed grating device were confirmed experimentally, namely, high values of κ, broad Bragg wavelength bandwidth, and arbitrary control of grating chirp and coupling coefficient.

Chapter 5

CBG Distributed Feedback Lasers

In addition to application as passive dispersion control elements or in DBR lasers CBGs may be exploited in the design of distributed feedback laser (DFB) structures. The main purpose of fabricating CBG DFB lasers was initially as a secondary method to confirm the fabricated, chirped grating operation in both amplitude and phase terms. DFB laser devices were also selected as a precursor to fabrication of the more complex DBR and mode-locked lasers as they are generally more easily manufactured and less susceptible to factors such as facet quality and absorption in passive regions.

However, the effects of applying a chirped structure as the basis for a DFB laser are not entirely clear from the analysis of passive grating structures. A derivation of the coupled-mode equations governing chirped DFB structures was outlined in section 2.3, and by including the gain term into the matrix-method simulations the behaviour of a CBG DFB laser may be predicted.

Using the TMM derived previously a number of chirped DFB geometries were simulated. The transmission spectrum of each device in the absence of gain, and the mode plots of the laser were calculated.

5.1 Fabrication of laser devices

The active devices were fabricated on a Multiple Quantum Well structure with InGaAs wells and GaAs barriers with lithography carried out in the same manner as for the passive devices. The MQW laser material details, lasing around 980 nm, are given in Figure 5.1. After the lithography a few further steps must be taken for

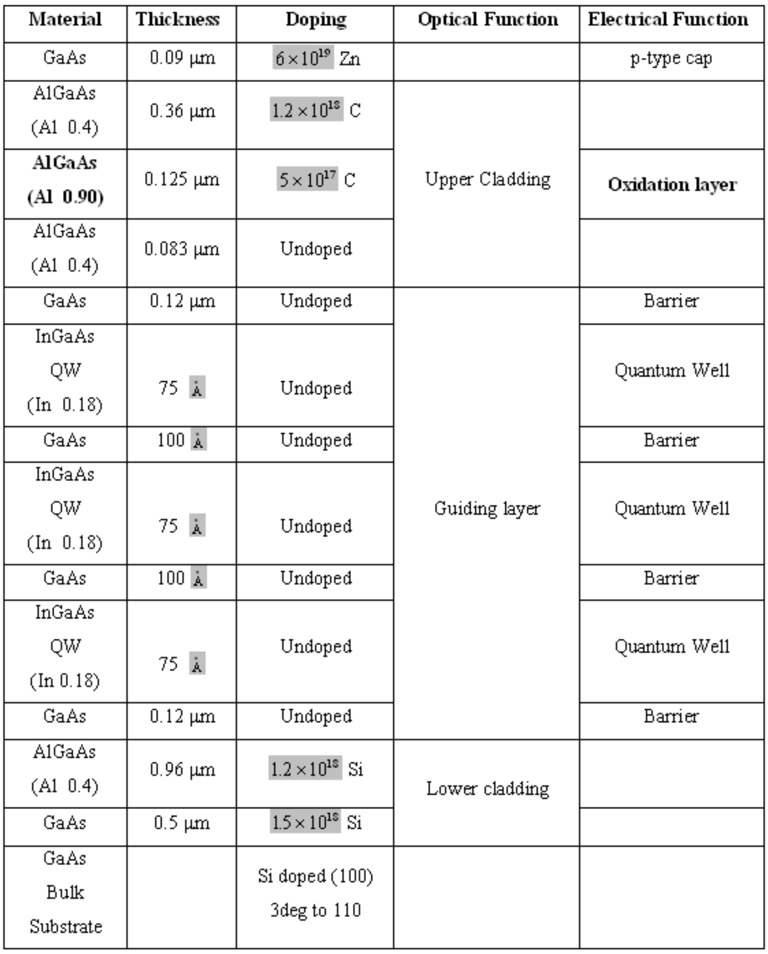

Material	**Thickness**	**Doping**	**Optical Function**	**Electrical Function**
GaAs	0.09 μm	6×10^{19} Zn		p-type cap
AlGaAs (Al 0.4)	0.36 μm	1.2×10^{18} C	Upper Cladding	
AlGaAs (Al 0.90)	0.125 μm	5×10^{17} C		**Oxidation layer**
AlGaAs (Al 0.4)	0.083 μm	Undoped		
GaAs	0.12 μm	Undoped	Guiding layer	Barrier
InGaAs QW (In 0.18)	75 Å	Undoped		Quantum Well
GaAs	100 Å	Undoped		Barrier
InGaAs QW (In 0.18)	75 Å	Undoped		Quantum Well
GaAs	100 Å	Undoped		Barrier
InGaAs QW (In 0.18)	75 Å	Undoped		Quantum Well
GaAs	0.12 μm	Undoped		Barrier
AlGaAs (Al 0.4)	0.96 μm	1.2×10^{18} Si	Lower cladding	
GaAs	0.5 μm	1.5×10^{18} Si		
GaAs Bulk Substrate		Si doped (100) 3deg to 110		

Figure 5.1: MQW material for lasing at 980nm.

fabrication of the laser devices. First the sample is coated with 200 nm of PECVD Si0$_2$, then a thick bi-layer of PMMA E-beam resist is spun onto the top surface. Narrow windows that extend over the gain region of the lasers are patterned in the PMMA and subsequently opened into the silica mask to allow contacts to be deposited. The sample is then cleaned and a second bilayer of PMMA spun onto the top surface. Large contact pad windows are then patterned into the resist. The cap layer of the semiconductor is wet etched and a Ti:Pt:Au contact evaporated onto the waveguide surface. Subsequent to the metal evaporation a further few hundred nanometres of gold is sputtered onto the sample. The sputtering is necessary to ensure the structure's vertical sidewalls and their bases are sufficiently coated to allow current flow to the device. The remaining resist is removed using a liftoff technique that clears the unwanted metal, leaving only the positive contacts. The sample substrate is then thinned down to around $200 - 300\,\mu m$ and a negative contact evaporated onto the substrate side. Finally the bars are cleaved and tested. The p-contact lithography and metalisation process is shown in outline in Figure 5.2.

5.2 Single period DFB laser

5.2.1 Simulation

Before examining the effects of introducing a chirp to the Bragg grating it is worth first noting the response of a simple, constant period, DFB laser. The transmission spectrum of a single period Bragg grating with no gain is shown in Figure 5.3. The device simulated was 500 μm long, with a constant coupling coefficient of $10\,cm^{-1}$. When the gain term is included in the simulation of the Bragg structure the response of a DFB with the same characteristics is effectively modelled. It may be recalled that the electric field in the grating can be written as:

$$\begin{aligned} E(z) = E_f(z)exp\left[g - j\left(\beta_0\left(1 - \frac{n_0 - n_{eff}}{n_0}\right) + \Delta\beta\right)z\right] \\ + E_b(z)exp\left[g + j\left(\beta_0\left(1 - \frac{n_0 - n_{eff}}{n_0}\right) + \Delta\beta\right)z\right] \end{aligned} \tag{5.1}$$

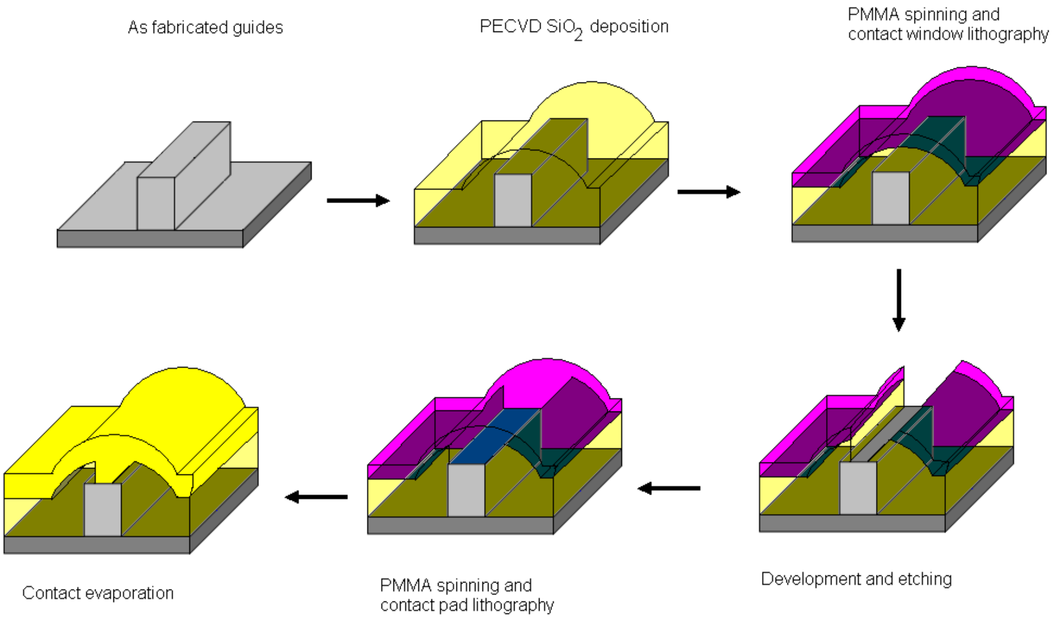

Figure 5.2: Fabrication of laser p-contacts.

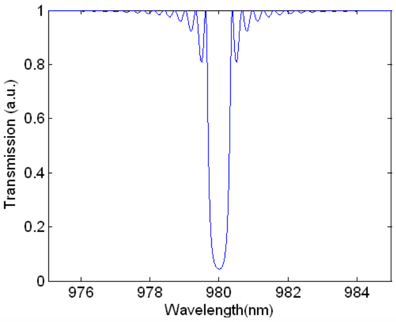

Figure 5.3: Simulated transmission spectrum of a single period Bragg grating with zero gain.

For the case of the passive gratings studied previously the gain, g, was set at $g = 0$. In order to simulate the behaviour of chirped, apodised, DFB lasers this modal gain term was varied from $0 \rightarrow 100\,cm^{-1}$ and the resulting output intensity plotted as a contour function of wavelength and modal gain. The simulated response of a single period DFB is shown in Figure 5.4. The modal spectrum is symmetric about the Bragg wavelength of the device with two fundamental lasing modes either side of the stopband. In real devices the mode competition between the fundamental modes is annihilated by asymmetric fabrication of the waveguides surrounding the DFB structure, forcing lasing action in only one mode.

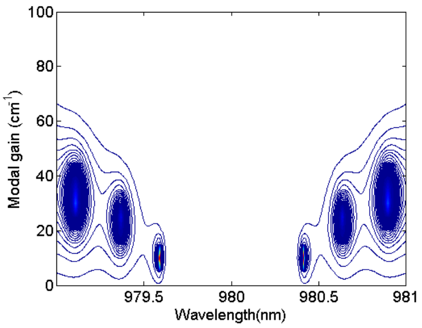

Figure 5.4: Simulation of single period DFB lasing modes.

5.2.2 Experimental results

A number of single period untapered gratings were fabricated within a Fabry-Pérot cavity, the results presented here are indicative of the agreement presented by the full range of results. The DFBs did not lase as expected, most likely due to the relatively small coupling coefficient achieved at this early stage in device fabrication maturity. However, the Fabry-Pérot etalon did allow lasing to occur and hence the characteristics of the grating structures could be inferred. Figure 5.5 shows the LI curve for this device. The threshold is around $90\,mA$ and the device shows a strong gain saturation. The spectrum of the device was taken at a number of injection currents and a sample of the results is presented in Figure 5.6. The mode spacing is around $0.33\,nm$ which corresponds with the Fabry-Pérot modes of the cavity. There is a clear stopband present with the modes at the red end of the spectrum being preferentially excited with increasing injection current. Figure 5.7 shows the consistent stopband more clearly. The stopband is exhibited at around

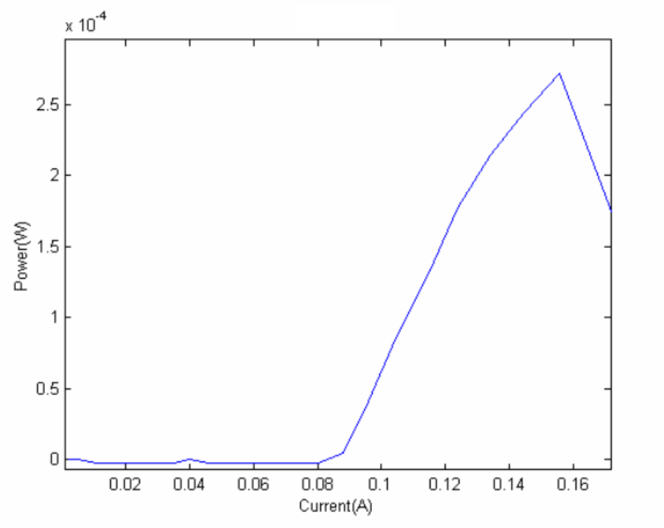

Figure 5.5: LI curve for straight grating within FP cavity device with $100\,nm$ recess depth.

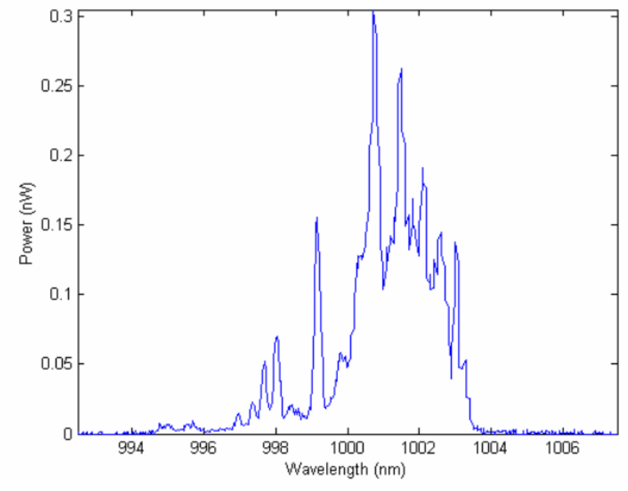

Figure 5.6: Lasing Spectrum of the straight grating with FP cavity device at $270\,mA$.

998.5 nm and is constant with increasing injection current. This measurement gives a good indication of where the centre of the tapered grating devices to be discussed subsequently should arise.

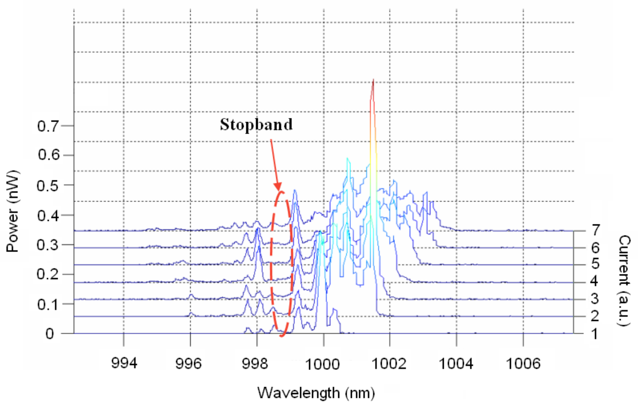

Figure 5.7: Waterfall plot of lasing modes of the straight grating in FP cavity with injection current.

5.3 Apodised, non-linearly chirped DFB lasers

As mentioned previously the main aim for producing the DFB lasers was to exhibit the chirped grating effects. However, at the time of fabrication the technological issues associated with producing gratings with arbitrary coupling coefficient profiles had not been surmounted. Furthermore, it was clear that for constant grating recess depth along the chirped grating, where the chirp is induced by varying waveguide width, a strongly wavelength dependent grating reflectivity would be observed. It was therefore necessary to counteract this problem without recourse to modulation of the grating recess depth. One possible solution to the uneven spread of the stopband is to introduce a non-linearly varying taper function that counteracts the effects of the varying coupling coefficient. Each grating increment, as described previously as a finite section of grating with constant pitch, may be allowed to vary in length, and in doing so the overall reflectivity of the section may be modified. In essence the coupling coefficient is balanced against the effective length of each grating increment. However, it is not practical to create a grating structure with varying incremental lengths, since it is desirable to keep the total device length under direct control. Instead the increase in effective index, induced by change in ridge width, over an increment may be varied. By varying the rate of change of effective index each increment feels the same effect as if under the influence of a varying length of constant pitch sections.

To find the width change over an incremental length of the grating it is necessary to know the average coupling coefficient κ_c, of the grating. From the average coupling coefficient, incremental length and the effective coupling coefficient of each grating section, the effective length of each section may be calculated. The incremental length can be calculated as in (5.2), where m denotes the index of the section under consideration, κ_m is the coupling coefficient of the grating increment with length dz.

$$L_m = \frac{\kappa_c dz}{\kappa_m} \tag{5.2}$$

From the effective length the change in effective index may be calculated.

$$\Delta n_m = \frac{dz}{L_m} dn \tag{5.3}$$

In (5.3) n_m is the change in effective index over the grating section and dn is the change in effective index over a linearly varying grating section. The change in ridge width may then be found from the effective index. A schematic of this device geometry is given in Figure 5.8. Figure 5.9 shows simulations of the transmission spectra for a linearly tapered chirped grating with constant grating recess depth and the associated non-linearly tapered, compensated device. It is clear from Figure 5.9, that by introducing a non-linearly varying taper to counteract the variation in the coupling coefficient, the bandwidth is widened and the peak reflectivity shifted back toward the design wavelength of 980 nm as compared to the linearly tapered grating. The peak reflectivity of the device is reduced as may be expected, and the side lobes on the long wavelength side of the stop band are

Figure 5.8: Schematic of non-linear taper.

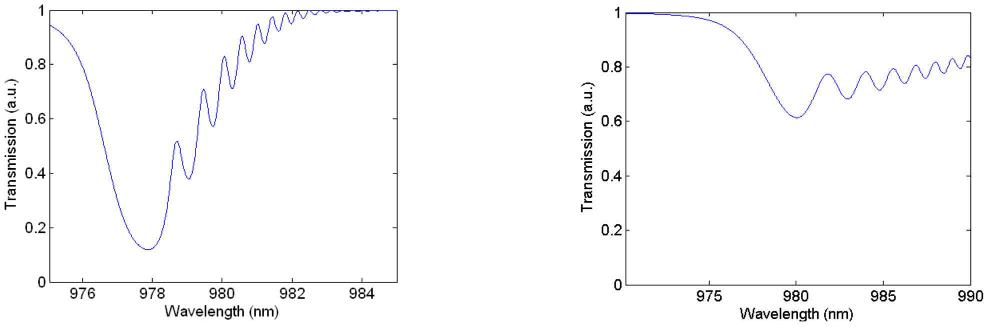

(a)

(b)

Figure 5.9: Simulated transmission spectra of (a) linearly tapered and (b) non-linear apodised grating.

still present. However, the response is closer to the ideal case than the linear taper device. In response to the increased modal gain required for lasing in the non-linear

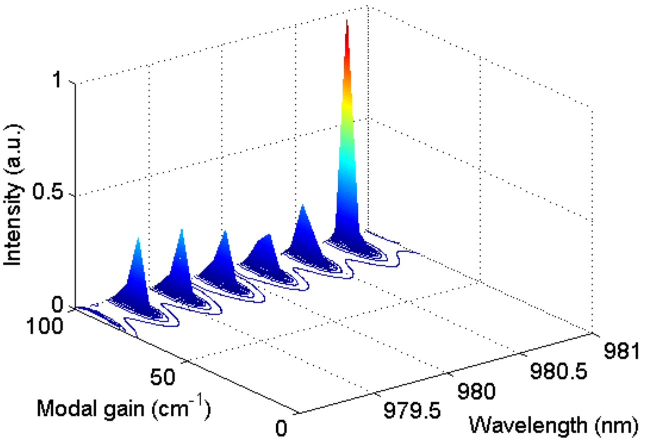

Figure 5.10: Simulation of non-linearly tapered DFB lasing modes.

grating devices, as illustrated in the lasing mode spectrum given in Figure 5.10, a symmetric tapered device may be implemented. The basic geometry of the device is shown in Figure 5.11. It is illustrated in Figure 5.12a that again there is a slight blue shift in the device reflection peak that appeared in the one sided non-linearly tapered device. However, there are now gap modes in the stopband. The occurrence of these is due to the effects of having reflection centres that satisfy the Bragg condition symmetrically placed on either side of the device's central point,

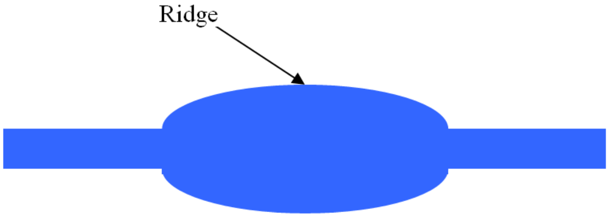

Figure 5.11: Symmetrical taper geometries.

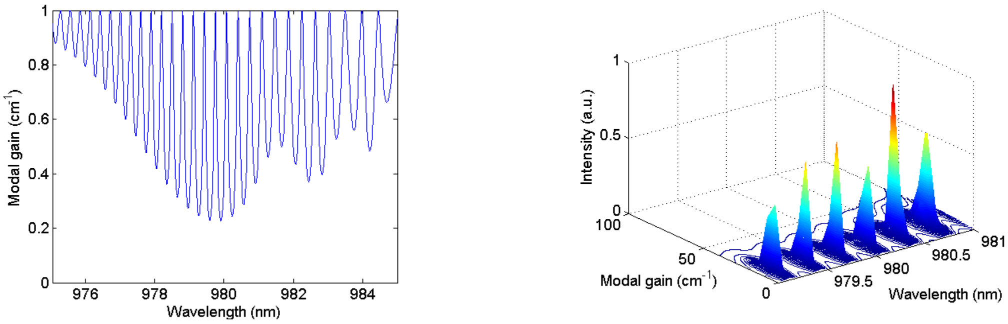

(a) (b)

Figure 5.12: Simulation results for symmetric non-linear apodised grating, (a) Transmission spectrum with zero gain, (b) Lasing modes.

highlighted by the frequency dependent free spectral range of the fringes. One effect of the gap modes suggests a lowering of the necessary modal gain for lasing. Figure 5.12 shows the simulation results for the symmetric non-linear taper device.

Finally it is apparent that there is a limit to the width of the waveguide that may be used in the non-linear taper compensation scheme. This upper limit is imposed by the practical width of waveguide ridge to be written, and the desire to keep from coupling into higher order modes of the waveguide structure. In other words the waveguide was not allowed to increase in width indefinitely, but was saturated at a predetermined value that would persist until the ideal waveguide width dropped below that width on the narrowing taper side. The device structure is illustrated in Figure 5.13. By capping the waveguide width at $2\,\mu m$ it was hoped to avoid the problems associated with coupling to higher order transverse waveguide modes. A device with a non-linear taper capped at $2\,\mu m$ was simulated

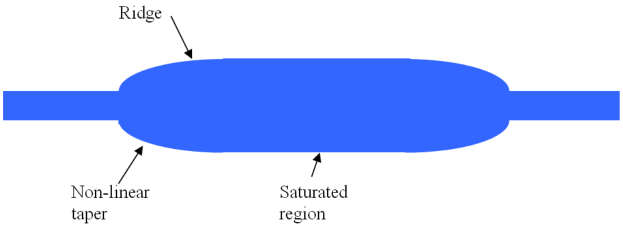

Figure 5.13: Symmetrical non-linear taper with saturated width.

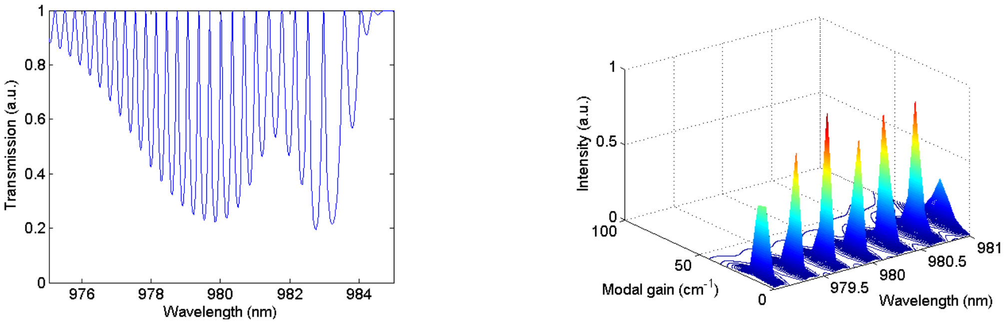

(a) (b)

Figure 5.14: Simulation results for saturated symmetric non-linear apodised grating, (a) Transmission spectrum with zero gain, (b) Lasing modes.

and the results are presented in Figure 5.14. It is apparent that the modified non-linear taper has a number of benefits. It still presents the series of gap modes in the transmission spectrum, however, although the stopband is almost the same as the unsaturated grating case, it shows a slight increase in reflectivity of the long wavelength portion as would be expected by elongating that portion of the grating by capping the width variation. The simulation presented in Figure 5.14 is due to a taper geometry with $W_1 = 1\,\mu m$, $W_{sat} = 2\,\mu m$ and recess depth $d = 100\,nm$. A secondary simulation was also carried out with the same waveguide parameters except for $W_1 = 1.5\,\mu m$. The result of this simulation is shown in Figure 5.15. Figure 5.15 shows that the gain required for lasing has increased from the $W_1 = 1\,\mu m$ case. This is expected since the grating average coupling coefficient is reduced and so the reflectivity is reduced leading to a higher gain requirement for lasing. Secondly there is in interesting feature of the predicted lasing modes. The equally spaced modes are still present but the simulation suggests that each alternate mode will preferentially lase in this geometry.

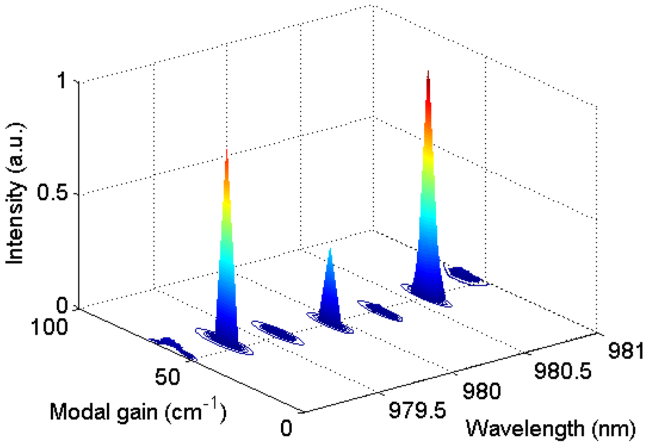

Figure 5.15: Simulated lasing spectrum of saturated non-linear tapered DFB, $W_1 = 1.5\,\mu m, W_2 = 2\,\mu m$

5.3.1 Experimental results

Symmetric non-linear taper with $100\,nm$ recess depth and $W_1 = 1\,\mu m$

The LI curve of the device is similar in form to that illustrated previously in Figure 5.5 with a threshold current of around $150\,mA$ and strong gain saturation. The spectrum was taken on a range of injection currents and a sample result at $375\,mA$ injection current is presented in Figure 5.16. Above threshold the device shows evenly spaced modes repeating around $0.5\,nm$ as predicted by the simulation. There is also a trend for the lasing power to experience a redshift with increasing injection current. The mode spacing and position however, remain constant with increasing current.

The lasing bandwidth of the evenly spaced modes is almost $10\,nm$ at $100\,mA$ injection current which also agrees with the simulations which show modes with even spacing and flat gain profile with around $10\,nm$ span. Of course the gain spectrum of the material will also affect the lasing mode profile, but the agreement seen here is certainly encouraging.

Symmetric non-linear taper $W_1 = 1.5\,\mu m$.

A further variation of the symmetric non-linear DFB was investigated where the waveguide taper was reduced from $1-2\,\mu m$ to $1.5-2\,\mu m$. The reduction

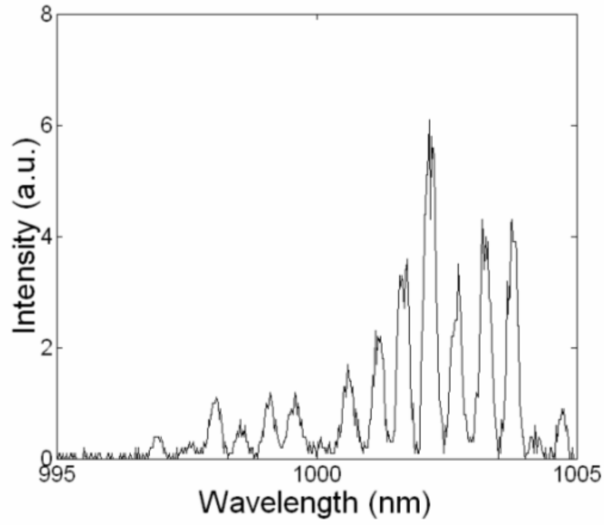

Figure 5.16: Lasing Spectrum of the Symmetric Non-Linear Taper Device at 375mA.

of the taper geometry results in a narrowing of the device bandwidth and a drop in peak reflectivity. The effect on the laser output is to increase the necessary gain required for lasing as outlined above. The LI curve for this device is of the same form as previously discussed with a threshold again around $150\,mA$ and a strong gain saturation. The spectrum of the device is shown in Figure 5.17. The mode spacing is the same as the wider taper device however, every second mode in the spectrum seems to be suppressed somewhat. Simulation results for this reduced taper device interestingly showed that alternate modes were favoured in the flattened gain regime as previously discussed, also matching very well with the experimental results.

Finally, it is useful to directly compare the simulated and measured lasing spectra for the fabricated devices outlined above. The comparisons are presented in Figure 5.18. The results show close agreement of the simulations with the fabricated results, confirming that coupled functions of the grating chirp and apodisation may be accurately fabricated by the means presented.

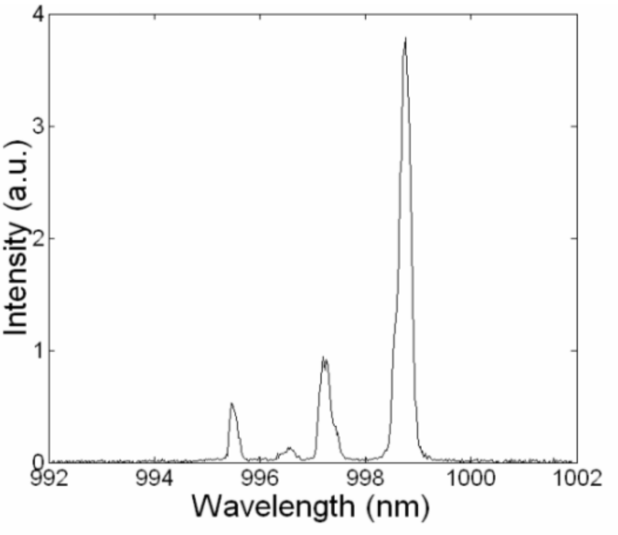

Figure 5.17: Lasing Spectrum of the reduced taper symmetric non-linear taper device at $210\,mA$.

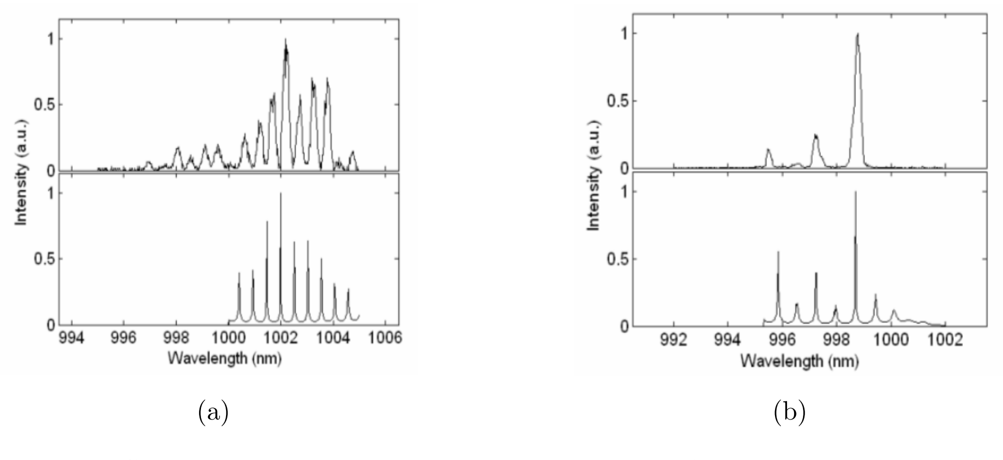

(a) (b)

Figure 5.18: Simulation and measured device results of saturated symmetric non-linear apodised grating (a) $W_1 = 1\,\mu m$, (b) $W_1 = 1.5\,\mu m$.

5.4 Conclusions

In this chapter DFB lasers based on tapered chirped Bragg gratings were presented. A scheme by which κ may be modulated without recourse to variation of the grating recess depth was implemented, and shown to produce devices that lased with interesting multimode behaviour. Whilst the devices do not provide a direct measurement technique for the grating amplitude and phase, their behaviour, matching well with that predicted by the TMM model, gave confidence in the grating design at an early stage in the fabrication optimisation process. The lasing behaviour of the devices provides a wider indication of the grating performance than a transmission measurement alone, allowing further development of devices that may be subsequently measured as detailed in Chapter 4.

Chapter 6

Tapers

In this work the main body of effort has been directed towards developing tapered deeply etched integrated grating structures. Necessarily, if these devices are to be implemented within integrated optical circuits they must be compatible with currently available technologies. Towards this aim of integration it is clear that an efficient and compact mode converter is required. Optical mode converters are used as an interface between planar systems of different functionality and hence varying modal profile [103–105]. In III-V material systems mode converters may be used as a means to couple light between deep and shallow etched ridge waveguides where, due to their unique properties it is often advantageous to implement both in the fabrication of a single system. The strong lateral confinement and high index contrast of deep etched waveguides allows for tight waveguide bends, novel grating devices and high-frequency components. However, these guides exhibit relatively high waveguide losses and are hence less suited for applications as interconnects, or in active structures where scattering losses and surface recombination may prove problematic. Previous work carried out into designing adiabatic tapers has focused both on the geometry of the taper [104–107] and its spatially dependent refractive index profile [108, 109], as both are required for strict adiabatic propagation [110]. However, it requires long device lengths to produce efficient tapers with simple linear and parabolic profiles and involved fabrication methods to create the requisite refractive index gradients for strict adiabaticity. In this chapter a double etched deep to shallow taper device, in addition to optimised taper profile design, is presented in order to produce adiabatic, single mode propagation on sub $100\,\mu m$ length scales, without recourse to refractive index modulation. For compatibility with photonic integrated circuits, especially those incorporating semiconductor optical amplifiers, they are required to exhibit both low reflectivity and loss. The resultant geometries are simulated using Finite Difference Time Domain (FDTD) and Transfer Matrix Methods (TMM) and compared with fabricated device results. In general, the lateral confinement of the deeply etched waveguide will be much greater than that of the shallow etched section, and therefore a larger cross-section width is required to match with the shallow etched guide. It is assumed in this case that the vertical confinement of both regimes is closely matched due to the epilayer structure which remains constant throughout the device. Therefore, since the width of the deeply etched waveguide is dictated by the grating structure, a means to expand the mode to match the shallow etched section was sought.

The literature presents a number of alternatives for the purposes of mode transformation in both fibres [111] and in integrated guides [44, 103–109, 112]. There are two essential elements in any proposed taper solution, firstly that the mode is transformed with little conversion into higher order guided modes, and secondly that there is minimal loss in the structure to radiation or leaky modes. Adiabatic tapers are defined as those meeting the aforementioned conditions, but more generally as structures that closely approach these conditions. In this work, following the convention of Marcatili [110] tapers that exhibit lossless and conversionless nature will be referred to as strictly adiabatic, with those close approximations being adiabatic. In the ideal case of a straight waveguide the spatial mode profile may be solved for by direct solution of Maxwell's equations given the boundary conditions. Since the waveguide structure does not vary with propagation length it is obvious then that this same solution applies along the propagation length of the structure and hence the mode should travel - in the absence of losses and other non-ideal factors such as waveguide roughness - without perturbation. However, in the case of the tapered waveguide the section of the structure can be considered as a continuously varying function and as such will require solution of the Maxwell's equations at each point. If the solution to this structure is not constant along its length then the mode will experience coupling between the fundamental mode and other higher order guided modes or radiative modes. The problem it seems resolves itself into two possible routes; either a perfect matching of solutions to Maxwell's equations may be sought along the taper length, or an approximation to the perfect adiabatic condition may be allowed given necessary concessions to the practicalities of device fabrication.

In the first case where perfect adiabaticity is sought, an excellent paper by Marcatili [110] has been presented in which the author defines a method to significantly ease the problems associated with consistent solution of the Maxwell's equations with varying spatial waveguide section. The author proposes that by recasting the equations into a non-Cartesian coordinate system the Maxwell's equations may be solved easily within that system. Therefore, in the case of a linearly varying taper the system may be constructed in polar space where the boundaries of the waveguide coincide with the principle axes of the coordinate system, making solution of the Maxwell's equations significantly easier. Figure 6.1 illustrates the system in which a linear taper may be approached. By recasting these equations in polar coordinates however, there is an implicit transform of the system that requires attention. The refractive index of the waveguide becomes, rather than the assumed constant that we are used to, a function of the coordinates, so that for adiabatic propagation of the mode the index of the waveguide must be variable. The author also casts curved, sublinear and superlinear, tapers [110] by recourse to elliptical coordinates in his work. So although this is an extremely elegant and powerful method for the design and solution of lossless tapers it includes in its workings the assumption that the necessary variable refractive index within the waveguide structures may be fabricated. As will be discussed, this is not an assumption that is easily contended with when considering real fabrication.

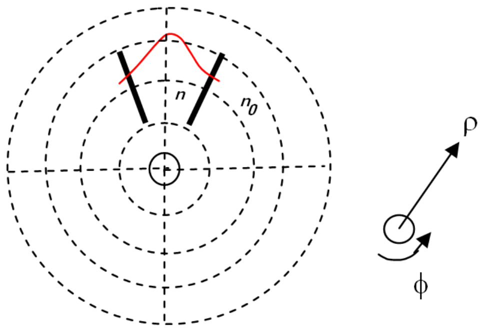

Figure 6.1: Linear taper in polar coordinates.

A second method for strict adiabcity is presented by Lee et. al. [113] based on conformal mapping. In this case a method for mapping a simple straight waveguide - being strictly adiabatic as previously discussed - onto a waveguide with varying spatial cross section is presented. As in any conformal mapping scheme the object of the analysis is to continuosly transform one domain into another. In the work presented by Lee the authors constrain the secondary domain - that which will contain the taper - by predefining two sections of waveguide with an indeterminate intermediary section to be calculated via the conformal mapping. However, this transform method requires that not only the physical waveguide dimensions be modulated but also the refractive index. So, although this method is another powerful tool in the design of strict adiabatic tapers for arbitrary mode size conversions, it retains the limiting factor of the Marcatili method that demands the fabrication of variable refractive index waveguides.

The bulk of published research into waveguide tapers has been directed towards applications in SOI devices with particular interest in conversion of waveguide modes for matching with optical fibres [44, 112], and conversion of waveguide cross-section [103–105, 107–109]. The main focus of the work has been divided into two areas. Firstly, some work has been done in tackling the problem of varying the refractive index of the waveguide along its length. Cheben et. al. [44] propose the use of a subwavelength grating - as outlined in section 3.1 - to vary the effective index of the propagating mode that may be used in addition to a spatial taper for mode matching with optical fibre. Another attempt to resolve this issue is made by fabrication of waveguides using Flame Hydrolysis Deposition (FHD) to deposit the waveguiding layer [109]. By so doing it is shown that by varying the deposition parameters the depth and density of the FHD layer may be varied across the sample surface and so produce varying refractive index conditions favourable for the production of adiabatic tapers designed using a constant V parameter method. In addition to these methods a device structure is proposed using two overlapping tapered waveguide sections with distinct refractive indices to induce the total modal index observed by the mode. Figure 6.2 shows the dual taper device structure presented by Yamaguchi et. al. [108]. However, since the work presented in this thesis is based on III-V materials and it is therefore more difficult to pursue variable refractive index waveguides it seems more prudent to follow a taper design that assumes a constant material refractive index. To this end a number of device geometries have been proposed in particular those by Solhemainen [107] and Dai [104, 105] that are concerned with double etched taper structures. Double etched waveguides are those that are etched first with one pattern then undergo

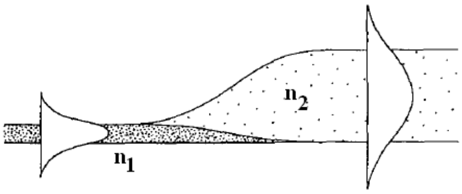

Figure 6.2: Overlapped taper[108].

a secondary lithographic step to etch a secondary mesa into the structure. The double etching process is shown in Figure 6.3. In the aforementioned works the authors present taper structures that are consistent of two taper sections, an upper and a lower. The lower taper may be considered as a lateral expansion section for the strip waveguide leading into the ridge section. The upper taper gradually increases the ridge width to transpose the mode from the strip guide into the ridge section. A schematic of the double etched taper device is shown in Figure 6.4.

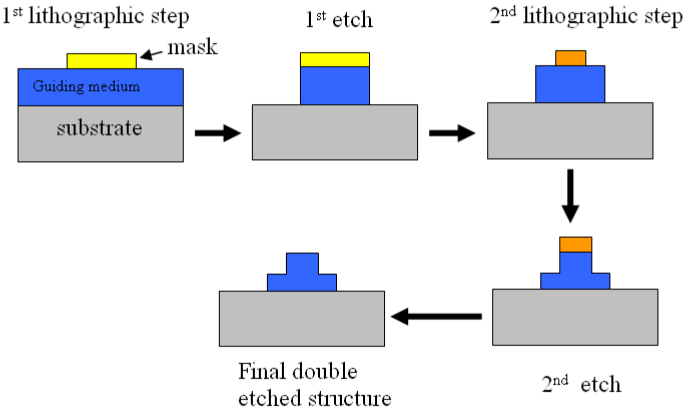

Figure 6.3: Double mask technique.

The strip to ridge taper may be easily transposed into a deep etched to shallow etched III-V material system waveguide setting. In III-V materials, both lateral, vertical and combinatorial tapers have been in use in integrated devices for some time and for many applications, a useful review of these taper geometries residing in the paper by Moerman [106]. However, although much work has been done on bulk taper geometries there has been little rigour shown in the design of the actual

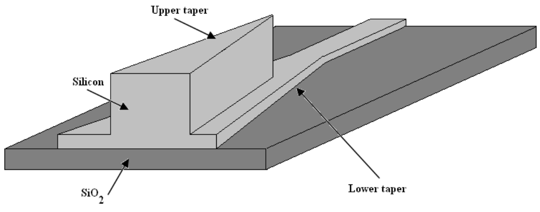

Figure 6.4: Double etched taper.

taper functions themselves, with most authors content in using the standard linear, parabolic or sine taper functions. The reason for this is not hard to fathom, as in the bulk of the work it is SOI devices that are considered and therefore the losses in the waveguides to be contended with are very small, as low as $0.2\,dB/cm$. With such low losses it is not an issue to let the taper lengths run to hundreds of microns at which scale the exact taper function is indeed not entirely critical to adiabatic function. However, since it is III-V materials that are being considered here, with their associated higher losses and a requirement to keep as small a device length as possible, the taper function itself is of great interest.

Aside from the coordinate transform and conformal mapping method, both of which require a variation of refractive index, there are models that may be used to calculate the optimal function for a waveguide taper. In these methods it is attempted to produce a taper of minimal length as offset by the coupling of the fundamental propagating mode into higher order guided modes or radiation modes. In effect they are approximate methods by with adiabatic propagation may be balanced against the propagation length.

The first of these methods is presented by Love et. al. [111] and is directed primarily for use with optical fibre propagation. However, the method may be taken as general and is transposable into a planar waveguide system. Firstly it is stated that at any section of the waveguide the structure may be solved for its guided and radiative modes and their associated effective refractive indices. It is then assumed that if it is required to vary the lateral dimension of the waveguide then the length over which that is achieved must be much larger than the beat length between the fundamental propagating mode and the mode with the closest effective index. The beat length condition is taken as the delineating point between adiabatic and lossy waveguides and is then used to calculate the critical angle of the waveguide at any given section as described by (6.1).

$$\Omega = \frac{1}{C}\frac{a(\beta_1 - \beta_2)}{2\pi} \tag{6.1}$$

In (6.1), Ω is the critical taper angle at a waveguide width of a, β_1 and β_2 are the propagation constants of the fundamental and closest matching mode and C is the constant normalised coupling coefficient. There are a number of interesting cases where the value for the secondary propagation constant takes on specific meaning. Firstly, if the waveguide is single moded but has a finite cladding then the second mode will be that of the closest matching cladding mode, secondly if the single moded guide is surrounded by effectively infinite cladding then the closest matching mode will be that of the radiative modes in the cladding and finally if the guide is multimoded then the secondary mode will be that of the closest matching guided mode. Figure 6.5 shows a schematic of the possible coupling between the fundamental guided mode and those others described. After definition of the relevant modal propagation constant, the taper profile may be extracted by integrating the critical angle of the taper over the lateral change in waveguide width, producing the optimal waveguide taper function.

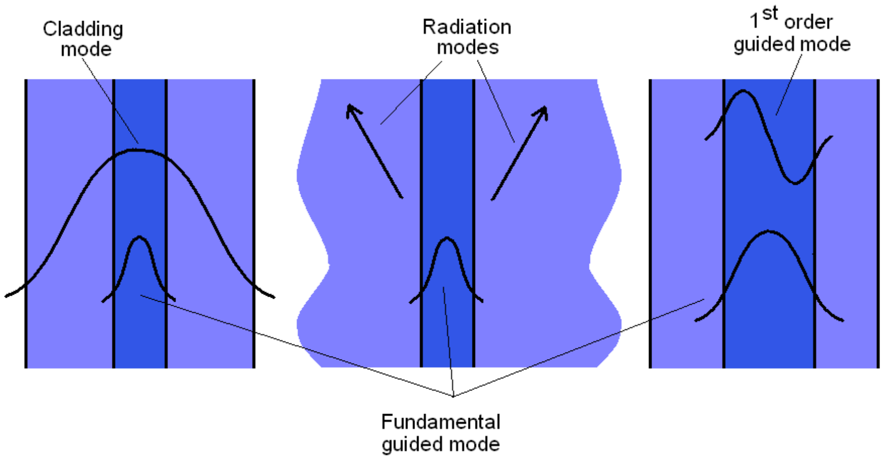

Figure 6.5: Possible coupling of fundamental guided mode to, cladding, radiative and 1^{st} order guided modes.

An alternative to the method proposed by Love, is submitted by Vassallo [114].

In his work Vassallo presents a method in which the taper profile is limited by the rate of change of mode cross section with propagation length over a laterally varying waveguide structure. The same assertion stated by Love is applied here, that a change in waveguide structure induces a coupling between the fundamental propagating mode and other guided and radiated modes of the structure. The rate of change of modal power in any given mode of the structure with rate of change of fundamental modal profile may be related as given in (6.2).

$$\frac{\partial S_m}{\partial z} \approx -\left\langle \phi_m^* \frac{\partial \phi_0}{\partial z} \right\rangle exp\left(i \int_0^z (\beta_m - \beta_0)\, dz \right) S_0 \tag{6.2}$$

In (6.2) S_0 and S_m are the powers of the fundamental and m^{th} modes of the structure, ϕ_0 and ϕ_m are the modal solutions in the transverse direction of the fundamental and m^{th} order modes, and β_0 and β_m are the propagation constants of the fundamental and m^{th} order modes respectively. For coupling to remain negligible it is necessary that $\left\langle \phi_m^* \frac{\partial \phi_0}{\partial z} \right\rangle \ll (\beta_m - \beta_0)$. The $\ll$ may be replaced by a strict inequality by introducing a factor F, where $F \gg 1$. The limiting factor on the rate of change of taper width with length may then be written as in (6.3), where $\frac{\partial \phi_0}{\partial a}$ is the rate of change of the fundamental modal profile with waveguide width, and $\left(\frac{\partial a}{\partial z}\right)_c$ is the critical rate of change of waveguide width with length.

$$\left(\frac{\partial a}{\partial z} \right)_c = \frac{(\beta_m - \beta_0)}{F \left\langle \left| \frac{\partial \phi_0}{\partial a} \right|^2 \right\rangle^{\frac{1}{2}}} \tag{6.3}$$

From (6.3) the optimal waveguide taper function may be extracted by integrating the reciprocal of the rate of change of width with length over the required waveguide width variation. As in the case of the method proposed by Love, the closest mode propagation constant is defined by the waveguide structure and may take the form of that associated with guided, radiative or cladding modes.

6.1 Design and fabrication

In this work the taper is to couple light from a shallow etched waveguide to a deeply etched section with refractive index solely defined by the material structure and waveguide section. A double etched waveguide solution may be used and the taper profile defined by standard approximations or by the optimised methods previously outlined. To assess the optimal design for the applications in this work a number of taper designs were simulated and fabricated in order to compare the reflectivity and loss produced by each design. The waveguides were all fabricated on the same $Al_xGa_{1-x}As$ material described in Chapter 4, and both the shallow and deep etched waveguides were designed with a waveguide width of $2\,\mu m$. The waveguide width was chosen as this allows both enough area for current injection - whilst remaining single moded - in the shallow etched ridge regime, and corresponds to the grating work in deeply etched waveguides already undertaken.

6.1.1 Fabrication method

The fabrication procedure for the tapers and waveguides was carried out using a double lithography process similar to that outlined previously [107]. First gold markers were deposited on the sample to allow alignment of the various lithographic steps carried out. The deep etched waveguides and the deeply etched envelope waveguides were defined first in HSQ and subsequently deeply etched into the semiconductor with a $SiCl_4$ RIE. Since the etch depth of the features was around $2\,\mu m$ the secondary lithography step had to be carried out using a thick bilayer of PMMA in order to ensure that the resist fully coated the sidewalls of the deeply etched features. The shallow etched features were then transferred into the resist, with careful consideration of proximitiy effects taken into account due to the very narrow width of the taper features, using the VB6 electron-beam lithography tool. The pattern was etched into a silica hardmask followed by second RIE process in $SiCl_4$ which was then carried out to etch the shallow features. The fabrication process is shown in Figure 6.6. The waveguides fabricated were of the form of a deeply etched waveguide followed by a taper transition section into a shallow etched waveguide as illustrated in Figure 6.7.

6.1.2 Deep to shallow etch transition devices

As a baseline by which to judge the performance of the optimised double etched tapers two other device geometries were fabricated. The first was a direct deep to shallow etch waveguide transition that was designed without appeal to mode-matching or taper optimisation processes where both deep and shallow etched

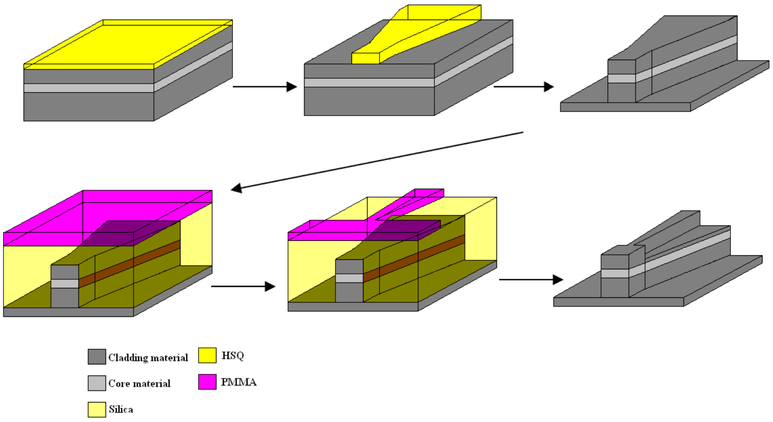

Figure 6.6: Taper fabrication.

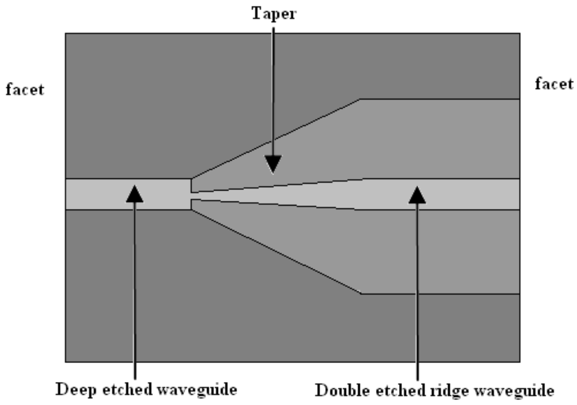

Figure 6.7: Taper sample.

waveguides were matched in physical width. The direct transition as fabricated on GaAs:AlGaAs is shown in Figure 6.8. The second device design to be tested was based on a horn taper. In this geometry the deeply etched section is linearly tapered to a width larger than that which would match the shallow etched mode. The horn taper is shown in Figure 6.9. Given the constraints previously mentioned, double etched tapers were designed using the adiabatic taper approximations previously outlined. The first taper design implemented was based on the method presented by Love [111]. The modes of the structure, for varying waveguide width, were calculated using the FIMMWAVE package, and the results used to calculate the taper profile as described. However, if the tapers were designed

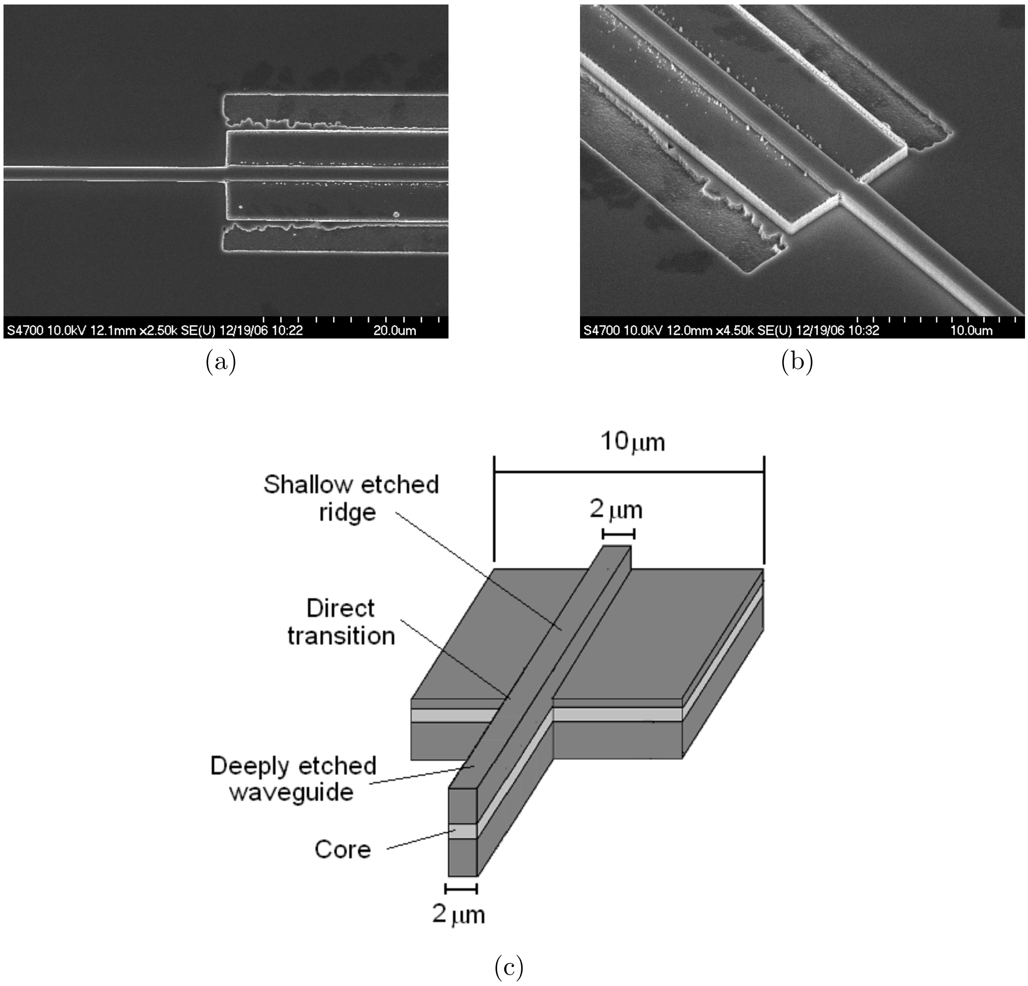

(a) (b)

(c)

Figure 6.8: Direct transition between deep and shallow etched waveguides (a),(b) SEM images and (c) schematic.

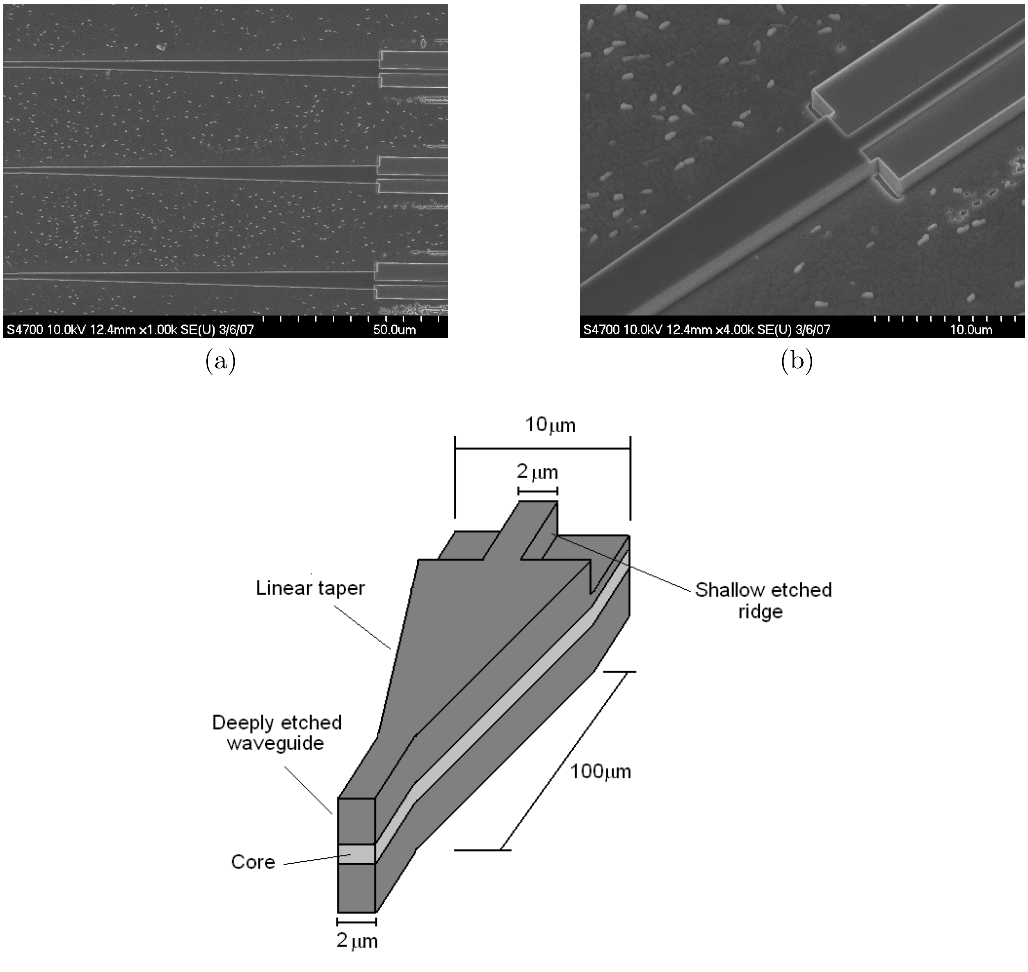

(a) (b)

(c)

Figure 6.9: Horn taper device (a),(b) SEM images and (c) schematic.

using a beat length defined by association with the closest order guided mode the method produced a device with a length in excess of $1.2\,mm$. Clearly, a millimetre scale device is not feasible for application in integrated optical devices. As a method to reduce the length of the device to more reasonable scales the secondary mode considered was that of the radiation condition. As an approximation the effect of this substitution is to create a less than adiabatic taper, however, it creates a device with a lengthscale in terms of tens of micrometres. It was predicted that this change, although the taper would be less efficient than in the ideal case, should still exhibit good conversion and loss characteristics. In addition there is an important point to consider when regarding the two tapers of the double etched structure. As described earlier the fundamental mode may couple to higher order guided modes, cladding modes or radiation modes of the waveguide structure and in the case of the upper taper, which gradually tapers from below cutoff to the ridge of the shallow etched waveguide section, the coupled modes are taken as the radiative modes into a pseudo-infinite cladding. The cladding modes of the upper taper clearly will exhibit much higher effective indices than those radiative modes of the lower taper where in effect the lateral waveguide cladding is air. The effect of this difference is to produce two tapers of varying profile, the upper taper length being greater than the lower. A second taper variation was also fabricated in which the lower taper profile was approximated to a linear variation whose length matched the upper taper, and so providing a more gentle variation than the calculated profile. The fabricated double-etched taper device based on the Love approximation is shown in Figure 6.10. The second, linearly varying lower taper device, is shown in Figure 6.11.

An alternative approximation to the adiabatic criterion was presented by Vassalo. In this case the adiabatic criterion was calculated given the rate of change of the mode profile with waveguide width and the difference in propagation constants between the fundamental mode and the mode of the structure with the nearest index of refraction and as such presents a more general method than that proposed by Love. As before this method produced extremely long devices, and so the radiation mode approximation was used again. Also, as in the case of the adiabatic tapers based on Love's method, tapers with ideal deeply etched envelopes and slowly varying linearly tapered envelopes were fabricated. To design the structures the modal cross sections of the both shallow and deeply etched waveguides were

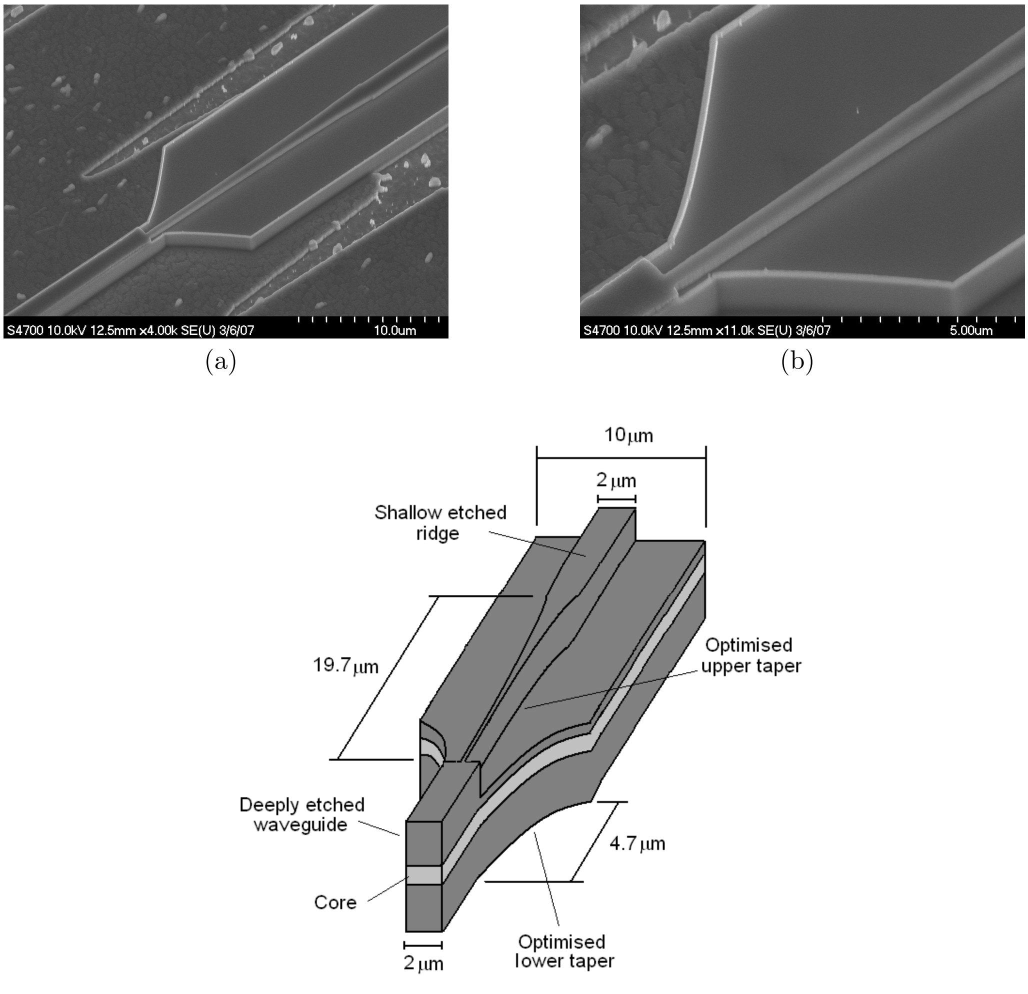

(a) (b)

(c)

Figure 6.10: Adiabatic taper device (Love), (a),(b) SEM images and (c) schematic.

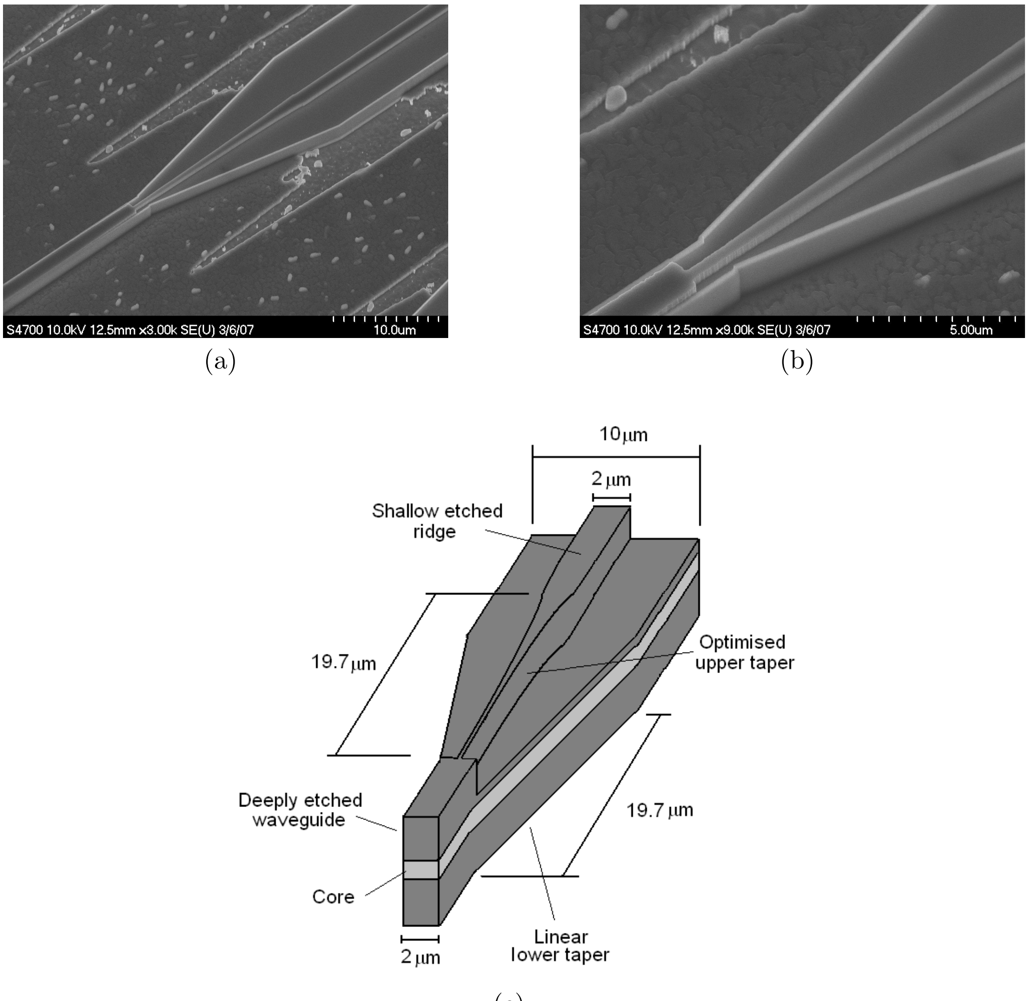

(a) (b)

(c)

Figure 6.11: Adiabatic taper device (Love), (a),(b) SEM images and (c) schematic.

simulated for a range of waveguide dimensions using the FIMMWAVE package. The rate of change of modal power in the mode cross section was then calculated as a function of the waveguide width for both cases and, given the extreme taper dimensions, used to solve for the optimised taper function as described. The devices with optimised upper and lower tapers are shown in Figure 6.12, and the devices with linear lower tapers are shown in Figure 6.13.

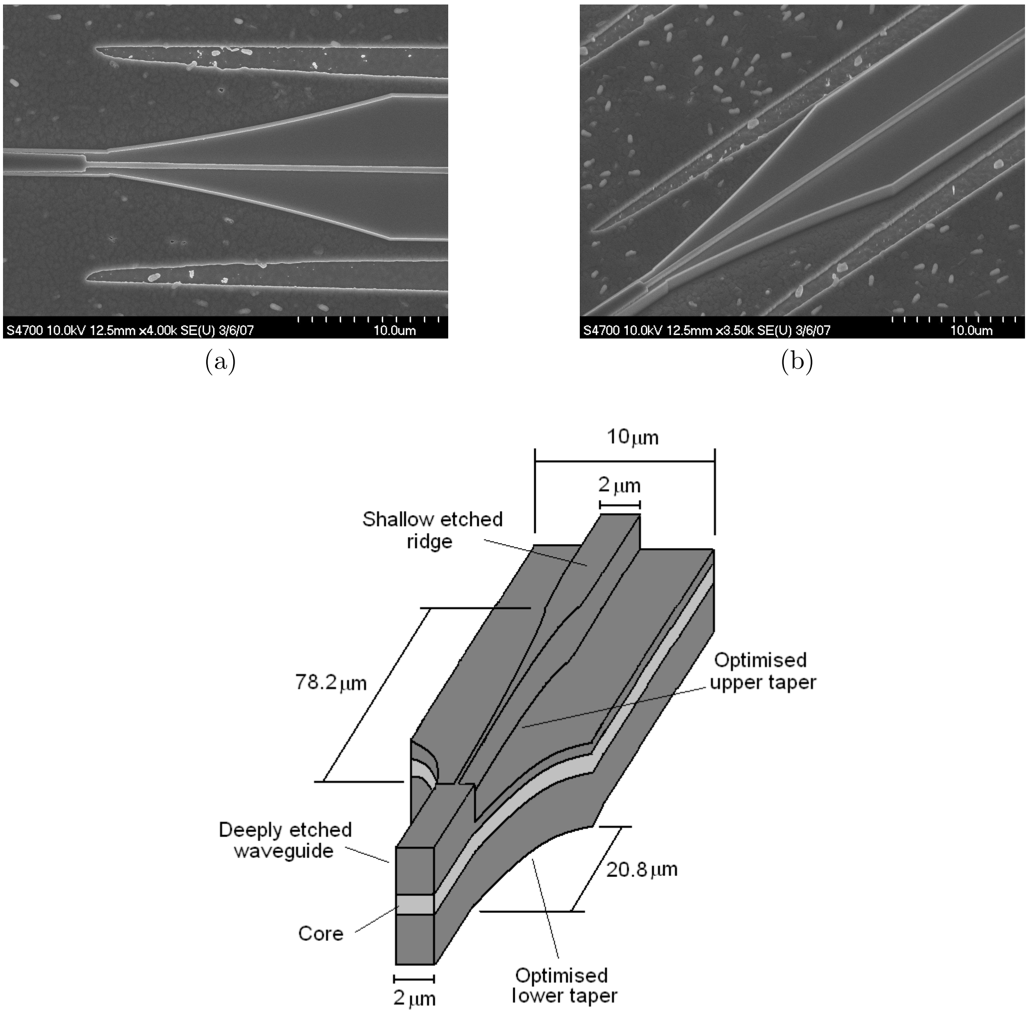

(a) (b)

(c)

Figure 6.12: Adiabatic taper device (Vassalo), (a),(b) SEM images and (c) schematic.

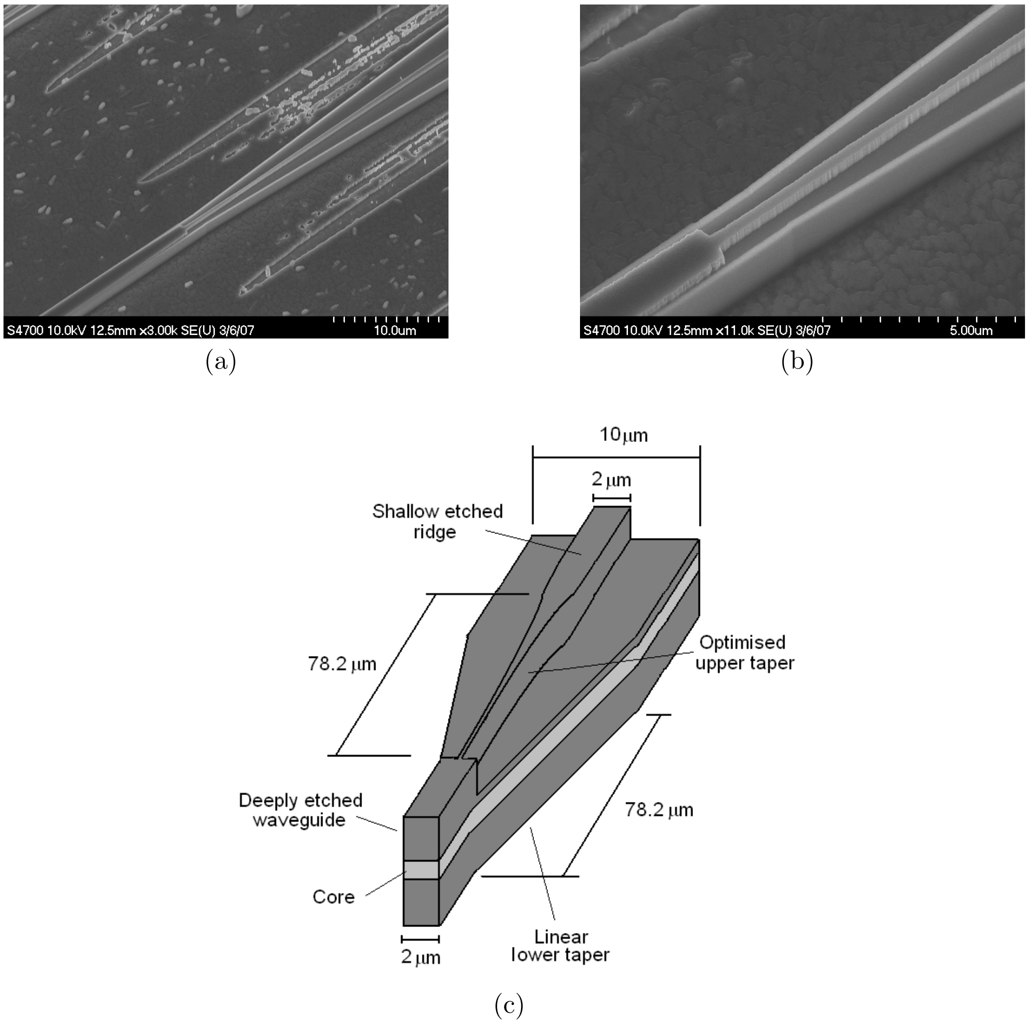

(a) (b)

(c)

Figure 6.13: Adiabatic taper device with linear lower taper (Vassalo), (a),(b) SEM images and (c) schematic.

6.2 Simulation

It was undertaken to simulate the tapered devices as outlined above in order to make a comparison with the results of the fabricated devices. The simulations were carried out using a $2D$ Finite Difference Time Domain (FDTD) package produced by Lumerical. The spatial and temporal grid conditions were calculated using the conditions presented by Taflove [115], with the spatial grid defined as $\lambda/20$, where λ is the wavelength of propagation in the semiconductor, and a time step of $dt = \frac{1}{c\sqrt{\left(\frac{1}{dx}\right)^2+\left(\frac{1}{dy}\right)^2}}$, where dx and dy are the spatial grid dimensions. The tapers as previously described were directly transcribed into the FDTD simulation system using effective index values for the various etched sections of the dielectric material. A pulse was injected into the fundamental mode of one end of the waveguide and the power monitored at both the output and input ends. The computational domain was surrounded by a Perfectly Matched Layer (PML) absorbing boundary condition to avoid reflections from the domain edges.

In order to calculate the reflectivity and loss of the device the total power in the reflected, transmitted and injected modes were calculated and used in the relations given in (6.4), (6.5) and (6.6).

$$R = P_{reflected}/P_{source} \tag{6.4}$$

$$T = P_{transmitted}/P_{source} \tag{6.5}$$

$$Loss = 10log_{10}\left(\frac{P_{source} - (P_{reflected} + P_{transmitted})}{P_{source}}\right) \tag{6.6}$$

6.3 Measurement technique

The fabricated taper devices were measured in the tunable laser setup as previously described in Chapter 4. As before, since the taper devices are situated in waveguides terminating in cleaved facets, Fabry-Pérot fringes should be apparent as the input wavelength of the laser is varied. The loss of the waveguides that affects the form of these fringes is in this occasion consistent of both a deeply and shallow etched section that will each have a different loss per unit length of propagation. Examples of both shallow and deeply etched waveguides were fabricated on the sample to extract the values for these losses in the usual manner. In addition to the Fabry-Pérot fringes associated with the facets it was conjectured that the reflections from the taper section would result in secondary resonances, and that since the taper is not situated at the exact centre of the sample, and hence the shallow and deep etched sections were of different lengths, these secondary resonances would be of distinct frequencies. Given that the loss of the straight waveguide sections is known as is the facet reflectivities then the loss of the taper structure may be found by extracting the primary Fabry-Pérot resonance and calculating its loss. The loss of the taper is then given as the difference between the known loss of the waveguides without the taper and that of the devices incorporating taper devices. Subsequently, since the loss of the system is known, and the resonances of the two subcavities, one corresponding to the shallow etch to deep etch transition and the other in the opposite direction, may be extracted by Fourier analysis, the reflectivities of each of the cavities may be calculated by rearranging the loss calculation equation, (3.7), given previously in section 3.3.2.

$$R_{taper} = \frac{\left(\frac{(1-(1-K^2)^{0.5})}{K} exp(\alpha_n L_n)\right)^2}{R_{facet}} \tag{6.7}$$

In (6.7) R_{taper} is the reflectivity of the taper in one direction, R_{facet} is the facet reflectivity, α_n is the waveguide loss per unit length of the relevant waveguide section and L_n is the length of that waveguide section. K is the contrast of the Fabry-Pérot fringes as described previously and given as $K = \frac{I_{max}-I_{min}}{I_{max}+I_{min}}$, where I is the wavelength dependent intensity of the transmission spectrum of the device.

It was noted that given the assumption that the taper is a non-symmetric reflector, the entire system may be modelled in a TMM system. The block representation of the matrix model of the system is shown in Figure 6.14. The model as

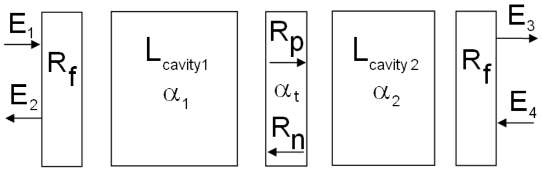

Figure 6.14: Taper matrix model.

shown in Figure 6.14 includes both directionally dependent reflectivities, taper loss and waveguide losses. The extracted results of the fabricated devices were input as parameters in the matrix model to confirm the operation of the waveguide cavities. The example given in Figure 6.15 is of a device with a direct deep to shallow etch transition. As is evident in Figure 6.15 there is close matching between the measured results and the matrix model giving confidence that the analysis method used to extract the reflectivity and loss parameters from the experimental results is valid. Therefore, the reflectivities of the tapered devices may be extracted from the transmission spectrum results by curve-fitting these against the ideal TMM model, where the directionally dependent reflectivities are the variables being fitted, with the physical waveguide parameters and device loss as inputs to the model. The curve-fitting method follows the same method as that used in section 4.2 where the grating element parameters were sought. Here the grating element is simply replaced with the lossy, directionally dependent reflector model.

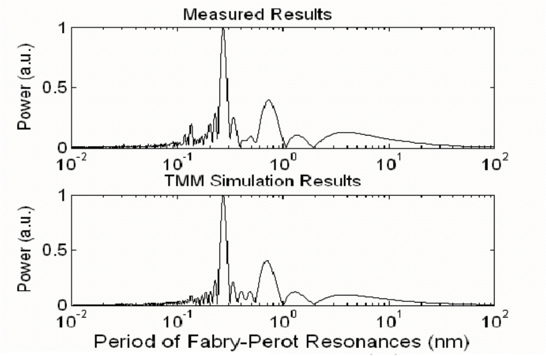

Figure 6.15: Sample measured and simulated Fourier transforms of transmission spectra for a direct transition device.

6.4 Results

The lengths of the taper designs, both upper and lower tapers are given in Table 6.1. The values for devices losses for the FDTD simulations and measured devices are presented in Table 6.2. The simulated and measured device reflectivities are given in Table 6.3. In addition to the FDTD simulations of ideal devices, Table 6.3 also presents FDTD simulation results for devices with a lateral offset misalignment between the two taper layers of $0.3\,\mu m$. These offset device simulations were included to assess the effects of misalignment between the two lithography steps required to fabricate the tapers, where $0.3\,\mu m$ was taken as an outside value for the misalignment that may occur in the fabrication procedure outlined above.

Table 6.1: Taper lengths.

Device	Taper Length (μm)	
	Lower Taper	Upper Taper
Direct Transition	–	–
Horn Taper (Intense)	100	–
Adiabatic (Love)	4.7	19.7
Adiabatic (Love), linear lower taper	19.7	19.7
Adiabatic (Vassallo)	20.8	78.2
Adiabatic (Vassallo), linear lower taper	78.2	78.2

Table 6.2: Taper loss results.

Device	Taper Losses (dB)		
	FDTD (ideal)	FDTD ($0.3\,\mu m$ offset)	Measured
Direct Transition	0.2	0.3	1.1
Horn Taper	0.5	0.5	2.2
Adiabatic (Love)	0.4	0.4	1.1
Adiabatic (Vassallo)	0.1	0.1	0.4

As may be expected the devices with lower linear tapers exhibited better performance than those with optimised profiles, as the linear taper being a slower variation in width with propagation length is closer to the ideal situation, where no approximation as to the index of the secondary modes has been made as discussed previously. The results presented for the adiabatic tapers in Table 6.2 and Table 6.3 then are those for the linear lower taper variations of those geometries. There is good agreement between the simulated results from the FDTD method and the measured devices. The first point to notice is that the measured losses, although following the same trend as those calculated in the FDTD method, are slightly larger. This result is anticipated as the effects of sidewall roughness and other fabrication imperfections are not taken into account in the FDTD model. In

Table 6.3: Taper reflectivity results.

Device	Reflectivity Shallow to Deep etch (%) FDTD (ideal)	 FDTD (0.3 μm offset)	 Measured
Direct Transition	2.88	3.39	3.05
Horn Taper	0.50	0.54	0.8
Adiabatic (Love)	0.14	0.38	0.13
Adiabatic (Vassallo)	0.02	0.02	0.02

Device	Reflectivity Deep to Shallow etch (%) FDTD (ideal)	 FDTD (0.3 μm offset)	 Measured
Direct Transition	0.05	0.06	0.44
Horn Taper	0.04	0.06	0.36
Adiabatic (Love)	0.02	0.02	0.22
Adiabatic (Vassallo)	0.01	0.02	0.05

addition, the FDTD model used was a 2D approximation to the 3D system. The main reason for this reduction was that it was computationally prohibitive to run a 3D simulation on devices of the dimensions under consideration here. However, by imposing this restriction on the model the effects of scattering in the vertical direction are neglected, resulting in lower losses in the simulated results than would be the case for the 3D model. With these factors taken into account the matching between simulation and measured results is reasonable, though the disparity suggests that a role is played both by fabrication imperfections and vertical scattering.

It is at once obvious from both the simulated and fabricated device results that there is a significantly higher reflectivity in the transition from shallow to deeply etched waveguides, except in the case of the adiabatic (Vassallo) tapers. The mode travelling in the shallow etched section is less confined in the lateral direction and so when it impinges on the interface a larger proportion of that mode will see the index perturbation of the lower taper than would be the case in the opposite direction. However, in the case of the optimised tapers this effect is greatly reduced so that the tapers become almost symmetrically reflecting devices, exactly what is required in many applications. There is a brief concern here that the non-symmetric reflectivity somehow falls foul of reciprocity considerations. However, this is easily quashed, recalling that the loss is symmetric and it is not against reciprocity for the scattered radiation (in this case, that trapped by the backward travelling mode) to be non-symmetric.

There is excellent agreement between the FDTD and fabricated device results for the shallow to deep etch transitions giving confidence in the analysis of the latter and the TMM representation. Surprisingly the inclusion of the misalignment between taper layers does not appear to induce very large effects in the simulated losses of the devices, and only the direct transition shows any significant increase in reflectivity. There is however another factor to consider with regards to the transmission of the devices. It is important for many applications that light is not only not lost or reflected in these devices but that the transmitted light is maintained in the fundamental mode of the waveguide. In the case of the shallow etched guide this is achieved readily as the waveguide dimensions dictate single mode operation, however, the deeply etched guide is potentially multimoded and therefore analysis of the transmitted modes in the FDTD simulation results was carried out. To calculate the power in the fundamental mode, and hence the transmitted power carried in the higher order modes of the waveguide the mode cross section in the waveguide was sampled and the calculated fundametal mode profile subtracted to give the power in the higher order modes. Simulations were carried out with misalignment between the two taper structures of $0\,nm$, $150\,nm$ and $300\,nm$ ($300\,nm$ having been previously noted as an outside value that may occur during fabrication.) The transmitted power in the waveguide was analysed - in both the shallow to deep and deep to shallow etched configurations - to find the percentage of the transmitted power carried in higher order modes. It was found that in all of the taper designs, excluding the direct transition and the Adiabatic (Love) shallow to deep etch geometry, the variation in coupling to higher order modes is less than $2\,\%$ between extreme values of misalignment. Furthermore it was exhibited that the coupling into higher order modes was significantly larger in the shallow to deep transitions than the reverse propagation direction. This may be explained, as noted earlier, by the fact that the deep etch guide supports a number of transverse modes whereas the shallow etched guide is nominally single-moded, with power carried in higher order modes in this case describing the guided cladding modes of the mesa structure. Again the optimised Adiabatic (Vassallo) taper exhibits the most robust response with over $94\,\%$ of the transmitted power carried in the fundamental mode for all configurations considered. These results are summarised in Figure 6.16

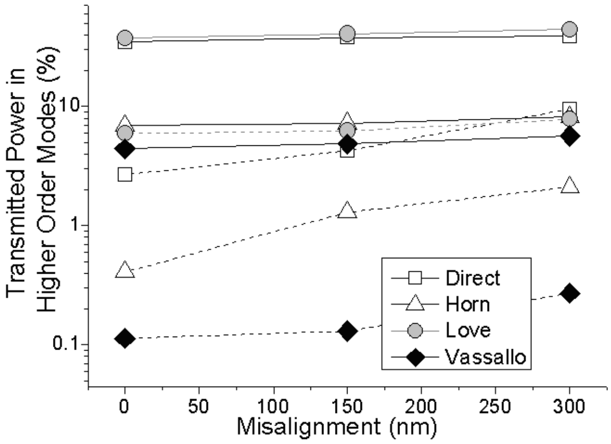

Figure 6.16: Power transmitted in higher order modes as function of misalignment between upper and lower tapers. Solid and dotted lines represent shallow to deep, and deep to shallow transitions respectively.

6.5 Conclusions

Double etched taper devices, were presented with particular attention paid to the taper profile in order to design short sub-100 μm devices. Two taper design schemes were outlined and the resulting tapers designed alongside control structures. FDTD simulations showed promising reflectivity characteristics that were matched by the low loss fabricated devices. In addition a TMM model of the experimental system provided confidence in the values extracted by experiment. The devices showed over a twofold reduction in loss and close to tenfold reduction in reflectivity compared with the direct transition, that along with their low loss, low modal conversion characteristics make them suitable for applications wide ranging in aspect.

Chapter 7

Conclusions

In this work it has been sought to investigate an integrated optical device solution for control of optical signal dispersion. After consideration of current technologies a tapered, deeply etched Bragg grating device was proposed. In the course of investigating the CBG device a number of issues were raised including fabrication techniques, waveguide loss reduction methods, modelling and design tools, measurement techniques and associated integrated devices for system integration. With recourse to the preceeding activities a chirped Bragg grating device was produced with high coupling coefficient characteristics and continuously variable Bragg condition. The grating was shown to operate well in two wavelength regimes - 980nm and 1550nm - with TE polarisation, so designed to correspond with semiconductor laser diode operaton, although TM operation is equally easy to implement. In addition to the flexible grating design other major outcomes were achieved in this work. A TMM model tool for the simulation of arbitrarily chirped and apodised grating devices was defined, the products of which consistently predicted the measured device characteristics. Wet chemical oxidation and fully post-growth grating and waveguide fabrication via HSQ based E-beam lithography and RIE were optimised to produce low loss, sub-micron structured, integrated optical devices. Double etched taper devices were designed and optimised to exhibit low reflectivity and loss transitions between deeply and shallow etched waveguide structures, allowing integration of devices based on both systems on one chip. The main results in these areas are summerised below.

7.1 Design and modelling of chirped, apodised Bragg gratings

For analysis of proposed chirped grating design, the well defined solution to the coupled-mode solutions pertaining to periodic structures was extended to include the effects of both Bragg condition variation and coupling coefficient with length. The effects of these variations were then described in terms of the delay profiles of the grating reflection characteristics and hence their dispersion modulation potential. The extended coupled-mode solutions were discretised for application as a TMM model of the grating system. With the available modulations in both λ_B and κ, arbitrary grating structures could be modelled, giving as outputs both transmitted and reflected fields, a useful situation given that later characterisation of the devices relied on both their reflection and transmission characteristics. The model was also analysed with respect to its discretisation dimensions, first by comparing the performance of the model against the direct solution to the coupled-mode equations for unchirped gratings, and then as an increasing function of discretisation length in both frequency and propagation length for arbitrarily chirped and apodised grating structures. It was shown that models with paramaters giving close approximation to analytic grating solutions could be easily simulated on a personal computer in a matter of minutes making this an attractive and flexible tool.

7.2 Deeply etched, tapered Bragg grating devices

With the grating design and predicted behaviour well defined by the coupled-mode TMM model, attention was paid to the physical design and fabrication of the devices. It was proposed that a tapered, deeply etched grating structure with constant longitudinal period would provide the features necessary for realisation of the intended devices. It was shown that the deeply etched sidewall gratings could provide high coupling coefficients due to the large overlap of the grating index modulation with the propagating mode cross-section and that the waveguide width taper could induce a significant change in effective index to modulate the Bragg condition as required. Work was carried out into fabrication of the grating patterns by E-beam lithography, both with PMMA and HSQ resists. It was found that not only did the HSQ fabrication method allow for fewer steps, but the patterns produced showed significantly less roughness after RIE etching than the associated PMMA/PECVD silica method. Further to the investigation between the two resists, work was carried out into wet chemical etching and oxide removal as a method by which the etched semiconductor sidewalls may be smoothed. Reductions in r.m.s. sidewall roughness and loss were observed up to $1.5\,nm$ and $4\,dBcm^{-1}$ respectively, although the as fabricated HSQ based devices still outperformed the treated PMMA/PECVD silica devices. The transmission spectra of fabricated gratings were measured for an array of devices with varying recess depth and facet conditions, with some AR coated and others left as cleaved. The results of these experiments illustrated two significant outcomes. Firstly, the gratings exhibited the predicted high coupling coefficients, close to $100\,cm^{-1}$ for a recess depth of only $200\,nm$ on a $2\,\mu m$ wide waveguide, showing that although there is an RIE lag effect of the pattern transfer into the deeply etched gratings, significant coupling may still be induced and furthermore κ may effectively be controlled by this method. Secondly these measurements highlighted the ability of a TMM model based curve-fitting algorithm to successfully supress the effects of the external cavity formed around the gratings by the access waveguides and device bar facets. The recovered transmission spectra of devices with one, two and no treated facets matched one another very well, in addition to closely following the spectra predicted by the TMM simulations of the grating devices. Given the relationships extracted from the first fabricated devices and the theoretical predictions, gratings with various chirp and apodisation profiles were designed, necessitating the careful design in concert of both the recess depth and waveguide width of the gratings. The transmission spectra of these devices matched very closely again with the simulations, exhibiting the effects of both grating chirp and apodisation together and in isolation. Non-linear variations and temporal pulse shaping devices were also fabricated and shown to closely follow the predicted stopband characteristics. In addition to the passive grating devices a secondary apodisation scheme was presented by way of DFB laser design and fabrication that allowed for variation of the grating coupling coefficient as a function of wavelength without recourse to modulation of the grating recess depth. The fabricated DFB lasing characteristics were multimoded and again predicted by the TMM model, showing clearly that the designed variations in both Bragg condition and coupling coefficient may be well controlled, and that the gratings are low loss enough, even when deeply etched, to allow lasing of the DFB devices. Finally, an integrated Michelson interferometer device was presented in order to measure the phase characteristics of the grating in reflection. Again the TMM model allowed simulation of this device structure and the devices fabricated within it closely agreed with the simulated outcomes. This not only allows further confirmation of the quality of the fabricated grating devices but also clearly illustrates the potential of the integrated Michelson in on chip interferometric applications.

7.3 Adiabatic deep to shallow etch transitions

As the grating devices presented in this thesis are based around deeply etched waveguide structures - a technology also useful for tight waveguide bends and high frequency components - and many integrated devices are implemented in shallow etched geometries it was identified that a low loss, and low reflectivity transition between the two would be extremely beneficial. To this end a double etched tapered transistion was identified and the taper profile designed using approximations to adiabatic criteria for sub-100 μm long devices. These tapers were fabricated using the optimised E-beam lithography and RIE processes already developed for the gratings and their properties measured using a transmission measurement that, by curve-fitting to a similar model as developed for the grating parameter extraction, may recover both the loss and reflectivity characteristics. The optimised devices were compared both against FDTD simulations and other taper geometries and shown to give a two-fold reduction in loss and ten-fold reduction in reflectivity over a direct transition. In addition, analysis of the FDTD simulations was carried out to predict the effect of misalignment of the taper layers on their performance and specifically with regards to coupling into higher order modes. The optimised tapers were found to couple very weakly into the higher order modes of the waveguides and remained relatively immune to misalignment of the layers up the maximum predicted fabrication offset likely of 300 nm.

7.4 Future Work

In this work the design, modelling, fabrication and measurement of flexible grating devices have been presented. Transmission and reflection measurements and loss reduction techniques have been investigated as well as the proposal of deep to shallow etch transitions by which the deeply etched gratings may be integrated with wider optical circuits. The success of these activities suggest new directions in which research may be pursued to apply the results obtained here.

Firstly, although gratings that may present arbitrarily variable λ_B and κ profiles have been illustrated, the manner by which these variations may be generated has not been dealt with fully. Normally the Bragg condition profile and coupling coefficient are not immediatly available but are implied in the required reflectivity and grating phase characteristics. As was described in Chapter 2 both the grating reflectivity and phase characteristics are dependent on both κ and λ_B. Therefore it is not a straightforward matter to extract these parameters from the desired outcomes, but requires solution of the coupled parameter problem. Once this has been tackled then in addition to the methods presented here, a very powerful method will be available for application with many existing problems.

Although the gratings presented here may be fabricated fully post-growth, and with controllable chirp and apodisation, where many other methods cannot, there is one aspect in which they have room for improvement. The bandwidths exhibited here are in the order of nanometers, as opposed to some linearly chirped, constant κ gratings fabricated by sampled grating or phase-shifted grating approximations that can show tens of nanometers bandwidth. One way in which this may be remedied, whilst still avoiding the necessity to locally vary the grating longitudinal period that was deemed a difficult method to pursue, is to combine the continuously varying chirped approach of the tapered waveguide with the sampled grating method. In this case long sections of grating with constant longitudinal period - that varies between them - may be written, and internal to these the Bragg condition may be varied as proposed in this work. In this way larger bandwidths might be achieved whilst still retaining all of the benefits of the methods outlined here.

It was illustrated that gratings may be fabricated with functions of chirp or apodisation isolated from one another. The ability to fabricate single Bragg condition gratings with arbitrarily modulated apodisation profiles for pulse shaping applications has already been exhibited in fibres [116]. With the technology presented here, this is an area that may be investigated in integrated devices, opening up a whole new pulse-width regime. To this end a colloboration has already begun with José Aza*ñ*a of INRS, Montréal, the initial results of which were presented in Chapter 4.

Finally, the building blocks for a fully integrated pulse dispersion control and ultrashort pulse generation system have been investigated and optimised here. So, the next logical step it seems would be to construct integrated mode-locked lasers with chirped, apodised DBR mirrors, with the two laser sections interfaced with the deep to shallow etch transitions. These devices may then be explored with regards to pulse modulation at generation, and compensation of the inherent chirping of ultrashort pulses in semiconductor MLLs.

Hopefully, there are other applications for the structures and processes described in this thesis that are so far outwith the knowledge of the author but may provide useful employment of these writings.

Appendix A

Coupled-Mode Theory

As stated in section 2.1 the case of two orthogonal, counter propagating modes in a waveguide with periodically varying index may be considered through coupled-mode theory. Firstly in a qualitative sense the amplitudes of the forward and backward propagating waves may be described when considering a grating of finite length, and initial excitation from only the forward propagating component. From Figure A.1 it is clear that the amplitude of the backward propagating mode is zero at the full length of the grating, increasing with coupling from the forward mode backwards along the grating length. Quantatively the analysis of the fields is based on the time independent wave equation.

$$\nabla^2\mathbf{E} + \epsilon(x, y, z)k_0^2\mathbf{E} = 0 \tag{A.1}$$

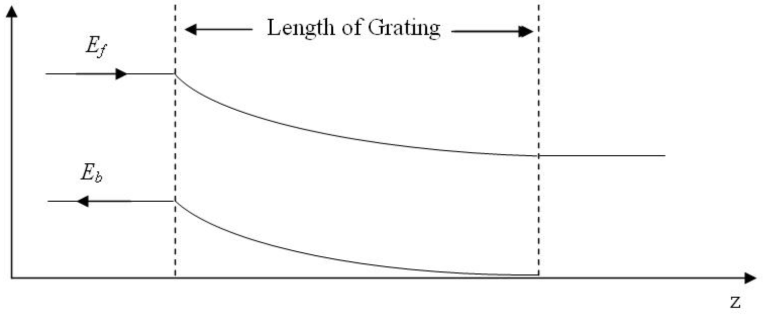

Figure A.1: Evolution of forward and backward mode amplitudes along a finite length Bragg grating.

Where **E** is the electric field, k_0 is the free space wavenumber and $\epsilon(x, y, z)$ is the permittivity of the media the fields are present in. The permittivity in the case of a grating may be written as a periodic modulation in z, superimposed on an average permittivity distribution in x and y.

$$\epsilon(x, y, z) = \bar{\epsilon}(x, y) + \Delta\epsilon(x, y, z). \tag{A.2}$$

The total electric field at any point in the grating region may be written as:

$$E(x, y, z) = \hat{x}U(x, y, z)\left[E_f \exp[(g - j\beta)z] + E_b \exp[(g + j\beta)z]\right]. \tag{A.3}$$

Where E_f and E_b are the complex amplitudes of the forward and backward propagating waves respectively β is their associated propagation constant, $U(x, y, z)$ is the slowly varying complex amplitude and $\hat{x}$ is the directional unit vector of the electric field. It can be assumed that there is negligible variation of $U(x, y, z)$ along the z direction - therefore it can be reduced to a variation in only the x and y directions, $U(x, y)$ - and that the functions E_f and E_b are also slowly varying, greatly simplifying the analysis. The resultant time independent wave function may be multiplied by $U(x, y)$ and integrated over x and y, giving:

$$\frac{dE_f}{dz}\exp[(g-j\beta)z]+\frac{(g+j\beta)}{(g-j\beta)}\frac{dE_b}{dz}\exp[(g+j\beta)z] = \frac{-jk_0^2}{2j(g-j\beta)V}\iint \Delta\epsilon(x, y, z)U^2(x, y)$$
$$\times\left[E_f \exp[(g - j\beta)z] + E_f \exp[(g + j\beta)z\right] dxdy. \tag{A.4}$$

Where V is a normalisation constant of

$$\iint U^2(x, y)dxdy.$$

As stated previously $\Delta\epsilon(x, y, z)$ is periodic in the z direction and can therefore be expanded as a Fourier series to:

$$\Delta\epsilon(x, y, z) = \sum_{l\neq 0} \Delta\epsilon_l(x, y) \exp(-j\frac{2\pi}{\Lambda_0}lz). \tag{A.5}$$

Replacing (A.5) into (A.4) gives an expression of the rate of change of forward and backward propagating modes in terms of the lateral modal and permittivity

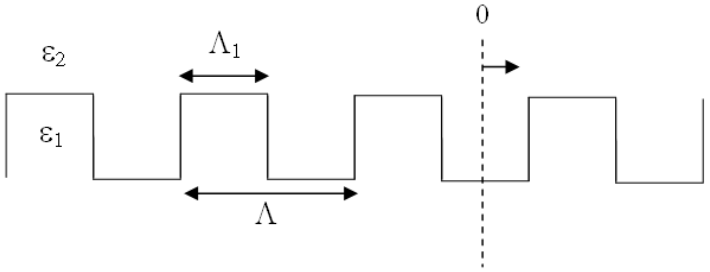

Figure A.2: Schematic of refractive index perturbation in a waveguiding structure

profiles and the longitudinal permittivity perturbation.

$$\frac{dE_f}{dz}\exp[(g-j\beta)z]+\frac{(g+j\beta)}{(g-j\beta)}\frac{dE_b}{dz}\exp[(g+j\beta)z]=$$
$$\frac{-jk_0^2}{2j(g-j\beta)V}\iint\sum_{l\neq 0}\Delta\epsilon_l(x,y)\exp(-j\frac{2\pi}{\Lambda}lz)\;U^2(x,y)$$
$$\times\;[E_f\exp[(g-j\beta)z]+E_f\exp[(g+j\beta)z]\;dxdy \quad \text{(A.6)}$$

It is useful at this point to consider the coupling coefficient of the system, this is the factor describing the effect of the perturbation on the modes of the grating. From (A.6) the coupling coefficient κ can be expressed as:

$$\kappa=\frac{k_0^2}{2j(g-j\beta)}\frac{\iint\sum_{l\neq 0}\Delta\epsilon_l(x,y)\exp(-j\frac{2\pi}{\Lambda}lz)\;U^2(x,y)\;dxdy}{\iint U^2(x,y)\;dxdy}. \quad \text{(A.7)}$$

A further simplification can be made by assuming that the index perturbation is of rectangular profile and of known duty-cycle as shown in Figure A.2. Further to the previous statements it is also assumed that the perturbation of permittivity is real. Therefore the perturbation may be solved for by integrating over one period of the grating. Using the origin given in Figure A.2 the integration may be carried out as outlined below.

$$\int\Delta\epsilon_l(x,y)\exp\left[-j\frac{2\pi}{\Lambda}lz\right]\;dz$$
$$\Rightarrow\frac{1}{\Lambda}\left\{\int_{-\frac{\Lambda_1}{2}}^{\frac{\Lambda_1}{2}}|\Delta\epsilon_l(x,y)|\cos\left(\frac{2\pi z}{\Lambda}\right)\;dz+\int_{\frac{\Lambda_1}{2}}^{\Lambda-\frac{\Lambda_1}{2}}|\Delta\epsilon_l(x,y)|\cos\left(\frac{2\pi z}{\Lambda}\right)\;dz\right\}$$

$|\Delta\epsilon|$ is taken as the difference of the permittivities $\epsilon(z)$ and ϵ_1 and so the second part of the integral is forced to zero.

$$\begin{aligned}
\frac{|\Delta\epsilon_l(x,y)|}{\Lambda}\int_{-\frac{\Lambda_1}{2}}^{\frac{\Lambda_1}{2}}\cos\left(\frac{2\pi lz}{\Lambda}\right)\,dz &= \frac{|\Delta\epsilon_l(x,y)|}{\Lambda}\left[\sin\left(\frac{2\pi}{\Lambda}lz\right)\cdot\frac{\Lambda}{2\pi l}\right]_{-\frac{\Lambda_1}{2}}^{\frac{\Lambda_1}{2}} \\
&= \frac{|\Delta\epsilon_l(x,y)|l}{2\pi}\left[\sin\left(\frac{2\pi l}{\Lambda}\frac{l\Lambda_1}{2}\right)-\sin\left(\frac{2\pi l}{\Lambda}\frac{-l\Lambda_1}{2}\right)\right] \\
&= \frac{|\Delta\epsilon_l(x,y)|l}{2\pi}\left[2\sin\left(\frac{\pi l\Lambda_1}{\Lambda}\right)\right] \\
&= \frac{|\Delta\epsilon_l(x,y)|l\sin\left(\frac{\pi l\Lambda_1}{\Lambda}\right)}{\pi}
\end{aligned} \tag{A.8}$$

It is clear that in the case where $l = 1$, in other words a first order Bragg grating response, and where the duty cycle is equal to 50%, (A.8) simplifies to $\frac{|\Delta\epsilon_l(x,y)|}{\pi}$. Replacing the first order response into (A.7) the coupling coefficient may be written as:

$$\kappa = \frac{k_0^2}{2j(g-j\beta)}\frac{(n_2^2-n_1^2)\Gamma_{x,y}}{\pi}. \tag{A.9}$$

Or, with some substitution, and assuming zero gain:

$$\kappa = \frac{(n_2^2-n_1^2)\Gamma_{x,y}}{2n_{eff}^2\Lambda_0}. \tag{A.10}$$

Where n_{eff} is the effective refractive index of the mode. With (A.10) and (A.6), the coupled mode equations may be derived by equating the coefficients of $exp(g \mp j\beta z)$ and retaining only the approximately phase matched-terms. Furthermore the electric field may be written in terms of the Bragg condition of the grating.

$$E(z) = A(z)\exp[-j\beta_0 z] + B(z)\exp[j\beta_0 z] \tag{A.11}$$

Where

$$A = E_f\exp[(g-j\Delta\beta)z] \quad \text{and} \quad B = E_b\exp[(g+j\Delta\beta)z]. \tag{A.12}$$

The coupled-mode equations of the system may be written in terms of A and B.

$$\frac{dA}{dz} = (g - j\Delta\beta)A + j\kappa B \tag{A.13}$$

$$-\frac{dB}{dz} = (g - j\Delta\beta)B + j\kappa A \tag{A.14}$$

Given the coupled differential equations (A.13) and (A.14), they may be solved by first assuming a general form of solutions given by (A.15) and (A.16).

$$A(z) = A_1 e^{-jqz} + A_2 e^{jqz} \tag{A.15}$$

$$B(z) = B_1 e^{-jqz} + B_2 e^{jqz} \tag{A.16}$$

Where $A_{1,2}$ and $B_{1,2}$ are interdependent constants, and q is the complex propagation coefficient of the solution. If q is purely real then there is no coupling between the waves and they would propagate as an orthogonal superposition. However, if q has some imaginary component, then there is an exponential term with respect to z introduced, so that there is power transfer between the forward and backward travelling waves. Replacing (A.15) and (A.16) into (A.13) and equating the coefficients of e^{jqz}, q can be expressed as (A.17).

$$q^2 = (jg + \Delta\beta)^2 - \kappa^2 \tag{A.17}$$

If the material gain constant is set to zero then the complex propagation constant through the grating becomes that of a passive grating structure $q^2 = \Delta\beta^2 - \kappa^2$. Further to the propagation constant, the reflection coefficient $r(q)$ is required to solve for the forward and backward components of the wave as (A.15) and (A.16) may be rewritten to show the interdependence of the coefficients.

$$A(z) = A_1 e^{-jqz} + r(q) B_2 e^{jqz} \tag{A.18}$$

$$B(z) = B_2 e^{jqz} + r(q) A_1 e^{-jqz} \tag{A.19}$$

(A.18) and (A.19) may be substituted into (A.14).

$$-\frac{dB}{dz} = (g - j\Delta\beta)\left[B_2 e^{jqz} + r(q)A_1 e^{-jqz}\right] + j\kappa\left[A_1 e^{-jqz} + r(q)B_2 e^{jqz}\right]$$
$$-\frac{dB}{dz} = jqB_1 e^{-jqz} - jqB_2 e^{jqz}$$

Equating the coefficients of e^{jqz}:

$$\begin{aligned}(g - j\Delta\beta)B_2 + j\kappa r(q)B_2 e^{jqz} &= -jqB_2 \\ &\Rightarrow \\ r(q) &= \frac{(jg + \Delta\beta) - q}{\kappa}\end{aligned} \tag{A.20}$$

Again, if the material gain coefficient is set to zero, then the reflection coefficient is equal to that found for a passive grating structure.

To calculate the reflection of a finite length of grating, boundary conditions must be imposed. Obviously for excitation by the forward travelling mode only, $B(L_g) = 0$, where L_g is the length of the grating.

$$\begin{aligned}A(0) &= A_1 + r(q)B_2 \\ B(0) &= B_2 + r(q)A_1\end{aligned}$$

$$\begin{aligned}B(z = L_g) &= B_2 e^{jqL_g} + r(q)A_1 e^{-jqL_g} = 0 \\ B_2 &= -r(q)A_1 e^(2jqL_g)\end{aligned}$$

so

$$\begin{aligned}r_g &= \frac{B(0)}{A(0)} = \frac{A_1 + r(q)B_2}{A_1 + r(q)B_2} \\ r_g &= \frac{r(q)\left[1 - e^{-2jqL_g}\right]}{1 - r^2(q)e^-2jqL_g}\end{aligned}$$

Appendix B

Hydrogen Passivation of Free Carriers

As mentioned in section 3.3.4 a strong source of losses in doped semiconductor devices is that derived from free carrier absorption. It is desirable to reduce these losses in the inactive sections of an integrated optical device and one method of doing so is by hydrogen passivation of the dopants.

B.1 Theory

B.1.1 Lattice charge distribution and effects of doping

The dopants in III-V semiconductors provide a mechanism for free carrier creation in the lattice. As the common epilayer structure of laser devices has the p doped cladding uppermost it is this layer that may be most easily accessed in passivation experiments. However, as will be discussed later the following theory is easily modified to deal with n type material. A common dopant used to create free holes in InP is zinc. Zinc is a group II metal, and therefore when placed on a group III lattice site creates a vacancy in the normally filled valence band. Figure B.1 is a simplified diagram of a group III lattice site; the structure of the crystal is tetrahedral but is shown as a two dimensional square here for simplicity. Figure B.1(a) is a schematic of the group III lattice site with indium fully coordinated with the surrounding phosphorus atoms. Figure B.1(b) shows zinc doping at a group III site and the resultant dangling bond from one of the surrounding phosphorus species. The dotted lines in Figure B.1 represent covalent bonds, the

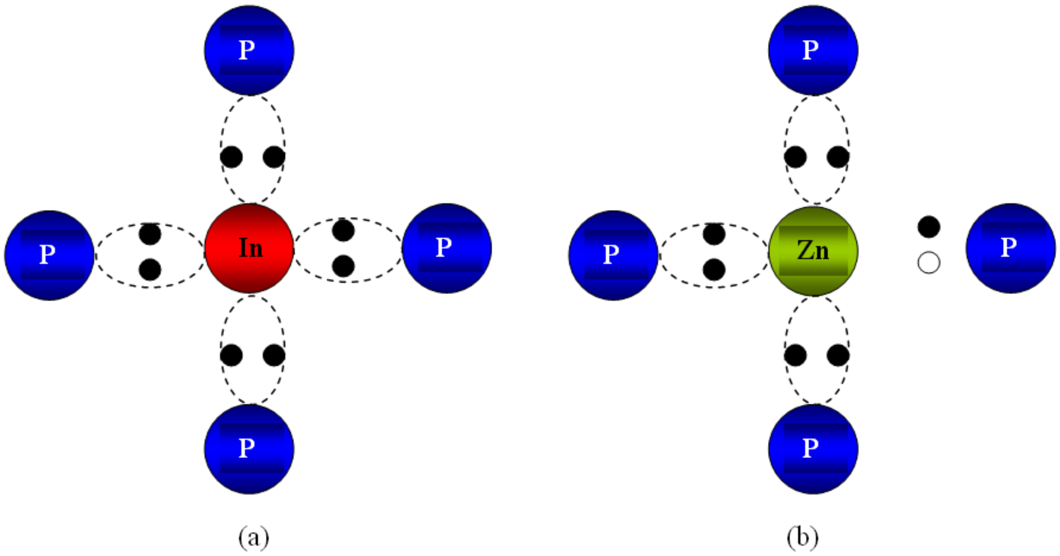

Figure B.1: Lattice site in a III-V InP lattice (a), and at a Zn doped site in a InP lattice.

filled circles are valence electrons and the empty circles are vacant states. In the InP lattice all four covalent bonds consist of two shared electrons, three provided by the In atom and five by the P atom. The valence band of the lattice has a full complement of eight electrons. However, in the case of the Zn doped site the zinc atom only contributes two valence electrons to the lattice, resulting in a dangling bond on the nearest P atom. The lattice, consequently, does not have a full valence band of electrons; an empty state being the potential to form a bond between the P atom with the dangling bond and the Zn. An acceptor energy level corresponding to the valence band to acceptor bond transition is now apparent in the band structure of the semiconductor. The vacant space in the valence band is generally referred to as a hole. The hole constitutes a free carrier in the p doped material and as such may play a part in inter-valence band absorption (IVBA).

In a semiconductor lattice in the absence of doping, the electrons may occupy states in the valence or conduction bands. At thermal equilibrium at room temperature, electrons in the semiconductor lattice occupy the valence and conduction bands in proportions governed by the Fermi distribution of the material. The electrons and holes, in the conduction and valence bands respectively, constitute the free carriers of the semiconductor. The numbers of these carriers are typically low under normal conditions [3]. As discussed above, by introducing a group II

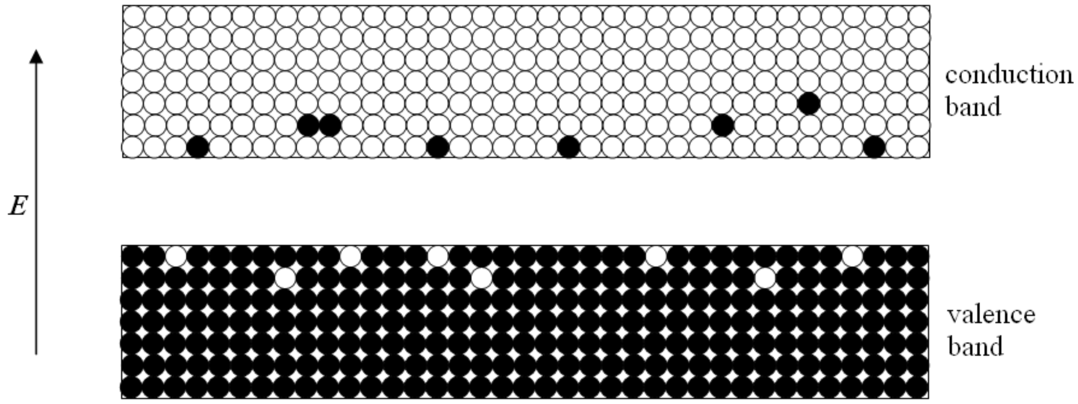

Figure B.2: Semiconductor valence and conduction bands under thermal equilibrium.

impurity to the lattice an acceptor energy level is introduced that exists just above the top of the valence band. The electrons in the valence band are therefore easily exited into this acceptor state, leaving holes in the valence band that can act as free carriers. The density of holes created in the valence band is then proportional

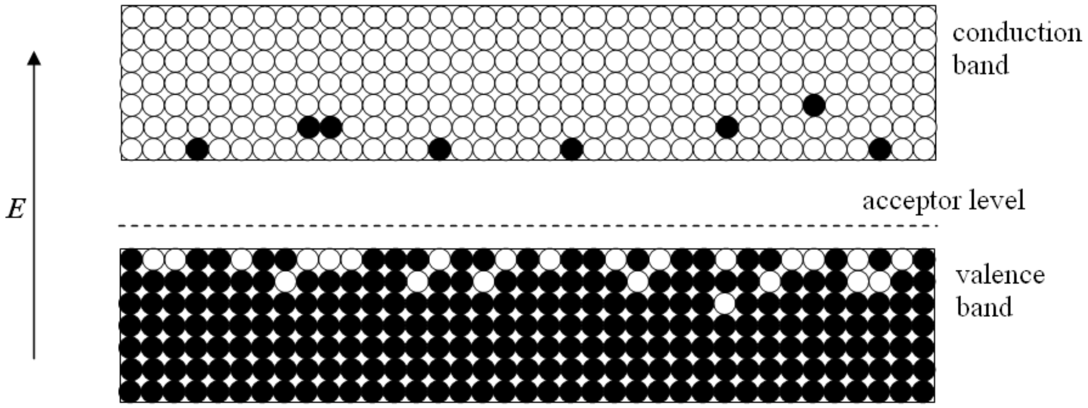

Figure B.3: Energy diagram of semiconductor with acceptor type doping.

to that of the dopant sites, typically $1 \times 10^{18} cm^{-3}$ for p type InP.

B.1.2 Hydrogen diffusion into active materials

One method proposed in the literature to suppress the effects of free carrier absorption is that of hydrogen passivation by plasma diffusion [52, 66, 70–72, 75, 79, 81, 117, 118]. The sample is placed in hydrogen plasma where the H^+ ions diffuse into the material, the inbuilt electric field - due to the acceptor impurities - causing the ions to penetrate deeply into the lattice. The H^+ ions are attracted to the negatively charged dopant sites in the *p* doped material; there they form complexes, with an overall neutral charge. The mechanism involved in this passivation also annihilates the free hole, resulting in the electrical neutralisation of the site. Initially the bond between adjacent P and Zn atoms is broken to leave two dangling bonds. The hydrogen then attaches to the phosphorus atom and the dangling bond on the zinc atom combines with the free hole such that the zinc is tri-coordinated with surrounding phosphorus atoms. This process is shown in Figure B.4. Over 90% passivation of dopant sites in zinc doped InP has been achieved by plasma diffusion hydrogen passivation [118] resulting in a large difference in losses due to IVBA. Free carrier absorption losses may be characterised as given in (B.1).

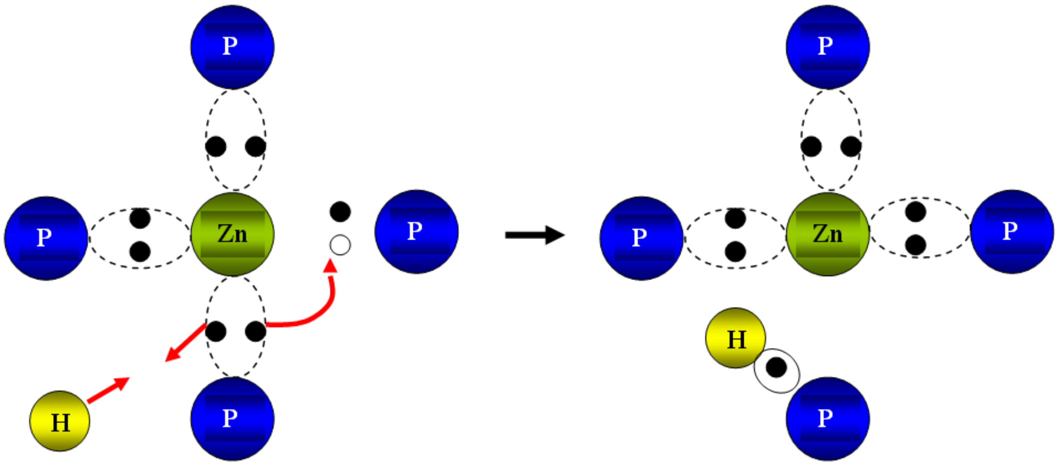

Figure B.4: Hydrogen complex at a Zn doped InP lattice site.

$$\alpha_{fc} = \frac{N_c e^3 \lambda^2}{4\pi^2 n (m^*)^2 \mu \epsilon_0 c^3} \tag{B.1}$$

Where α_{fc} is the free carrier absorption coefficient, N_c is the number of free carriers, λ is the incident wavelength of radiation being absorbed, n is the refractive index of the material, m^* is the effective mass of the carrier and μ is the carrier mobility. Clearly the free carrier absorption is proportional to the number of carriers present, and as a large proportion of these are neutralised with hydrogen passivation, the losses associated with IVBA should also decrease by significant fractions. It is also worth noting that the passivation of the dopant sites results in a neutral local charge, as opposed to the local negative charge of a group II atom on a group III lattice site. The negative charge on the unpassivated dopant site results in reduced carrier mobility - when the charged dopant sites are the limiting factor - and therefore by neutralising the sites the Couloumbic effect on carrier mobility is removed, leading to higher carrier mobility and a reduction in the free carrier loss coefficient. The reduction due to increased carrier mobility is however, an order of magnitude less than that due to the reduced free carrier population.

In n type material the dopant, often Si, creates a donor state in the lattice. At donor sites the valance band is full but an extra electron is donated by the dopant species. Hydrogen passivation at these sites is very similar to that in p type material. A hydrogen ion attaches to the dangling bond of the donor atom trapping the donor state and preventing free carrier absorption at that site.

B.2 Experimental Results

The material used in this work is a MQW structure based on InAlGaAs, on an InP substrate. A schematic of the material structure is given in Figure B.5. The literature presents a wide range of parameters for the hydrogen diffusion process [52,66,70–72,79,81]. Either hydrogen or deuterium (an isotope of hydrogen with an additional neutron) is used and the range of temperatures and pressures of the plasma vary greatly. The objective is constant however, to ensure the process is diffusion limited rather than a physical etching of the material. The literature also shows a predomination of RIE based processes with only the Bristol group notably using an inductively coupled plasma (ICP) process. The initial work presented here is based on RIE techniques and aimed to cover the range of working conditions presented in the literature. The parameters taken from other works are given in

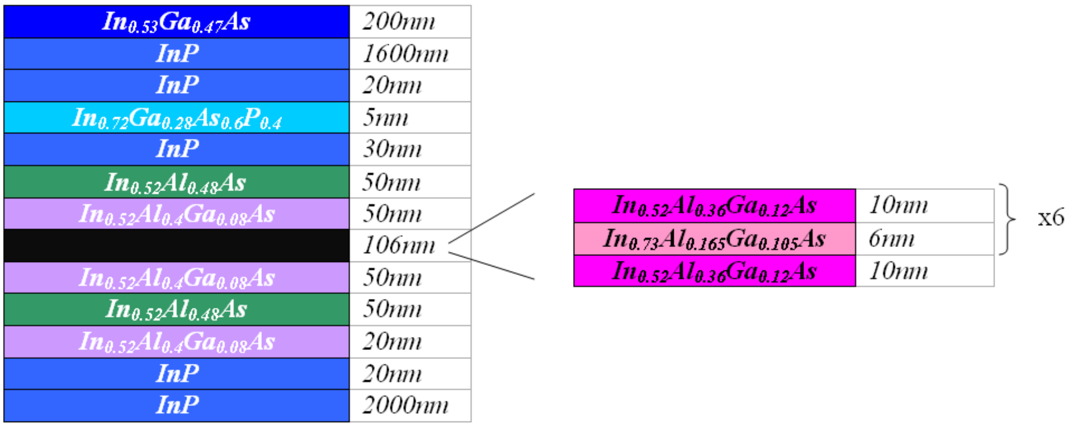

Figure B.5: Material structure of MBE 3177.

table B.1. Where the flow rate is given in standard cubic centimetres per minute (sccm).

Table B.1: Parameters for hydrogen passivation from literature.

Group	Chevaillier	Intense (Marsh)	Bristol	Glasgow Uni
Gas	Deuterium	H_2	H_2	H_2
Pressure $(mTorr)$	-	$75-750$	8	$50-200$
Flow rate $(sccm)$	-	-	50	50
Source Power (W)	-	-	1000	-
RF Power (W)	60	280	25	$34-300$
Temp (^oC)	163	200	170	Ambient -200
Time (min)	Up to 120	Up to 120	Up to 120	$10-60$

B.2.1 RIE based processes

The first experimental setup used was the System100 RIE machine. The InP sample was previously patterned with shallow etched ridge waveguides of $2\mu m$ width to allow loss testing after the passivation run. A schematic of the chamber is presented in Figure B.6. The pressure in the chamber is controlled by the inlet and outlet valves, the high pressures required in these experiments necessitating an almost fully shut outlet valve. In the first experiment the process was carried out at ambient temperature. The full process parameters are given in table B.2. The operating conditions lie well within the boundaries of those presented by other

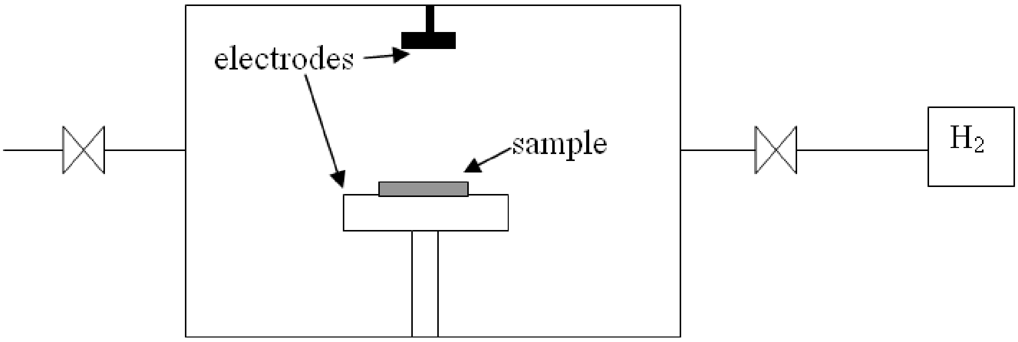

Figure B.6: Schematic of the System100 RIE setup.

Table B.2: Passivation parameters using the System100 at high pressure and power.

Machine	System100
Forward RF power	$300W$
Process time	$30min$
Process temperature	200^oC
Process pressure	$200mTorr$

groups, however the results did not match with those presented elsewhere. Figure B.7 shows SEM images of the $2\mu m$ waveguides after the passivation attempt. From Figure B.7 it is clear the waveguides have been destroyed by the process. It is possible that the high pressure and temperature of the process caused mass transport of the InP resulting in the flattened waveguides apparent. To test this theory the next sample was processed in the ET340 machine at lower pressure, power and temperature. The parameters are given in table B.3.

Table B.3: Passivation parameters using the ET340 RIE machine.

Machine	ET340
Forward RF power	$150W$
Process time	$30min$
Process temperature	Ambient
Process pressure	$100mTorr$

Figure B.8 shows the SEM images of the waveguides after the process given in table B.3. From Figure B.8 it is clear that the reduction in pressure, power and temperature of the process has prevented the mass transport of the InP in the upper-cladding. The waveguides appear undamaged apart from the roughness on the facet. As the InGaAs cap and MQW layers are unaffected by the roughness it was postulated that this effect was caused by the liberation of phosphorus from the InP surface by its reaction with hydrogen to form PH_3, leaving deposits of indium behind. The sample was cleaved to remove the rough surfaces and loss measurements carried out. However there was no significant difference in the loss figure from that of the as-fabricated sample, suggesting that the hydrogen had not penetrated into the material deeply, its effects limited to the surface liberation of phosphorus.

A $200nm$ layer of PECVD silica was deposited on top of the InP as-fabricated waveguide structures to act as a barrier to the liberation of P from the sample, and as protection from the possible physical etching effects of the plasma. The process parameters were kept as detailed in table B.2 in an attempt to promote deep diffusion of the H^+ species into the lattice. Figure B.9 shows SEM images of the sample after the passivation process. Clearly the layer of PECVD silica acts as a barrier to the liberation of phosphorus from the material. Figure B.9 shows

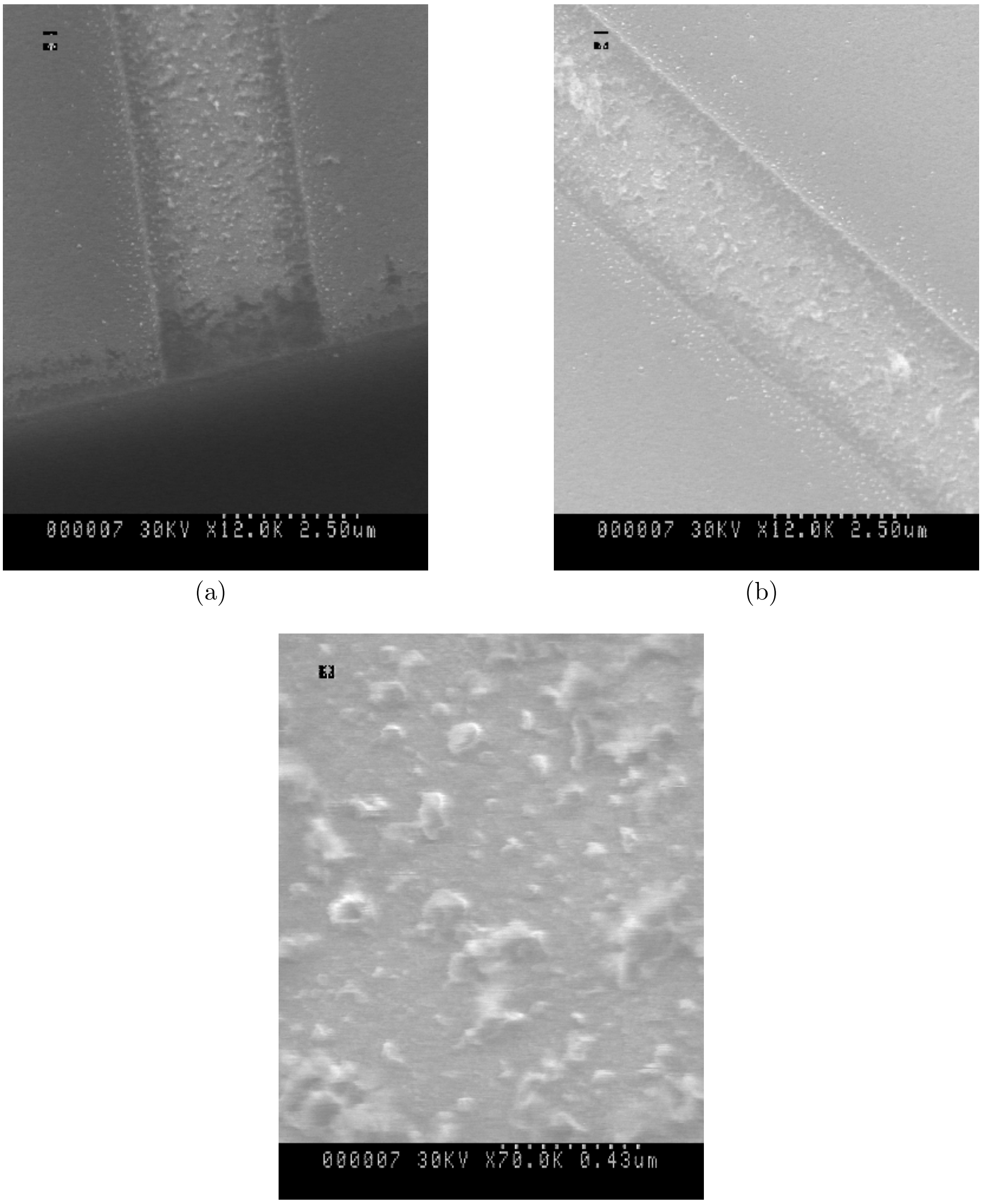

(a) (b)

(c)

Figure B.7: Waveguide on InP after H^+ passivation in System100 at high power and pressure.

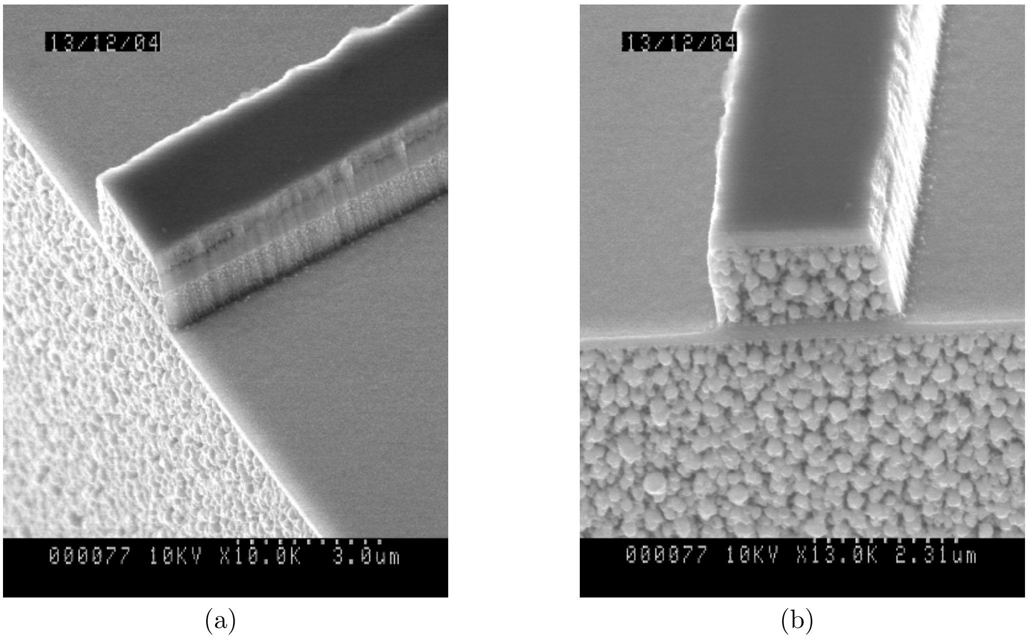

(a) (b)

Figure B.8: Facet of InP waveguide after H^+ plasma in the ET340.

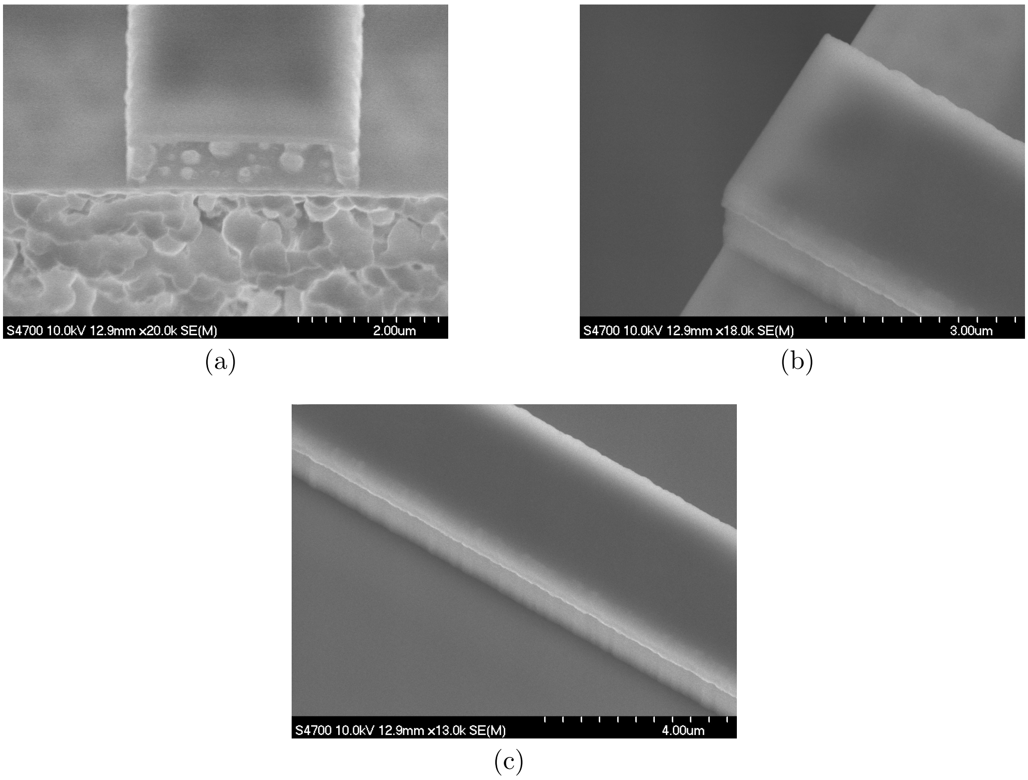

(a) (b) (c)

Figure B.9: Waveguide on InP after H^+ passivation in System100 with PECVD silica cap.

that on the facet the InP is attacked but the PECVD layer is left undisturbed. The guiding MQW layer is also damaged in this case, which was not so in the low temperature and pressure process. Loss measurements before and after the passivation process showed that the PECVD cap not only physically protected the waveguide but also blocked the diffusion of hydrogen into the material so that the waveguide losses were not significantly affected by the process.

In all previous processes the waveguide structure was defined initially and then the hydrogen passivation was carried out. The literature suggested that an InGaAs cap layer should act as a protective barrier against the liberation of the phosphorus from the sample[1, 3-6] whilst still allowing diffusion of the hydrogen ions into the semiconductor lattice. To this end it was decided to passivate the material prior to waveguide definition, thus having no open InP surfaces other than the facets during passivation. The first run was undertaken using the parameters detailed previously in table B.2. Figure B.10 shows the surface of the material after the process. It appears from Figure B.10 that InGaAs cap layer had no beneficial effect on the process, with the surface showing the familiar pattern of indium droplets. The process was then modified to lower power and pressure levels in an attempt to prevent the physical etching of the material. The parameters for this process are given in table B.4.

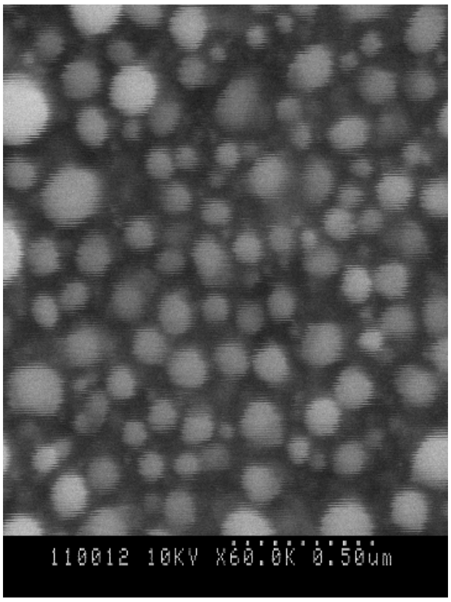

Figure B.10: Surface of sample after passivation in System100 machine.

Figure B.11 shows the effects of the process detailed in table B.4. Again,

Table B.4: Passivation parameters using the System100 at low pressure and power.

Machine	System100
Forward RF power	$34W$
Process time	$30min$
Process temperature	200^oC
Process pressure	$75mTorr$

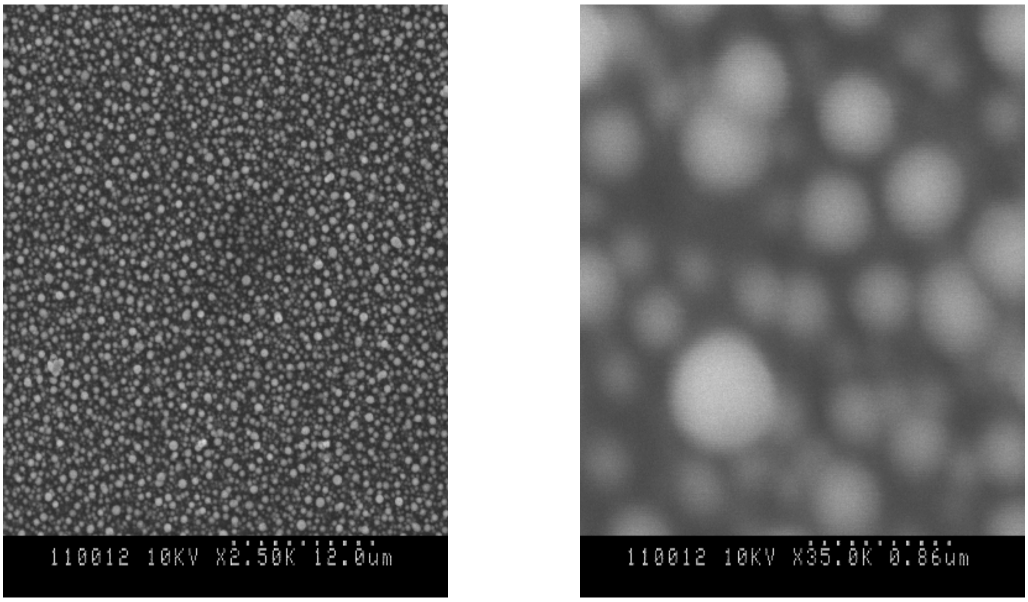

(a) (b)

Figure B.11: Surface of sample after low power and pressure passivation in System100.

although the power and pressure were greatly reduced, the plasma has physically etched through the InGaAs layer and left a layer of indium droplets on the surface of the sample. A cross section of the sample was viewed with the SEM as shown in B.12. The right hand side of the image shows the sample coated with a 200*nm* layer of PECVD silica and photo-resist. The left hand side is the bare sample after H_2 passivation. Clearly the hydrogen has almost etched completely through the upper cladding, with the indium droplets plainly visible. In order to ensure that only the InGaAs cap was exposed to the plasma and no side etching of the InP was leading to the erosion of the waveguides, a layer of silica was deposited onto the waveguides and windows opened on their top surface. The windowing process provided a protective silica layer on the exposed InP surfaces constituting the waveguide sidewalls, leaving only the InGaAs cap exposed to the hydrogen plasma.

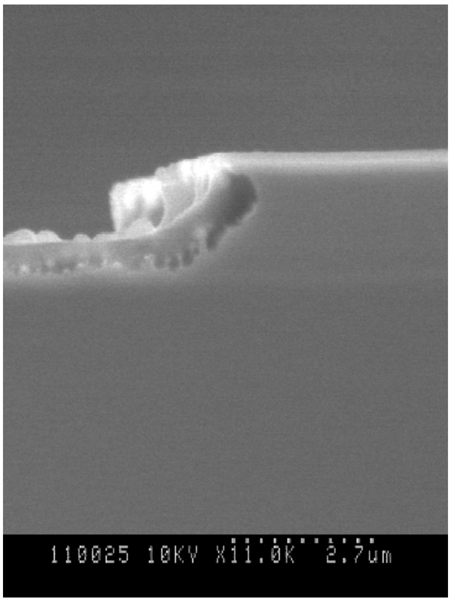

Figure B.12: Section of InP material after hydrogenation.

Again the InGaAs cap layer was etched through leaving the indium droplets on the material surface. Figure B.13 shows a waveguide with its sidewalls and surrounding trench protected with PECVD silica.

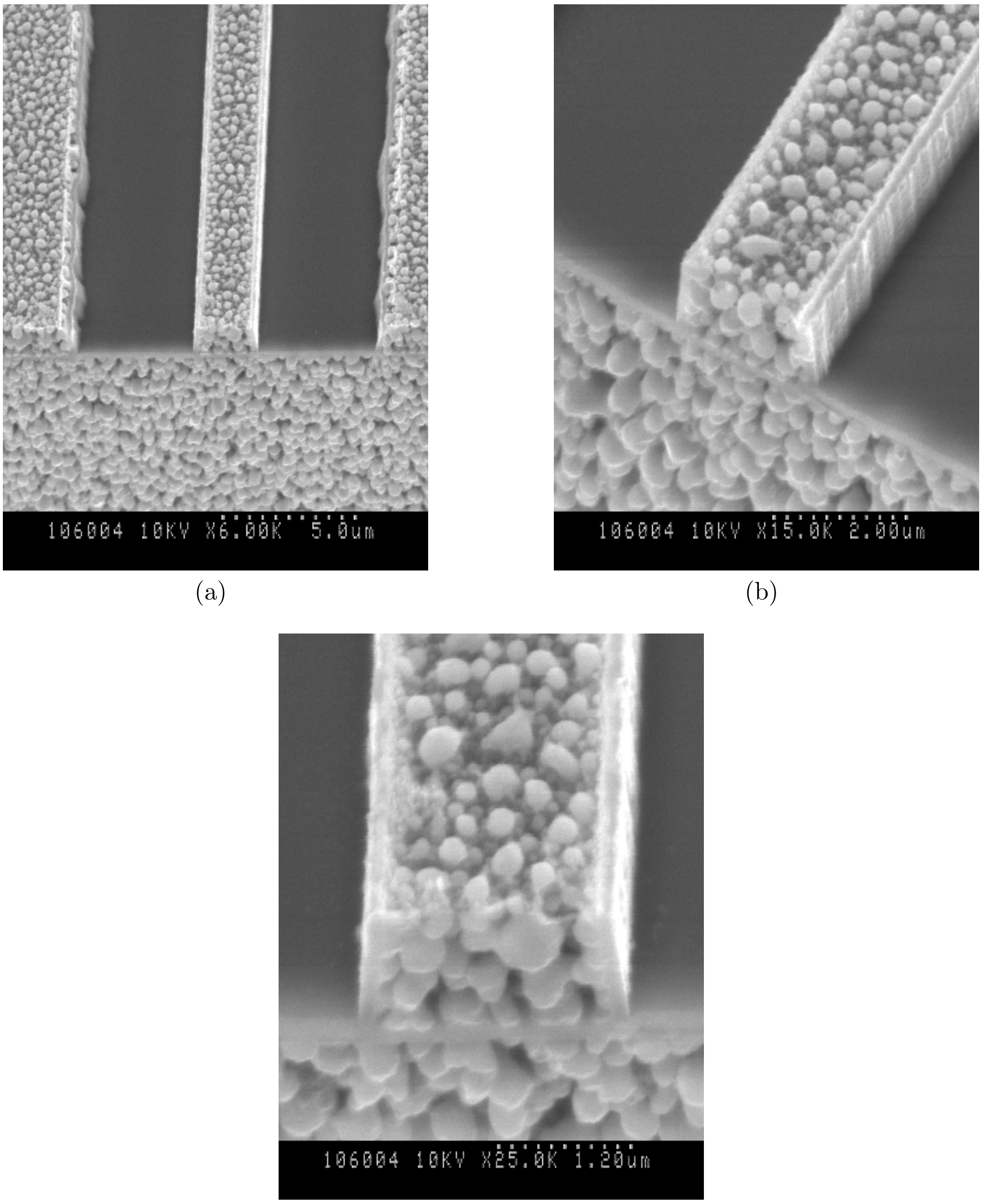

(a) (b)

(c)

Figure B.13: Waveguide with SiO_2 protected sidewalls and trench after RIE hydrogenation.

B.2.2 ICP processes

The RIE processes described suffer from the fact that the power required to create the plasma is also applied across the sample in the chamber, meaning that a relatively high bias voltage is also exhibited across the sample. A high voltage across the sample can possibly lead to the physical etching of the InGaAs cap layer and rapid liberation of phosphorus noted in the ET340 processes. To combat this problem a process based on an ICP machine was sought. The major benefit of this technique is that a high power is used to create the plasma in one chamber which is then transferred to the sample chamber where a relatively low power may be used, reducing the bias voltage across the sample. The experimental work for this process was carried out by Zhong Ren at Bristol University. The process parameters that were used are given in table B.5.

Table B.5: Passivation parameters using the System100 at low pressure and power.

Machine	ICP
Source power	$1000W$
Forward RF power	$25W$
Process time	$30min$
Process temperature	170^oC
Process pressure	$8mTorr$
Flow rate	$50sccm$

Figure B.14 shows the surface of the unpatterned material after the passivation process. From Figure B.14 it is clear that although the apparent bias voltage problem was addressed there are still large imperfections on the sample. However the nature of the topography in the ICP treated sample is substantially different from those experiments outlined earlier. The sample firstly exhibits a flat surface punctuated with large hemispheres with diameters extending beyond $50\mu m$ in dimension. Compared with earlier results the protrusions are geometrically regular though varying in size, contrasting with the small - sub micron diameter - nodules that entirely covered the previous materials' surface. Figure B.14 shows the effect of the process on bare InP material, i.e. InP with no protective epilayer or cap structures. The inference drawn here is that although physical etching may not be occurring, hence the flat underlying surface of the processed sample, phosphorus

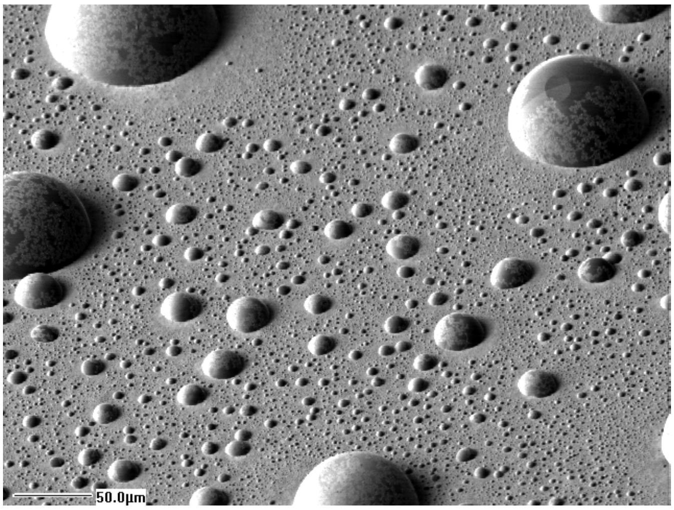

Figure B.14: SEM image of the surface of InP sample after H passivation in the ICP.

is still being liberated by the hydrogen at a slower rate. To pursue the dynamics of the process further a second experiment was carried out on a sample that included the InGaAs cap layer, previously supposed to protect the InP from the phosphorus liberation. The sample used had two sections, an uncapped InP area and an area covered by the InGaAs cap. Figure B.15 shows the sample after the process, where the area at the top of the image is the capped region. Although the cap layer has

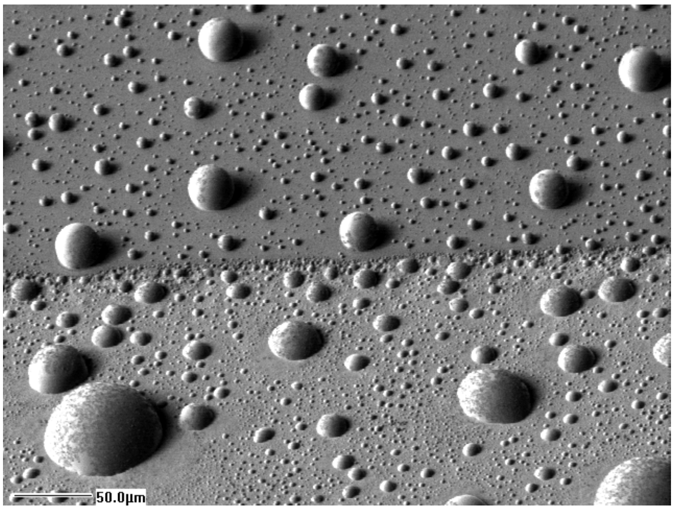

Figure B.15: SEM of InGaAs capped (top half of image) and uncapped (lower half) InP after H passivation in the ICP.

not prevented the formation of the protrusions, it has altered their manifestation.

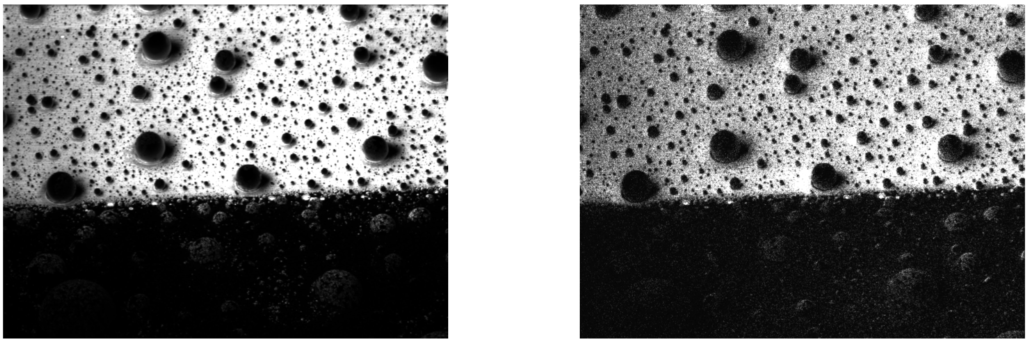

(a) Al (b) As_{75}

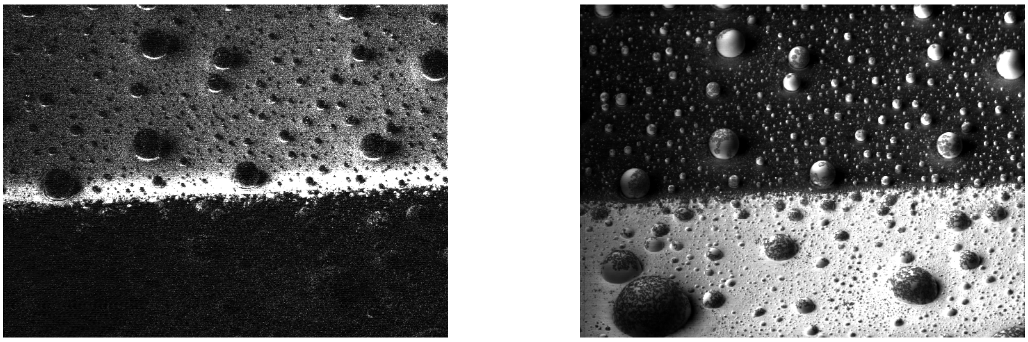

(c) Ga_{71} (d) In_{115}

Figure B.16: SIMS images of InP sample after H^+ treatment in the ICP machine.

In the capped region the formation of extrusions is less dense than in the bare InP region where small bubbles cover most of the surface. In the capped area the lower limit in scale is larger than in the uncapped region, suggesting some critical factor in formation. The shape of the protrusions is also different. In the uncapped region the bubbles are hemispherical, however in the InGaAs capped area they are more similar to protruding spheres. One possibility for the difference between the two regions is that the cap does in fact impede the liberation of phosphorus from the material, but only in so much as it acts as a fine filter, forcing the gas to travel through the cap material. The resulting indium bubbles may be formed through defects in the cap, restrained and hence form into spherical protrusions.
In order to study these effects further, Secondary Ion Mass Spectroscopy (SIMS) analysis was carried out. Figure B.16 shows the SIMS images for the materials characterised in the sample.

The first conclusion that may be drawn from the results in figures B.16 and B.17 concerns the surface stability of the two areas. The results shown for Al,

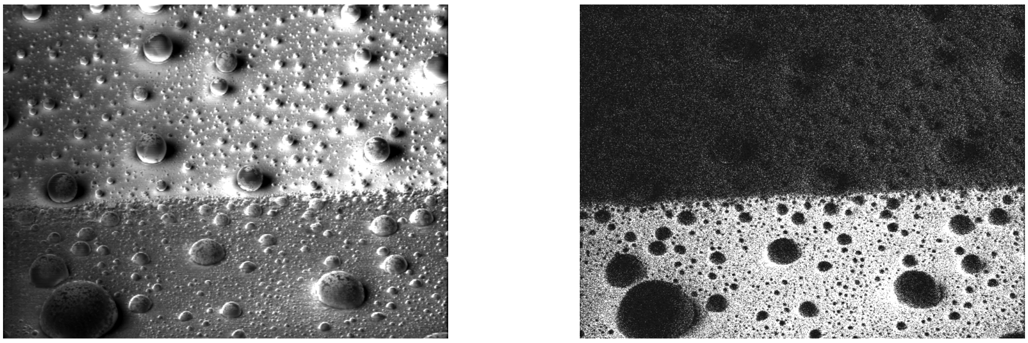

(a) In_{115} post etching

(b) InP

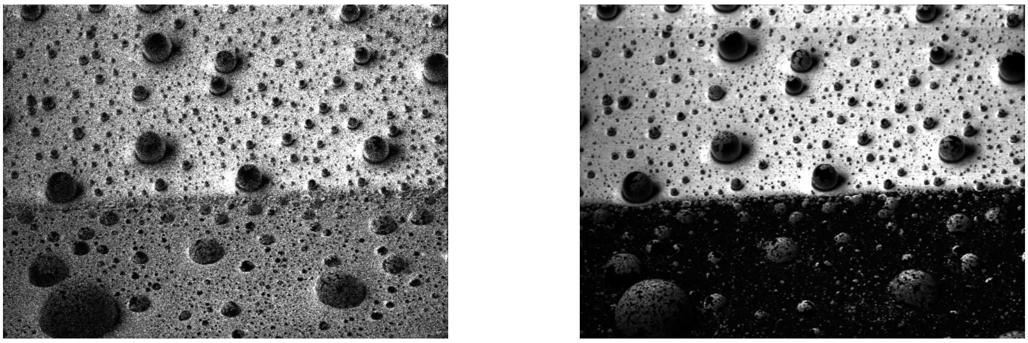

(c) P

(d) Si

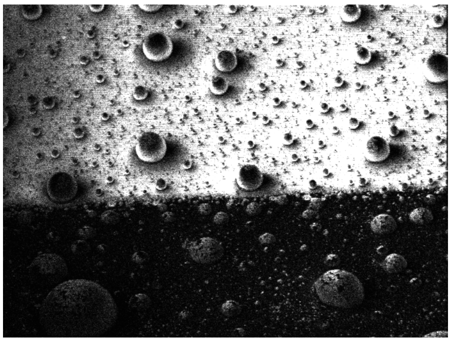

(e) $(SiCHF_3)_{43}$

Figure B.17: SIMS images of InP sample after H^+ treatment in the ICP machine.

As_{75}, and Ga_{71}, all show a high concentration on the cap area, with little presence on the uncapped region and the surfaces of the protrusions. This suggests that the liberation of phosphorus from the uncapped region, being unimpeded, allows the surface to react with the hydrogen directly, whereas the capped region remains unchanged by the reaction. To confirm this conjecture the silicon result may be considered. The silicon is apparent on the capped region, though not the uncapped region. The silicon is sputtered from the sample holder and deposited onto the material, however the unstable bare InP area does not allow it to settle, whereas the capped region must remain stable during the process, as a high silicon concentration is apparent in that area. Further to this the surface of the protrusions may be examined. Figure B.17e shows that silicon is deposited on the hemispheres' surface but is displaced by the structures expansion, confirming that the reaction with hydrogen causes the growth of these structures, rather than the physical etching of them - as previously illustrated in the single process chamber experiments.

The InP is clearly seen on the uncapped layer, but little is found on the InGaAs capped layer, suggesting that the cap material is not etched away, and any reaction with the hydrogen must occur by its diffusion through the cap. Figure B.17c shows phosphorus evenly distributed across the material, showing that it is liberated with the hydrogen gas even through the cap layer. In_{115} is predominantly found in the uncapped area, and significantly, in the protrusions. After etching of the sample the cap layer is removed and the In is found all over the exposed surfaces. It may reasonably be concluded that the protrusions are composed of the In run-off from the hydrogen/phosphorus reaction that forms in hemispheres in the uncapped region and collects through defects in the cap region to form sphere like structures. To confirm this hypothesis the chemical composition of the protrusions was examined in more detail. Figures B.18, B.19 and B.20 show the measured compositions for the large hemispheres on the bare InP surface, the small spheres protruding from the InGaAs cap and the bare surface adjacent to the large hemispheres respectively. From figures B.18, B.19 and B.20 it is clear that the hemispheres and spheres are composed of mainly of indium, with the sputtered silicon coating also observed. The uncapped surface exhibits both indium and phosphorus, suggesting that the run-off indium from the hydrogen/phosphorus reaction is collected in the protrusions and held together with surface tension.

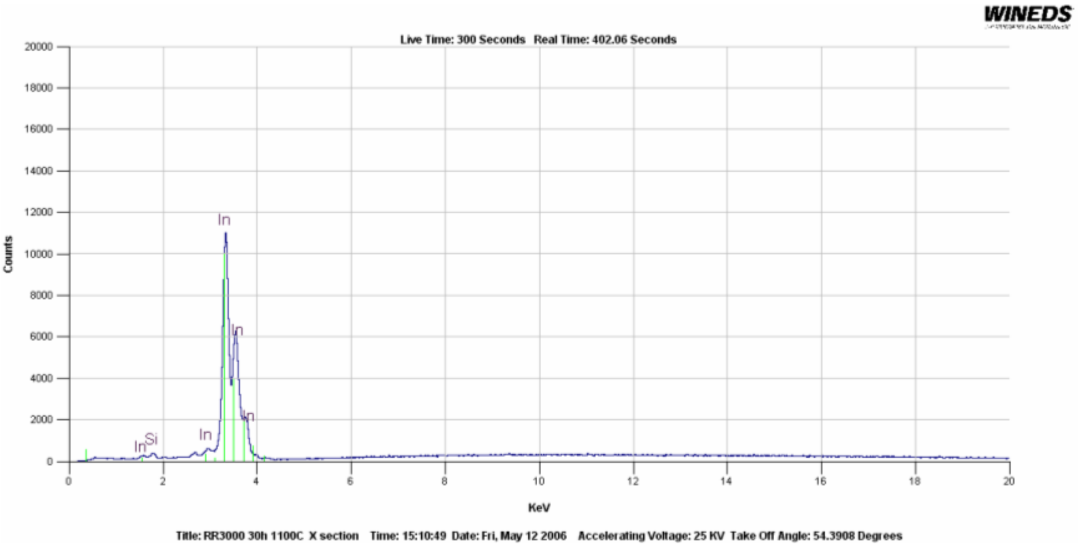

Figure B.18: Composition of large hemisphere structures.

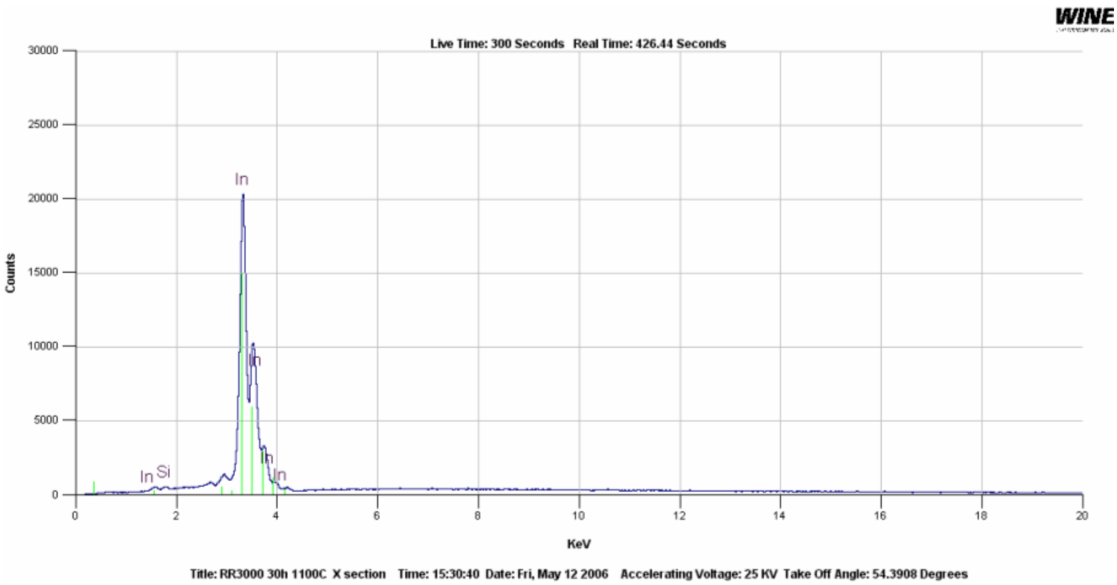

Figure B.19: Composition of small spherical structures.

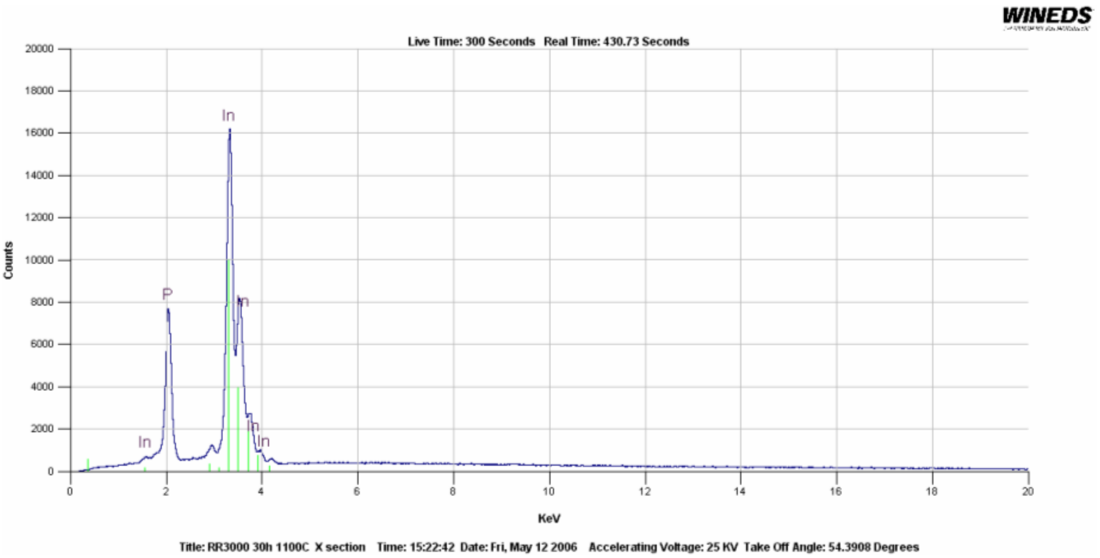

Figure B.20: Composition of area adjacent to large hemisphere structures.

B.3 Conclusions

In this chapter the process of hydrogen passivation of acceptor/donor impurities in III-V lattices for reduction of free-carrier absorption losses was presented. The manner by which the H^+ ions form electrically neutral complexes at dopant sites was shown and the current state of the art assessed. The intention was to diffuse hydrogen ions into the upper cladding of an InP QW epi-structure and measure the effect on waveguide propagation losses. However initial tests using RIE machines to process the samples - over a range of operation parameters - showed poor results, with either the material being physically etched or eroded by liberation of phosphorus to form PH_3 with the hydrogen plasma. To combat these effects PECVD silica masks were implemented but found to effectively prevent the hydrogen diffusion into the material. Finally samples were sent to Bristol university for processesing in their ICP systems, the intention being that the lower process bias may circumvent the problems associated with the RIE processes. However liberation of PH_3 proved to be a limiting factor, even when the sample was covered with an InGaAs cap layer, something suggested in the literature to prevent this effect. SIMS analysis confirmed the formation of Indium bubbles, even through the cap layer, and the physical erosion of an uncapped InP layer. If this work is to be carried further some manner by which the indiffusion of hydrogen into the upper cladding layers of the wafer is allowed, but the out diffusion of phosphorus-hydrogen complexes is suppressed, must be sought, so that the intended dopant passivation is favoured over the erosion of the semiconductor material.

References

[1] E. A. Avrutin, J. H. Marsh, and E. L. Portnoi, “Monolithic and multi-GigaHertz mode-locked semiconductor lasers: Constructions, experiments, models and applications,” *IEE Proceedings-Optoelectronics*, vol. 147, no. 4, pp. 251–278, 2000.

[2] S. Arahira, Y. Matsui, and Y. Ogawa, “Mode-locking at very high repetition rates more than terahertz in passively mode-locked distributed-Bragg-reflector laser diodes,” *IEEE Journal Of Quantum Electronics*, vol. 32, no. 7, pp. 1211–1224, 1996.

[3] B. E. A. Saleh and M. C. Teich, *Fundamentals of photonics.* New York: Wiley, 1991.

[4] S. Bischoff, J. Mork, T. Franck, S. D. Brorson, M. Hofmann, K. Frojdh, L. Prip, and M. P. Sorensen, “Monolithic colliding pulse mode-locked semiconductor lasers,” *Quantum And Semiclassical Optics*, vol. 9, no. 5, pp. 655–674, 1997.

[5] S. D. Brorson, Z. Wang, T. Franck, S. Bischoff, A. Mollerlarsen, J. M. Nielsen, J. Mork, and M. P. Sorensen, “Characterization Of Wavelength Chirping In Modelocked Monolithic CPM Lasers,” *IEEE Photonics Technology Letters*, vol. 7, no. 10, pp. 1148–1150, 1995.

[6] M. B. Flynn, L. O’Faolain, and T. F. Krauss, “Integrated chirp compensation in a monolithic passively mode-locked semiconductor diode laser,” *Applied Physics Letters*, vol. 86, no. 22, 2005.

[7] M. Hofmann, S. Bischoff, T. Franck, L. Prip, S. D. Brorson, J. Mork, and K. Frojdh, “Chirp of monolithic colliding pulse mode-locked diode lasers,” *Applied Physics Letters*, vol. 70, no. 19, pp. 2514–2516, 1997.

[8] R. A. Salvatore, T. Schrans, and A. Yariv, “Pulse Characteristics Of Passively Mode-Locked Diode-Lasers,” *Optics Letters*, vol. 20, no. 7, pp. 737–739, 1995.

[9] S. Sanders, A. Yariv, J. Paslaski, J. E. Ungar, and H. A. Zarem, “Passive-Mode Locking Of A 2-Section Multiple Quantum-Well Laser At Harmonics Of The Cavity Round-Trip Frequency,” *Applied Physics Letters*, vol. 58, no. 7, pp. 681–683, 1991.

[10] M. Schell, M. Tsuchiya, and T. Kamiya, “Chirp and stability of mode-locked semiconductor lasers,” *IEEE Journal Of Quantum Electronics*, vol. 32, no. 7, pp. 1180–1190, 1996.

[11] A. Boskovic, J. R. Taylor, and R. Kashyap, “40 Times Dispersive Broadening Of Femtosecond Pulses And Complete Recompression In A Chirped Fiber Grating,” *Optics Communications*, vol. 119, no. 1-2, pp. 51–55, 1995.

[12] K. C. Byron, K. Sugden, T. Bricheno, and I. Bennion, “Fabrication Of Chirped Bragg Gratings In Photosensitive Fiber,” *Electronics Letters*, vol. 29, no. 18, pp. 1659–1660, 1993.

[13] A. Clarke, P. M. Anandarajah, D. Reid, G. Edvell, L. P. Barry, and J. D. Harvey, “Optimized pulse source for 40-Gb/s systems based on a gain- switched laser diode in conjunction with a nonlinearly chirped grating,” *IEEE Photonics Technology Letters*, vol. 17, no. 1, pp. 196–198, 2005.

[14] B. J. Eggleton, P. A. Krug, L. Poladian, K. A. Ahmed, and H. F. Liu, “Experimental Demonstration Of Compression Of Dispersed Optical Pulses By Reflection From Self-Chirped Optical-Fiber Bragg Gratings,” *Optics Letters*, vol. 19, no. 12, pp. 877–879, 1994.

[15] K. O. Hill, F. Bilodeau, B. Malo, T. Kitagawa, S. Theriault, D. C. Johnson, J. Albert, and K. Takiguchi, “Chirped In-Fiber Bragg Gratings For Compensation Of Optical- Fiber Dispersion,” *Optics Letters*, vol. 19, no. 17, pp. 1314–1316, 1994.

[16] R. Kashyap, S. Chernikov, R. Campbell, P. McKee, J. Williams, and D. Taylor, “Demonstration of dispersion compensation in all-fibre photoinduced chirped gratings,” *Pure Applied Optics*, no. 4, pp. 425–429, 1995.

[17] F. Ouellette, “Dispersion Cancellation Using Linearly Chirped Bragg Grating Filters In Optical Wave-Guides,” *Optics Letters*, vol. 12, no. 10, pp. 847–849, 1987.

[18] ——, “All-Fiber Filter For Efficient Dispersion Compensation,” *Optics Letters*, vol. 16, no. 5, pp. 303–305, 1991.

[19] L. Xia, X. H. Li, X. F. Chen, and S. H. Xie, “A novel dispersion compensating fiber grating with a large chirp parameter and period sampled distribution,” *Optics Communications*, vol. 227, no. 4-6, pp. 311–315, 2003.

[20] M. N. Zervas and D. Taverner, “Asymmetrically apodized linearly chirped fiber Bragg gratings for efficient pulse compression,” *Fiber And Integrated Optics*, vol. 19, no. 4, pp. 355–365, 2000.

[21] Q. Zhang, D. A. Brown, L. J. Reinhart, and T. F. Morse, “Linearly And Nonlinearly Chirped Bragg Gratings Fabricated On Curved Fibers,” *Optics Letters*, vol. 20, no. 10, pp. 1122–1124, 1995.

[22] J. Williams, K. Sugden, I. Zhang, L. andBennion, and N. Doran, “In-fiber grating systems for pulse compression and complete dispersion compensation,” in *IEE Colloquium on Optical Fibre Gratings and Their Applications.* IEE, 1995, pp. 9/1 –9/6.

[23] T. Schrans, R. A. Salvatore, S. Sanders, and A. Yariv, “Subpicosecond (320fs) Pulses From Cw Passively Mode-Locked External Cavity 2-Section Multiquantum Well Lasers,” *Electronics Letters*, vol. 28, no. 16, pp. 1480–1482, 1992.

[24] Y. Silberberg and P. W. Smith, “Subpicosecond Pulses From A Mode-Locked Semiconductor-Laser,” *IEEE Journal Of Quantum Electronics*, vol. 22, no. 6, pp. 759–761, 1986.

[25] N. Stelmakh and J. Lourtioz, “230fs, 25W Pulses from conventional mode-locked laser-diodes with saturable absorber created by ion-implantation,” *Electronics Letters*, vol. 29, no. 2, pp. 160–162, 1993.

[26] J. Lauzon, S. Thibault, J. Martin, and F. Ouellette, “Implementation And Characterization Of Fiber Bragg Gratings Linearly Chirped By A Temperature-Gradient,” *Optics Letters*, vol. 19, no. 23, pp. 2027–2029, 1994.

[27] J. S. Barton, E. J. Skogen, M. L. Masanovic, S. P. Denbaars, and L. A. Coldren, "A widely tunable high-speed transmitter using an integrated SGDBR laser-semiconductor optical amplifier and Mach-Zehnder modulator," *IEEE Journal Of Selected Topics In Quantum Electronics*, vol. 9, no. 5, pp. 1113–1117, 2003.

[28] N. Chen, Y. Nakano, K. Okamoto, K. Tada, G. I. Morthier, and R. G. Baets, "Analysis, fabrication, and characterization of tunable DFB lasers with chirped gratings," *IEEE Journal Of Selected Topics In Quantum Electronics*, vol. 3, no. 2, pp. 541–546, 1997.

[29] H. Hillmer, H. Burkhard, E. Seebald, and K. Kiesel, "Ultrahigh resolution chirped distributed feedback gratings fabricated by electron-beam lithography using bent waveguides for low-cost photonic components," *Journal of Vacuum Science and Technology B*, vol. 13, no. 6, pp. 2853–2858, 1995.

[30] H. Hillmer, A. Grabmaier, S. Hansmann, H. L. Zhu, H. Burkhard, and K. Magari, "Tailored Dfb Laser Properties By Individually Chirped Gratings Using Bent Wave-Guides," *IEEE Journal Of Selected Topics In Quantum Electronics*, vol. 1, no. 2, pp. 356–362, 1995.

[31] H. Hillmer, A. Grabmaier, H. L. Zhu, S. Hansmann, and H. Burkhard, "Continuously Chirped Dfb Gratings By Specially Bent Wave-Guides For Tunable Lasers," *Journal Of Lightwave Technology*, vol. 13, no. 9, pp. 1905–1912, 1995.

[32] B. Mason, G. A. Fish, S. P. DenBaars, and L. A. Coldren, "Widely tunable sampled grating DBR laser with integrated electroabsorption modulator," *IEEE Photonics Technology Letters*, vol. 11, no. 6, pp. 638–640, 1999.

[33] M. Mohrle, A. Sigmund, R. Steingruber, W. Furst, and A. Suna, "All-active tapered 1.55-mu m InGaAsPBH-DFB laser with continuously chirped grating," *IEEE Photonics Technology Letters*, vol. 15, no. 3, pp. 365–367, 2003.

[34] R. Steingruber, M. Mohrle, A. Sigmund, and W. Furst, "Continuously chirped gratings for DFB-lasers fabricated by direct write electron-beam lithography," *Microelectronic Engineering*, vol. 61-2, pp. 331–335, 2002.

[35] G. Steinmeyer, "Dispersion compensation by microstructured optical devices in ultrafast optics," *Applied Physics A-Materials Science & Processing*, vol. 79, no. 7, pp. 1663–1671, 2004.

[36] A. Ward, D. Robbins, G. Busico, E. Barton, L. Ponnampalam, J. Duck, N. Whitbread, P. Williams, D. Reid, A. Carter, and M. Wale, "Widely tunable DS-DBR laser with monolithically integrated SOA: Design and performance," *IEEE Journal of Selected Topics in Quantum Electronics*, vol. 11, no. 1, pp. 149–156, 2005.

[37] P. Anandarajah, C. Guignard, A. Clarke, D. Reid, M. Rensing, L. Barry, G. Edvell, and J. Harvey, "Optimized pulse source employing an externally injected gain-switched laser diode in conjunction with a nonlinearly chirped grating," *IEEE Journal of Selected Topics in Quantum Electronics*, vol. 12, no. 2, pp. 255–264, 2006.

[38] K. Sato, A. Hirano, M. Asobe, and H. Ishii, "Chirp-compensated 40GHz semiconductor modelocked lasers integrated with chirped gratings," *Electronics Letters*, vol. 34, no. 20, pp. 1944–1946, 1998.

[39] K. Sato, A. Hirano, and H. Ishii, "Chirp-compensated 40-GHz mode-locked lasers integrated with electroabsorption modulators and chirped gratings," *IEEE Journal Of Selected Topics In Quantum Electronics*, vol. 5, no. 3, pp. 590–595, 1999.

[40] K. Sato, H. Ishii, Y. Kondo, and M. Yamamoto, "Frequency range extension of actively mode-locked lasers integrated with electroabsorption modulators using chirped gratings," *IEEE Journal Of Selected Topics In Quantum Electronics*, vol. 3, no. 2, pp. 250–255, 1997.

[41] A. M. Schober, G. Imeshev, and M. M. Fejer, "Tunable-chirp pulse compression in quasi-phase-matched second-harmonic generation," *Optics Letters*, vol. 27, no. 13, pp. 1129–1131, 2002.

[42] D. N. Agrawal G.P., *Long-wavelength semiconductor lasers.* Van Nostrand Reinhold, 1986.

[43] B. Malo, S. Theriault, D. C. Johnson, F. Bilodeau, J. Albert, and K. O. Hill, "Apodised In-Fiber Bragg Grating Reflectors Photoimprinted Using A Phase Mask," *Electronics Letters*, vol. 31, no. 3, pp. 223–225, 1995.

[44] P. Cheben, D. X. Xu, S. Janz, and A. Densmore, "Subwavelength waveguide grating for mode conversion and light coupling in integrated optics," *Optics Express*, vol. 14, no. 11, pp. 4695–4702, 2006.

[45] B. M. Holmes and D. C. Hutchings, "Realization of novel low-loss monolithically integrated passive waveguide mode converters," *IEEE Photonics Technology Letters*, vol. 18, no. 1-4, pp. 43–45, 2006.

[46] W. Bogaerts, V. Wiaux, D. Taillaert, S. Beckx, B. Luyssaert, P. Bienstman, and R. Baets, "Fabrication of photonic crystals in silicon-on-insulator using $248 - nm$ deep UV lithography," *IEEE Journal on Selected Topics in Quantum Electronics*, vol. 8, no. 4, p. 928, 2002.

[47] M. Settle, M. Salib, A. Michaeli, and T. F. Krauss, "Low loss silicon on insulator photonic crystal waveguides made by $193\,nm$ optical lithography," *Optics Express*, vol. 14, no. 6, p. 2440, 2006.

[48] Vistec, "Leica VB6 UHR EWF, http://www.vistec-semi.com/," April 2006.

[49] R. A. Gottscho, G. Smolinsky, and R. H. Burton, "Carbon-Tetrachloride Plasma-Etching Of GaAs And InP - A Kinetic-Study Utilizing Nonperturbative Optical Techniques," *Journal Of Applied Physics*, vol. 53, no. 8, pp. 5908–5919, 1982.

[50] T. Katoh, Y. Nagamune, G. P. Li, S. Fukatsu, Y. Shiraki, and R. Ito, "Fabrication Of Ultrafine Gratings On GaAs By Electron-Beam Lithography And 2-Step Wet Chemical Etching," *Applied Physics Letters*, vol. 57, no. 12, pp. 1212–1214, 1990.

[51] S. W. Pang, G. A. Lincoln, R. W. McClelland, P. D. Degraff, M. W. Geis, and W. J. Piacentini, "Effects Of Dry Etching On GaAs," *Journal Of Vacuum Science & Technology B*, vol. 1, no. 4, pp. 1334–1337, 1983.

[52] S. J. Pearton, U. K. Chakrabarti, W. S. Hobson, and A. P. Kinsella, "Reactive Ion Etching Of GaAs, AlGaAs, And GaSb In Cl_2 And $SiCl_4$," *Journal Of Vacuum Science & Technology B*, vol. 8, no. 4, pp. 607–617, 1990.

[53] G. J. Sonek, L. Jianzhong, E. D. Wolf, and J. M. Ballantyne, "$SiCl_4$ Reactive Ion Etching For GaAs Optical Wave-Guides," *Journal Of Lightwave Technology*, vol. 3, no. 5, pp. 1147–1150, 1985.

[54] M. B. Stern and P. F. Liao, "Reactive Ion Etching Of GaAs And InP Using $SiCl_4$," *Journal Of Vacuum Science & Technology B*, vol. 1, no. 4, pp. 1053–1055, 1983.

[55] R. J. Deri and E. Kapon, "Low-Loss III-V Semiconductor Optical Wave-Guides," *IEEE Journal Of Quantum Electronics*, vol. 27, no. 3, pp. 626–640, 1991.

[56] F. P. Payne and J. P. R. Lacey, "A Theoretical-Analysis Of Scattering Loss From Planar Optical Wave-Guides," *Optical And Quantum Electronics*, vol. 26, no. 10, pp. 977–986, 1994.

[57] D. Sparacin, S. Spector, and L. Kimerling, "Silicon waveguide sidewall smoothing by wet chemical oxidation," *Journal of Lightwave Technology*, vol. 23, no. 8, pp. 2455–2461, 2005.

[58] K. Lee, Y. Wang, and M. Houng, "Liquid phase chemical enhanced oxidation on AlGaAs and its application," *Japanese Journal of Applied Physics Part 1-Regular Papers Short Notes & Review Papers*, vol. 43, no. 7A, pp. 4087–4091, 2004.

[59] H. Wang, D. Chou, J. Wu, Y. Wang, and M. Houng, "Effect of crystal orientation and doping on the activation energy for GaAs oxide growth by liquid phase method," *Journal Of Applied Physics*, vol. 87, no. 5, pp. 2629–2633, 2000.

[60] ——, "Surface oxidation kinetics of GaAs oxide growth by liquid phase chemical-enhanced technique," *Japanese Journal of Applied Physics Part 1-Regular Papers Short Notes & Review Papers*, vol. 39, no. 7B, pp. 4477–4480, 2000.

[61] H. Wang, C. Huang, Y. Wang, and M. Houng, "Liquid phase chemical-enhanced oxidation for GaAs operated near room temperature," *Japanese Journal Of Applied Physics Part 2-Letters & Express Letters*, vol. 37, no. 1AB, pp. L67–L70, 1998.

[62] H. Wang, J. Wu, Y. Wang, and M. Houng, “Effects of pH values on the kinetics of liquid-phase chemical-enhanced oxidation of GaAs,” *Journal Of The Electrochemical Society*, vol. 146, no. 6, pp. 2328–2332, 1999.

[63] K. Lee, D. Lim, L. Kimerling, J. Shin, and F. Cerrina, “Fabrication of ultralow-loss Si/SiO_2 waveguides by roughness reduction,” *Optics Letters*, vol. 26, no. 23, pp. 1888–1890, 2001.

[64] E. Kapon and R. Bhat, “Low-Loss Single-Mode GaAs/AlGaas Optical Wave-Guides Grown By Organometallic Vapor-Phase Epitaxy,” *Applied Physics Letters*, vol. 50, no. 23, pp. 1628–1630, 1987.

[65] S. D. McDougall, O. P. Kowalski, C. J. Hamilton, F. Camacho, B. C. Qiu, M. L. Ke, R. M. De La Rue, A. C. Bryce, and J. H. Marsh, “Monolithic integration via a universal damage enhanced quantum-well intermixing technique,” *IEEE Journal Of Selected Topics In Quantum Electronics*, vol. 4, no. 4, pp. 636–646, 1998.

[66] J. Chevallier, A. Jalil, B. Theys, J. C. Pesant, M. Aucouturier, B. Rose, and A. Mircea, “Hydrogen Passivation Of Shallow Acceptors In P-Type InP,” *Semiconductor Science And Technology*, vol. 4, no. 2, pp. 87–90, 1989.

[67] H. P. Gislason, T. Egilsson, K. Leosson, and B. H. Yang, “Lithium Passivation And Electric-Field-Assisted Reactivation Of Acceptors In GaAs,” *Physical Review B*, vol. 51, no. 15, pp. 9677–9681, 1995.

[68] H. P. Gislason, B. H. Yang, and M. Linnarsson, “Shifting Photoluminescence Bands In High-Resistivity Li-Compensated GaAs,” *Physical Review B*, vol. 47, no. 15, pp. 9418–9424, 1993.

[69] A. Henkel, S. L. Delage, M. A. diFortePoisson, H. Blanck, and H. L. Hartnagel, “Boron implantation into GaAs/Ga0.5In0.5P heterostructures,” *Japanese Journal Of Applied Physics Part 1-Regular Papers Short Notes and Review Papers*, vol. 36, no. 1A, pp. 175–180, 1997.

[70] N. M. Johnson, R. D. Burnham, R. A. Street, and R. L. Thornton, “Hydrogen Passivation Of Shallow-Acceptor Impurities In Para-Type GaAs,” *Physical Review B*, vol. 33, no. 2, pp. 1102–1105, 1986.

[71] M. Kumar, J. T. Boyd, H. E. Jackson, J. M. Zavada, H. A. Jenkinson, R. G. Wilson, B. Theys, and J. Chevallier, “Channel optical waveguides formed by deuterium passivation in GaAs and InP,” *Journal Of Applied Physics*, vol. 82, no. 7, pp. 3205–3213, 1997.

[72] J. Marsh, C. Bryce, B. Qui, E. Roa, B. Theys, and Y. Heymes, “Improvements in and relating to optoelectronic devices,” Patent PCT/GB02/04 993, 2003.

[73] K. Otte, G. Lippold, H. Neumann, and A. Schindler, “Hydrogen in CuInSe2,” *Journal Of Physics And Chemistry Of Solids*, vol. 64, no. 9-10, pp. 1641–1647, 2003.

[74] K. Otte, A. Schindler, F. Bigl, and H. Schlemm, “A modified broad beam ion source for low-energy hydrogen implantation,” *Review Of Scientific Instruments*, vol. 69, no. 3, pp. 1499–1504, 1998.

[75] B. Pajot, A. Jalil, J. Chevallier, and R. Azoulay, “Spectroscopic Evidence For The Hydrogen Passivation Of Zinc Acceptors In Gallium-Arsenide,” *Semiconductor Science And Technology*, vol. 2, no. 5, pp. 305–307, 1987.

[76] S. J. Pearton, C. R. Abernathy, R. G. Wilson, F. Ren, and J. M. Zavada, “Effect Of Ion Energy On Hydrogen Diffusion In N- And P- GaAs,” *Electronics Letters*, vol. 31, no. 6, pp. 496–497, 1995.

[77] E. V. K. Rao, M. Allovon, Y. Rafle, M. Juhel, H. Thibierge, B. Theys, and J. Chevallier, “Evaluation of the properties of hydrogenated InP/InGaAsP double heterostructure waveguides,” *Materials Science And Engineering B-Solid State Materials For Advanced Technology*, vol. 44, no. 1-3, pp. 117–120, 1997.

[78] E. V. K. Rao, Y. Gottesman, M. Allovon, E. Vergnol, D. Sigogne, A. Talneau, H. Sik, S. Slempkes, B. Theys, and J. Chevallier, “A significant reduction of propagation losses in InGaAsP-InP buried-stripe waveguides by hydrogenation,” *IEEE Photonics Technology Letters*, vol. 10, no. 3, pp. 370–372, 1998.

[79] B. Theys and F. Jomard, “Diffusion of deuterium (hydrogen) in previously hydrogenated (deuterated) III-V semiconductors,” *Journal Of Applied Physics*, vol. 93, no. 8, pp. 4590–4593, 2003.

[80] B. H. Yang, H. P. Gislason, and M. Linnarsson, “Lithium Passivation Of Zn And Cd Acceptors In P-Type GaAs,” *Physical Review B*, vol. 48, no. 16, pp. 12 345–12 348, 1993.

[81] J. M. Zavada, B. L. Weiss, I. V. Bradley, B. Theys, J. Chevallier, R. Rahbi, R. Addinall, R. C. Newman, and H. A. Jenkinson, “Optical Wave-Guides Formed By Deuterium Passivation Of Acceptors In Si Doped P-Type GaAs Epilayers,” *Journal Of Applied Physics*, vol. 71, no. 9, pp. 4151–4155, 1992.

[82] N. Iwai, T. Mukaihara, N. Yamanaka, M. Itoh, S. Arakawa, H. Shimizu, and A. Kasukawa, “Low threshold, high reliability 1.3 μm PACIS (p-substrate Al-oxide confined inner stripe) lasers and application to laser arrays,” *Electronics Letters*, vol. 35, no. 13, pp. 1081–1082, 1999.

[83] N. Iwai, T. Mukaihara, N. Yamanaka, K. Kumada, H. Shimizu, and A. Kasukawa, “High-performance 1.3 μm InAsP strained-layer quantum-well ACIS (Al-oxide confined inner stripe) lasers,” *IEEE Journal Of Selected Topics In Quantum Electronics*, vol. 5, no. 3, pp. 694–700, 1999.

[84] S. H. Groves, Z. L. Liau, S. C. Palmateer, and J. N. Walpole, “GaInP Mass-Transport And GaInP/GaAs Buried-Heterostructure Lasers,” *Applied Physics Letters*, vol. 56, no. 4, pp. 312–314, 1990.

[85] Z. L. Liau, S. C. Palmateer, S. H. Groves, J. N. Walpole, and L. J. Missaggia, “Low-Threshold Ingaas Strained-Layer Quantum-Well Lasers ($\lambda = 0.98\,\mu m$) With GaInP Cladding Layers And Mass-Transported Buried Heterostructure,” *Applied Physics Letters*, vol. 60, no. 1, pp. 6–8, 1992.

[86] Z. L. Liau and J. N. Walpole, “Mass-Transport - A Promising New Technique For Compound Semiconductor-Device Fabrication,” *Journal Of The Electrochemical Society*, vol. 135, no. 9, pp. C450–C451, 1988.

[87] Z. L. Liau, J. N. Walpole, and D. Z. Tsang, “Fabrication, Characterization, And Analysis Of Mass-Transported Gainasp InP Buried-Heterostructure

Lasers," *IEEE Journal Of Quantum Electronics*, vol. 20, no. 8, pp. 855–865, 1984.

[88] V. N. Bessolov, M. V. Lebedev, Y. M. Shernyakov, and B. V. Tsarenkov, "Sulfur passivation of InGaAs/AlGaAs SQW laser (977 nm) facets in alcohol-based solutions," *Materials Science And Engineering B-Solid State Materials For Advanced Technology*, vol. 44, no. 1-3, pp. 380–382, 1997.

[89] R. Hakimi and M. C. Amann, "Reduction of 1/f carrier noise in InGaAsP/InP heterostructures by sulphur passivation of facets," *Semiconductor Science And Technology*, vol. 12, no. 7, pp. 778–780, 1997.

[90] R. Iyer, R. R. Chang, and D. L. Lile, "Sulfur As A Surface Passivation For InP," *Applied Physics Letters*, vol. 53, no. 2, pp. 134–136, 1988.

[91] R. Iyer and D. L. Lile, "Role Of Polysulfides In The Passivation Of The InP Surface," *Applied Physics Letters*, vol. 59, no. 4, pp. 437–439, 1991.

[92] M. R. Ravi, A. DasGupta, and N. DasGupta, "Effect of sulfur passivation and polyimide capping on InGaAs- InPPIN photodetectors," *IEEE Transactions On Electron Devices*, vol. 50, no. 2, pp. 532–534, 2003.

[93] C. J. Sandroff, M. S. Hegde, L. A. Farrow, C. C. Chang, and J. P. Harbison, "Electronic Passivation Of GaAs-Surfaces Through The Formation Of Arsenic Sulfur Bonds," *Applied Physics Letters*, vol. 54, no. 4, pp. 362–364, 1989.

[94] C. J. Sandroff, R. N. Nottenburg, J. C. Bischoff, and R. Bhat, "Dramatic Enhancement In The Gain Of A GaAs/AlGaAs Heterostructure Bipolar-Transistor By Surface Chemical Passivation," *Applied Physics Letters*, vol. 51, no. 1, pp. 33–35, 1987.

[95] Y. K. Su, H. C. Wang, C. L. Lin, W. B. Chen, and S. M. Chen, "Improvement of AlGaInP light emitting diode by sulfide passivation," *IEEE Photonics Technology Letters*, vol. 15, no. 10, pp. 1345–1347, 2003.

[96] D. B. Young, A. Kapila, J. W. Scott, V. Malhotra, and L. A. Coldren, "Reduced Threshold Vertical-Cavity Surface-Emitting Lasers," *Electronics Letters*, vol. 30, no. 3, pp. 233–235, 1994.

[97] T. S. Shamirzaev, K. S. Zhuravlev, A. Y. Kobitski, H. P. Wagner, and D. R. T. Zahn, "Passivation of growth defects in GaAs/AlGaAs multiple quantum well structures by CF_4 plasma," *Physica B*, vol. 308, pp. 761–764, 2001.

[98] S. R. Andrew, J. H. Marsh, M. C. Holland, and A. H. Kean, "Quantum-Well Laser With Integrated Passive Wave-Guide Fabricated By Neutral Impurity Disordering," *IEEE Photonics Technology Letters*, vol. 4, no. 5, pp. 426–428, 1992.

[99] K. Hamamoto, S. Sugou, K. Komatsu, and M. Kitamura, "Extremely Low-Loss 4 X 4 GaAs/AlGaAs Optical Matrix Switch," *Electronics Letters*, vol. 29, no. 17, pp. 1580–1582, 1993.

[100] M. Gnan, "Photonic Wire Devices in Silicon-on-Insulator," Ph.D. dissertation, University of Glasgow, 2007.

[101] L. B. Soldano, F. B. Veerman, M. K. Smit, B. H. Verbeek, A. H. Dubost, and E. C. M. Pennings, "Planar Monomode Optical Couplers Based On Multimode Interference Effects," *Journal Of Lightwave Technology*, vol. 10, no. 12, pp. 1843–1850, 1992.

[102] Y. Shani, C. H. Henry, R. C. Kistler, K. J. Orlowsky, and D. A. Ackerman, "Efficient Coupling Of A Semiconductor-Laser To An Optical Fiber By Means Of A Tapered Wave-Guide On Silicon," *Applied Physics Letters*, vol. 55, no. 23, pp. 2389–2391, 1989.

[103] S. Akiyama, M. A. Popovic, P. T. Rakich, K. Wada, E. Michel, H. A. Haus, E. P. Ippen, and L. C. Kimerling, "Air trench bends and splitters for dense optical integration in low index contrast," *Journal Of Lightwave Technology*, vol. 23, no. 7, pp. 2271–2277, 2005.

[104] D. X. Dai, J. J. He, and S. L. He, "Elimination of multimode effects in a silicon-on-insulator etched diffraction grating demultiplexer with bi-level taper structure," *IEEE Journal Of Selected Topics In Quantum Electronics*, vol. 11, no. 2, pp. 439–443, 2005.

[105] D. X. Dai, S. L. He, and H. K. Tsang, "Bilevel mode converter between a silicon nanowire waveguide and a larger waveguide," *Journal Of Lightwave Technology*, vol. 24, no. 6, pp. 2428–2433, 2006.

[106] I. Moerman, P. P. Van Daele, and P. M. Demeester, "A review on fabrication technologies for the monolithic integration of tapers with III-V semiconductor devices," *IEEE Journal Of Selected Topics In Quantum Electronics*, vol. 3, no. 6, pp. 1308–1320, 1997.

[107] K. Solehmainen, T. Aalto, J. Dekker, M. Kapulainen, M. Harjanne, and P. Heimala, "Development of multi-step processing in silicon-on-insulator for optical waveguide applications," *Journal Of Optics A-Pure And Applied Optics*, vol. 8, no. 7, pp. S455–S460, 2006.

[108] N. Yamaguchi, Y. Kokubun, and K. Sato, "Low-Loss Spot-Size Transformer By Dual Tapered Wave-Guides (Dtw-Sst)," *Journal Of Lightwave Technology*, vol. 8, no. 4, pp. 587–594, 1990.

[109] H. Yanagawa, T. Shimizu, S. Nakamura, and I. Ohyama, "Index-And-Dimensional Taper And Its Application To Photonic Devices," *Journal Of Lightwave Technology*, vol. 10, no. 5, pp. 587–592, 1992.

[110] E. A. J. Marcatili, "Dielectric Tapers With Curved Axes And No Loss," *IEEE Journal Of Quantum Electronics*, vol. 21, no. 4, pp. 307–314, 1985.

[111] J. D. Love, W. M. Henry, W. J. Stewart, R. J. Black, S. Lacroix, and F. Gonthier, "Tapered Single-Mode Fibers And Devices. 1. Adiabaticity Criteria," *IEE Proceedings-J Optoelectronics*, vol. 138, no. 5, pp. 343–354, 1991.

[112] O. Mitomi, K. Kasaya, and H. Miyazawa, "Design Of A Single-Mode Tapered Wave-Guide For Low-Loss Chip-To-Fiber Coupling," *IEEE Journal Of Quantum Electronics*, vol. 30, no. 8, pp. 1787–1793, 1994.

[113] C. T. Lee, M. L. Wu, L. G. Sheu, P. L. Fan, and J. M. Hsu, "Design and analysis of completely adiabatic tapered waveguides by conformal mapping," *Journal Of Lightwave Technology*, vol. 15, no. 2, pp. 403–410, 1997.

[114] C. Vassallo, "Analysis Of Tapered Mode Transformers For Semiconductor Optical Amplifiers," *Optical And Quantum Electronics*, vol. 26, no. 3, pp. S235–S248, 1994.

[115] A. Taflove, *Computational electrodynamics : the finite-difference time-domain method.* Boston: Artech House, 1995.

[116] J. Azana and L. R. Chen, "Synthesis of temporal optical waveforms by fiber Bragg gratings: a new approach based on space-to-frequency-to-time mapping," *Journal Of The Optical Society Of America B-Optical Physics*, vol. 19, no. 11, pp. 2758–2769, 2002.

[117] E. V. K. Rao, M. Allovon, Y. Rafle, M. Juhel, H. Thibierge, B. Theys, and J. Chevallier, "Evaluation of the properties of hydrogenated InP/InGaAsP double heterostructure waveguides," *Materials Science And Engineering B-Solid State Materials For Advanced Technology*, vol. 44, no. 1-3, pp. 117–120, 1997.

[118] E. V. K. Rao, Y. Gottesman, M. Allovon, E. Vergnol, D. Sigogne, A. Talneau, H. Sik, S. Slempkes, B. Theys, and J. Chevallier, "A significant reduction of propagation losses in InGaAsP-InP buried-stripe waveguides by hydrogenation," *IEEE Photonics Technology Letters*, vol. 10, no. 3, pp. 370–372, 1998.